

# Electron dynamics in optically excited systems: Molecules, solids and interfaces



Dissertation zur Erlangung des akademischen Grades  
*doctor rerum naturalis (Dr. rer. nat.)*

Marvin Krenz

Department Physik, Arbeitsgruppe Theoretische Materialphysik  
Universität Paderborn

Name: Marvin Krenz  
Geboren am: 12.12.1994  
Geburtsort: Paderborn  
Eingereicht am: 10.10.2023

### **Promotionskommission**

Vorsitzender: Prof. Dr. Donat As  
Optoelectronic semiconductors – Group III nitrides  
Department Physik – Universität Paderborn

Erstgutachter: Prof. Dr. Wolf Gero Schmidt  
Theoretical Material Physics  
Department Physik – Universität Paderborn

Zweitgutachter: Prof. Dr. Simone Sanna  
Solid State Spectroscopy  
Institut für Theoretische Physik – Justus-Liebig-Universität Gießen

Vertreter des Mittelbaus: Dr. Julien Pinske  
Theoretical Quantum Systems  
Department Physik – Universität Paderborn

## Abstract

The density functional theory (DFT) is a well established tool in both chemistry and solid state physics for the calculation of structural, electronic and optical properties for a wide variety of materials. By expanding on the DFT, for example by adding constraints to the density or occupation (cDFT), one is able to also describe excited system properties, which also sees ever growing applications. However, an often less explored area are time dependent system properties like decay or transition times, as the calculation of dynamic properties is generally more complicated and/or more computationally expensive as for static ones. The increase of computational power in the last decades, however, makes it possible to have a look at these properties for an ever growing number of systems. A possibility to simulate dynamic properties are DFT based molecular dynamics (MDs), and by extension the non-adiabatic molecular dynamics (NAMDs).

In this thesis both MDs and NAMDs as well as further supplementary methods are used to determine specific dynamic properties in three different optically excited systems at different temperatures. For the oxirane molecule the photochemical decomposition is studied with the focus on the excited state life times, their influence on the reactions as well as the reaction yields. Reaction yields and lifetime are in good agreement with both theory and experiment. The excited states responsible for the reaction show slight differences to previous works.

The lithium niobate crystal is examined in respect to the bound polaron formation time and its formation mechanism. The formation time, calculated to be between 50 and 75 fs, is on the lower end of experimental values. The formation time was found to be strongly dependent on the phase of the oxygen breathing phonon modes.

In case of the Si(111)-tetracene interface the triplet exciton transfer from the tetracene layer to the silicon is studied. The introduction of a point defect to the passivating H layer proved to be vital for the transfer by enabling a level crossing of the Si dangling bond state via a  $sp^3 \rightarrow sp^2 + p$  rehybridization. The transfer time was calculated to take several 100 fs up to the picosecond range.



## Kurzfassung

Die Dichtefunktionaltheorie (DFT) ist eine fest etablierte Methode in Chemie und Festkörperphysik zur Berechnung von strukturellen, elektronischen und optischen Eigenschaften einer Vielzahl von Materialien. Auf der DFT aufbauende Methoden, wie beispielsweise die constraint DFT (cDFT), in welcher die Dichte oder die Besetzungszahlen zusätzlichen Einschränkungen unterworfen werden, ermöglichen es zudem die Eigenschaften von angeregten Systemen zu betrachten; diese Methoden erfreuen sich immer zunehmender Beliebtheit. Ein jedoch selteneres Anwendungsgebiet ist die Simulation von zeitabhängigen Eigenschaften wie Zerfalls- oder Transferzeiten, da die Berechnung von solchen dynamischen Eigenschaften kompliziert und/oder aufwendig ist. Der Zuwachs an Rechenleistung in den letzten Jahrzehnten macht es jedoch möglich solche Eigenschaften in immer mehr Systemen zu berechnen. Eine Möglichkeit diese dynamischen Eigenschaften zu simulieren sind DFT basierte Molekulardynamiken (MDs), und in Erweiterung die nicht-adiabatischen Molekulardynamiken (NAMDs).

In dieser Arbeit werden sowohl MDs als auch NAMDs zusammen mit weiteren unterstützenden Methoden verwendet, um bestimmte Eigenschaften von drei unterschiedlichen optisch angeregten Systemen bei verschiedenen Temperaturen zu bestimmen. Im ersten System, dem Oxiran Molekül, wird die photochemische Zersetzung in Bezug auf die Lebensdauer der angeregten Zustände, ihr Einfluss auf die Reaktion, sowie auf die Reaktionsprodukte untersucht. Die Verhältnisse der Reaktionsprodukte sowie die Lebensdauer der Zustände entsprechen sowohl experimentellen als auch theoretischen Befunden. Die elektronischen Zustände welche für die Reaktion verantwortlich sind unterscheiden sich allerdings leicht zu denen aus vorherigen Arbeiten.

Als zweites System wurde der Lithiumniobat Kristall untersucht bezüglich des Polaronenbildungsmechanismus und der Polaronenbildungszeit. Die berechnete Bildungszeit liegt zwischen 50 und 75 fs, was am unteren Ende der experimentell gemessenen Zeiten liegt. Die Bildungszeit ist zudem stark von der Phase der „Atmungsmoden“ des Sauerstoffs abhängig.

Als letztes System wird das Si(111)-Tetrazen betrachtet. Hier wird der Transfer eines Triplet-Exzitons von der Tetrazenschicht zum Silizium untersucht. Es stellt sich heraus, dass das Einbringen eines Defekts in die passivierende H Schicht notwendig ist um den Transfer zu ermöglichen, wobei dieser durch ein „levelcrossing“ des „dangling bond“ Si Zustands zustande kommt, welcher wiederum durch eine Rehybridisierung von  $sp^3$  nach  $sp^2+p$  verursacht wird. Die Transferzeit des Exzitons beträgt mehrere hundert Femtosekunden bis in den Pikosekundenbereich.

# Contents

<b>Abbreviations</b>	<b>VIII</b>
<b>1. Introduction</b>	<b>1</b>
<b>2. Theoretical foundations</b>	<b>5</b>
2.1. Periodic boundary conditions, Born-Oppenheimer approximation . . . . .	5
2.2. Density functional theory . . . . .	6
2.3. Molecular dynamics using density functional theory . . . . .	8
2.4. Simulation of the temperature . . . . .	9
2.5. Phonons . . . . .	12
2.6. Excited states within density functional theory . . . . .	13
2.7. Interband transitions . . . . .	15
2.8. Localized states in density functional theory . . . . .	18
2.8.1. Problems of the density functional theory . . . . .	18
2.8.2. DFT+U . . . . .	18
2.8.3. Hybrid functionals . . . . .	21
<b>3. First reference system: Oxirane</b>	<b>25</b>
3.1. Introductions . . . . .	25
3.2. Modelling the static molecule . . . . .	26
3.3. The dynamic system: Methods and parameters . . . . .	28
3.4. Results: Statistics of the <i>NVE</i> and <i>NVT</i> ensemble . . . . .	30
3.5. Results: States during the Reaction . . . . .	33
<b>4. Polaron formation in lithium niobate</b>	<b>37</b>
4.1. Introduction: Lithium niobate and polarons . . . . .	37
4.2. Polarons in lithium niobate: Types and classifications . . . . .	38
4.3. Detection of polarons . . . . .	39
4.4. Modelling the free polaron . . . . .	39
4.5. Modelling the bound polaron . . . . .	42
4.6. Molecular dynamics: Parameters and starting configurations . . . . .	43
4.6.1. The influence of the starting configuration . . . . .	43
4.7. Analysing the trajectories: Thresholds and additional methods . . . . .	44
4.8. Results . . . . .	48
4.8.1. Localization and formation times . . . . .	48
4.8.2. The influence of the Hubbard U . . . . .	50
4.8.3. Lattice relaxation . . . . .	51
4.9. Non-adiabatic potential energy surface hopping in lithium niobate . . . . .	52
<b>5. Exciton dynamics at the silicon-tetracene interface</b>	<b>57</b>
5.1. Silicon, tetracene and solar cells . . . . .	57
5.2. The ideal Si(111)-TC interface . . . . .	59
5.2.1. Modelling . . . . .	59
5.2.2. Excursion: Which (hybrid) functional to choose? . . . . .	60
5.2.3. Band alignment . . . . .	63
5.3. Introducing the defect . . . . .	65
5.4. Dynamics . . . . .	69
5.4.1. Surface hopping at interfaces and with level crossings . . . . .	71

5.4.2. Transfer times . . . . .	74
Starting configurations . . . . .	76
Trajectories and results . . . . .	77
5.4.3. Exciton transfer using DFT+U . . . . .	81
<b>6. Conclusions</b>	<b>85</b>
<b>A. Program modifications</b>	<b>89</b>
<b>B. Publications</b>	<b>89</b>
<b>Bibliography</b>	<b>90</b>
<b>List of Figures</b>	<b>100</b>
<b>List of Tables</b>	<b>101</b>

## Abbreviations

<b>Computational approaches</b>	
(c-)DFT	(constrained) density functional theory
DFT+U	density functional theory with Hubbard correction
FSSH	fewest switches surface hopping
KS	Kohn-Sham
MD	molecular dynamic
NEB	nudged elastic band
NBRA	neglect of back-reaction approximation
<i>NVE</i>	thermodynamic ensemble with constant particle count, volume and energy
<i>NVT</i>	thermodynamic ensemble with constant particle count, volume and temperature
SIE	self interaction error
TD-DFT	time dependent density functional theory
<b>Exchange-correlation functionals</b>	
B3LYP	three parameter Becke-Lee-Yang-Parr hybrid functional
GGA	generalized gradient approximation
HSE(-X)	Heyd-Scuseria-Ernzerhof hybrid functional (with X percent exact exchange)
LDA	local density approximation
PBE	Perdew-Burke-Ernzerhof functional
PBEsol	Perdew-Burke-Ernzerhof functional optimized for solids
PBE0	Perdew-Burke-Ernzerhof hybrid functional
<b>Model related abbreviations</b>	
db	dangling bond
HD	high density
LD	low density
LN	lithium niobate
Si-TC <sub>Si*</sub>	silicon-tetracene interface with triplet excitation at the silicon surface
Si-TC <sub>TC*</sub>	silicon-tetracene interface with triplet excitation at the tetracene surface
TC	tetracene
<b>Other</b>	
HOMO	highest occupied molecular orbital
LUMO	lowest unoccupied molecular orbital
PDOS	partial density of states
PES	potential energy surface

---

## 1. Introduction

Systems with excited electronic states are one of the cornerstones of modern technology. From the information technology based on semiconductors over lasers to such apparently mundane things as UV curable adhesive, all employ thermally or optically excited electronic states. For many basic properties like the frequency of a laser a view on the properties of the system in its geometric ground (and sometimes excited) state is often sufficient – therefore most theoretical investigations are static. If, however, a structural change causes a substantial change in electronic structure, or one is interested in a time dependent parameter like excitation decay or phase transition times, a look at the whole dynamic of the system becomes necessary.

Such changes in electronic structure can be caused by different things. A structural change like a phase transition, a chemical reaction or just lattice vibrations can cause the electrons to change their energy, impulse and position. The thermal or optical excitation process usually has an influence on the forces acting in the system, which in return can cause structural change, which then may cause electronic structure changes. Through these changes the electron may then relax to a lower energetic state, which again can cause structural changes. Last but not least an external influence like a time dependent electric field can cause a change in electronic structure.

Having such a vast amount of interacting parts in a dynamic system leads to an abundance of different phenomena which can occur in such a system. Depending on the phenomenon and the size of the considered system, different methods of description of the excitation and/or the dynamic can or rather have to be utilized. To simulate such dynamics the density functional based molecular dynamics are a typical choice. Those are commonly used for small systems and/or electronic ground states. In this work several phenomena occurring during electron dynamics will be explored in different systems by using density functional based *ab initio* molecular dynamics as main method for the description of the systems. However, in contrast to the commonly used approaches, calculations spanning several excited states with non-adiabatic switching between those states will be covered, allowing the study of not only the movement of ions in excited electron configurations, but also the electronic relaxation. First, the optical dissociation of the oxirane molecule will be examined as a reference system, in which the influence of different excited states onto the geometric structure of the molecule, as well as the electronic relaxation process can be observed. As the second system the lithium niobate crystal, an optical non-linear material with numerous optical applications will be examined. In detail the mechanics of the polaron – a quasiparticle which influences the non-linear properties – formation, its formation time and dynamics are studied, shedding light onto the influence of the lattice vibrations on electron localization. With the insights gained by these two systems, at last the exciton transfer between the silicon-111 surface and a tetracene layer is examined using and comparing different descriptions, which not only applies the methods to a medium sized system, but also covers a subject of high technological relevance, the hybrid solar cell.

This work is structured as follows: First the basics of the methods used in most or all of the systems are explained in chapter 2. Afterwards, the different systems are examined one by one. For each system, the system itself, the phenomenon to be observed and important quantities are introduced. Following this the system in its electronic and geometric ground state is modelled, and the gained information discussed. Then we switch to the time resolved description of the dynamic system, where first the computational parameters and the methods to analyse the phenomena in the time domain dynamic system are explained.

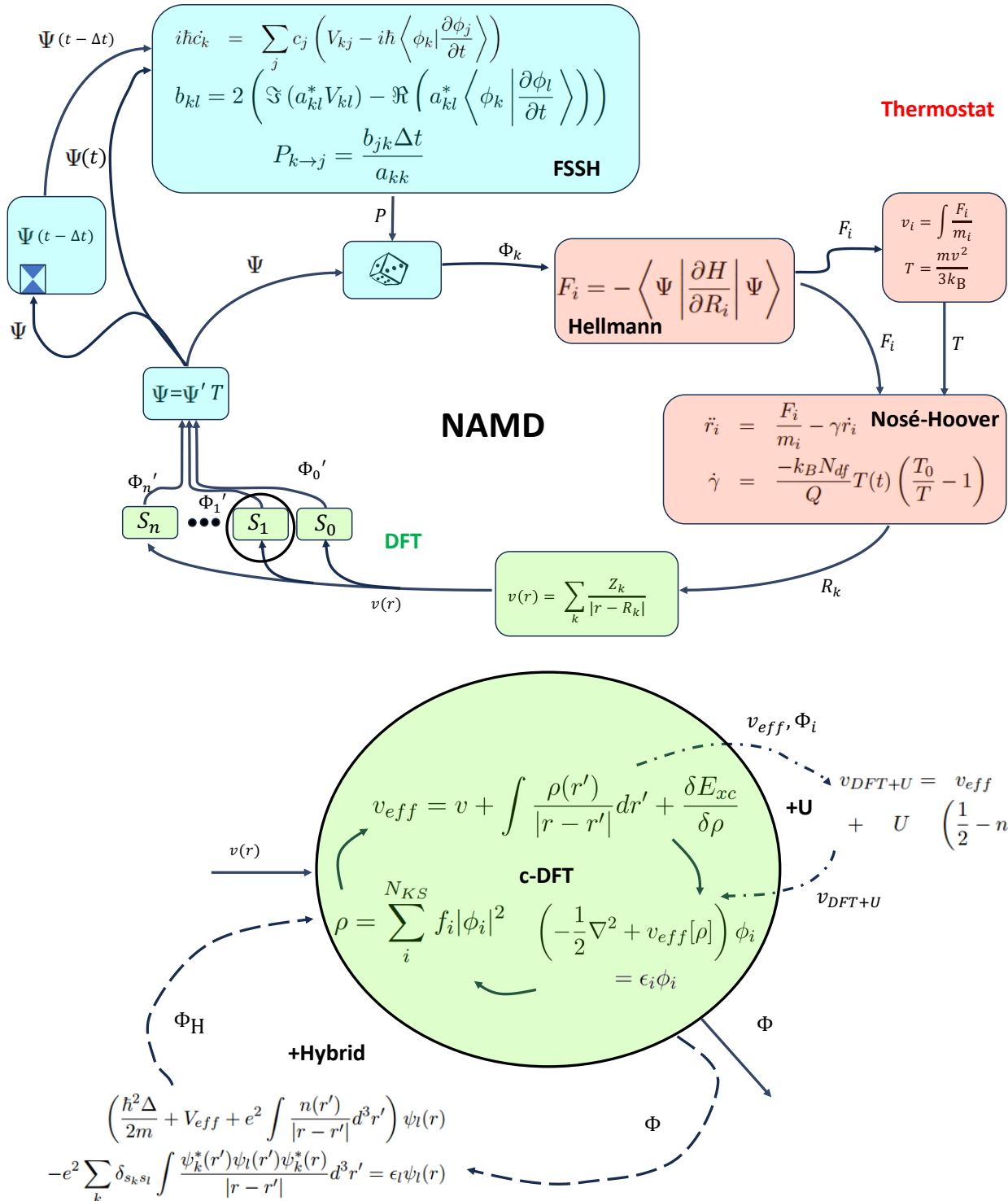
## 1 INTRODUCTION

---

With all methods and parameters discussed, the results are shown and analysed, ending with a summary of each system. After all systems are handled this way, each system is summarized and the used methods are evaluated.



## Surface Hopping



Theoretical foundations

---

## 2. Theoretical foundations

### 2.1. Periodic boundary conditions, Born-Oppenheimer approximation

Before going into detail for the specific methods a few approximations and simplifications have to be made in order to make the many-particle problem of a solid solvable. A typical solid consists of approximately  $10^{23}$  particles<sup>[1]</sup>. A full quantum mechanical description would encompass solving the Schrödinger equation for a Hamiltonian of similar size, i.e. diagonalizing a matrix of rank  $N^{3 \cdot 10^{23}}$  (with  $N$  being the discretization), which is obviously not possible. To solve this problem a reduction of the size is in order. Solid states are differentiated into two groups; on one hand, the amorphous solids, and on the other one, the crystalline solids. Amorphous materials do not have an ordered atomic structure and are therefore difficult to describe. Crystalline solids, however, consist (at least at a temperature of 0 K) of periodically repeating ground structures called unit cells. These unit cells usually contain between 1 and 1000 atoms. A first step in describing such a crystalline solid is to reduce the problem to this unit cell. In order to do so, the Bloch theorem is employed:<sup>[1,2]</sup>

$$\Psi(r) = e^{ik \cdot r} u_i(r) \quad (2.1)$$

Where  $k$  is a wave vector and  $u_i$  is a lattice periodic function. Instead of calculating the wave functions for the whole crystal (with  $r \rightarrow \infty$ ),  $r$  is confined to the unit cell and the variable  $k$  is introduced, where  $k$  is chosen from the set given by the condition  $k \cdot r \in [0, 2\pi]$ . This set of allowed  $k$  vectors is referred to as first Brillouine zone.<sup>[1]</sup> Within computational numeric an infinitely dense set of  $k$  vectors cannot be used for obvious reasons, it has to be discretized. In this context the discretized  $k$  vectors are also referred to as  $k$ -points. The lattice periodic function has also to be discretized, where a common representation is to expand the function in the plane wave basis. For an exact description of the function an infinite amount of plane waves would have to be considered, which is again impossible. Instead a sub set of plane waves is used, where the plane waves are chosen by their wave number (i.e. their contribution to the kinetic energy of the electron), beginning with the lowest ones.<sup>[3]</sup> The set is limited by an energy corresponding to the highest included wave number, the so-called (kinetic-) cutoff energy. All later introduced methods for solving the many particle problem employ both  $k$ -points and cutoff energy as essential parameters for the accuracy of the calculations.

Until now the many particle problem was only reformulated and therefore exact. Now the Hamiltonian  $H(\{r_i\}, \{R_i\})$  is simplified by an approximation. After rescaling the operator to get rid of the units, the Hamiltonian has the form<sup>[1,4]</sup>:

$$\frac{H}{E_0} = -\frac{1}{2} \sum_i \frac{\partial^2}{\partial r_i^2} - \frac{1}{2} \sum_k \frac{m_e}{M_k} \frac{\partial^2}{\partial R_k^2} + \sum_{i < j} \frac{1}{|r_i - r_j|} + \sum_{k < l} \frac{Z_k Z_l}{|R_k - R_l|} - \sum_{i, k} \frac{Z_k}{|r_i - R_k|} \quad (2.2)$$

It is apparent that the second term, which describes the movement of the ions, is dependent on the ratio between electron mass  $m_e$  and nuclei mass  $M_k$ . This ratio is of the order of  $10^{-5}$  and can be therefore discarded in most cases. As a consequence the energy is not explicitly dependent on the nuclei positions  $R_k$ , they can be seen as fixed external parameters. Therefore, two separate differential equations are obtained, one of the electrons in the

potential of the fixed nuclei and one for the ion movement. This approximation is known as Born-Oppenheimer approximation<sup>[1]</sup> and is used in all following methods. For the sake of clarification it should be noted that very often the Born-Oppenheimer approximation is associated with an adiabatic development of the system, i.e. the system stays in its quantum state, therefore the ions are moving on one potential energy surface.<sup>[5]</sup> This is, however, not necessarily the case, as will be shown in chapter 2.7. A switching between states can be achieved while still treating the ion movement and electron dynamics only parametrical dependent on each other. Thus a non-adiabatic development of a system can be simulated while still obeying the Born-Oppenheimer approximation.

## 2.2. Density functional theory

After applying the Born-Oppenheimer approximation, the electronic system for a fixed ionic potential has to be solved. As mentioned in the last chapter, solving the Schrödinger equation requires the construction and diagonalization of the Hamiltonian, which in turn requires a discretization of the Hamiltonian and wave function. If for a system with  $N_e$  electrons a basis set consisting of  $N$  basis states is chosen, the Hamiltonian has the dimension of  $N^{3N_e}$ . With an interacting system even a small number of electrons would lead to calculation times spanning years. To bypass this problem the density functional theory (DFT), a wide spread procedure to describe solids quantum mechanically, was developed. The basis for the DFT are the Hohenberg-Kohn theorems. The first Hohenberg-Kohn theorem states that the electric potential of the ground state is explicitly assigned to the electronic density  $\rho$  of the ground state. Following this, the ground state Hamiltonian is also assigned to the ground state electronic density. The second Hohenberg-Kohn theorem states that deviating from the electronic ground state density can only lead to higher energetic configurations.<sup>[6]</sup> Combining those theorems, the ground state density can be obtained by minimizing the functional of the energy depending on the electronic density  $E[\rho]$  under the condition that the density corresponds to the number of electrons in the system (i.e.  $\int \rho(r)dr = N_e$ ). This functional is, however, not known, the density has to be calculated on a detour. First the electron-ion interaction is separated from the functional, since its dependence is known explicitly:<sup>[7]</sup>

$$E_{e-n} = \langle \Psi | V_{e-n} | \Psi \rangle = \int v(r)\rho(r)dr = E_{e-n}[\rho] \quad (2.3)$$

With  $v$  being the potential of the ions. The energy functional is now given with

$$E[\rho] = F[\rho] + \int v\rho dr \quad (2.4)$$

Where  $F$  is the functional for the kinetic energy of the electrons and the electron-electron interaction, which is, however, also unknown. To minimize this functional, a functional derivative with respect to  $\rho$  is conducted with the constraint of the integral of the density being equal to the number of electrons. By setting the resulting equation to zero, one gains the Euler-Lagrange equation for the electron density:

$$\mu = v + \frac{\delta F}{\delta \rho} \quad (2.5)$$

In order to actually calculate  $\rho$  usually the Kohn-Sham ansatz is employed. In the Kohn-Sham ansatz the interacting system is replaced by a non-interacting one, which has to have the same electronic density as the interacting system.<sup>[8]</sup> The corresponding functional  $F_{KS}$  only consists of the kinetic energy of the electrons. To achieve the same density the external potential (which is the electron-ion interaction in the interactive system) of the non-interacting system has to be modified. This potential is also referred to as effective potential  $v_{\text{eff}}$ . Setting the Lagrange multipliers<sup>[9]</sup> of the systems equal, one gains for the effective potential:

$$v_{\text{eff}} = v + \frac{\delta F}{\delta \rho} - \frac{\delta F_{KS}}{\delta \rho} \quad (2.6)$$

The functional  $F$  is then also separated into an interacting and non-interacting part,  $F = F_{KS} + F_{WW}$ . The effective potential is therefore given by

$$v_{\text{eff}}[\rho] = v + \frac{\delta F_{WW}[\rho]}{\delta \rho} \quad (2.7)$$

With the effective potential the energy and one-particle wave functions can be obtained. Since the substitute system is a non-interacting one, it can be solved by the one-particle Schrödinger equation<sup>[8]</sup>:

$$\left( -\frac{1}{2} \nabla^2 + v_{\text{eff}}[\rho] \right) \phi_i = \epsilon_i \phi_i \quad (2.8)$$

Neglecting the possible interaction between electron states, the resulting electron density can be written as:<sup>1</sup>

$$\rho = \sum_i^{N_e} |\phi_i|^2 \quad (2.9)$$

It is to notice that  $v_{\text{eff}}$  is dependent on  $\rho$ , which makes the wave functions and therefore the equation for the density dependent on  $\rho$ . Thus, the density can only be calculated by self-consistent iteration. A suitable test density leads to an effective potential, which leads to the KS-wave functions, which then lead to a new density. This procedure is repeated until the density and wave function do not change any more.

That method can, however, only be applied if an expression for  $F_{WW}$  is known. Typically the problem is simplified by separating the energy of a classical interacting electron density, the so-called Hartree-term:

$$F_{WW} = E_H + E_{xc} = \frac{1}{2} \int \int \frac{\rho(r)\rho(r')}{|r-r'|} dr dr' + E_{xc} \quad (2.10)$$

The term  $E_{xc}$  is known as exchange-correlation energy and includes all quantum mechanic

---

<sup>1</sup>This assumption holds true if the system is describable using a single Slater-Determinant

exclusive interactions between the electrons. The effective potential is then given by:<sup>[8]</sup>

$$v_{\text{eff}} = v + \int \frac{\rho(r')}{|r - r'|} dr' + \frac{\delta E_{\text{xc}}}{\delta \rho} \quad (2.11)$$

Inserting this expression into equation 2.8 one arrives at the Kohn-Sham equation, which is solved consecutively with the density until no more change occurs:<sup>[8]</sup>

$$\left( -\frac{1}{2} \nabla^2 + v + \int \frac{\rho(r')}{|r - r'|} dr' + \frac{\delta E_{\text{xc}}}{\delta \rho} \right) \phi_i = \epsilon_i \phi_i \quad (2.12)$$

Having the Kohn-Sham wave functions and density identified, the total energy can be calculated using equation 2.4:

$$\begin{aligned} E &= F_{\text{KS}} + E_{\text{H}} + E_{\text{xc}} + E_{\text{e-n}} \\ &= \sum_i^{N_e} \langle \phi_i | \nabla^2 | \phi_i \rangle + \frac{1}{2} \int \int \frac{\rho(r) \rho(r')}{|r - r'|} dr dr' + E_{\text{xc}} + \int v(r) \rho(r) dr \end{aligned} \quad (2.13)$$

Until now the electronic system is described with few assumptions. The term  $E_{\text{xc}}$ , called exchange-correlation functional, includes the pure quantum mechanical effects of the system. This term is, however, unknown and has to be approximated. There are several approximations for this term, which can be categorized in several classes, from which the most used ones are the local density approximation (LDA), the generalized gradient approximation (GGA) and the hybrid functionals. Hybrid functionals will be discussed in a later section, the LDA is dependent only on the electron density and the GGA is additionally dependent on the spacial derivative of the density. In the LDA the exchange-correlation term is calculated on the basis of the homogeneous electron gas. This ansatz therefore requires a certain homogeneity of the system; the density can only vary slowly<sup>[8,10]</sup>. Since the GGA also includes the derivative of the density this restriction can be circumvented and inhomogeneous systems like molecules can be described.<sup>[7,11]</sup> Both LDA and GGA functionals (as well as the DFT generally) are nowadays standard tools in chemistry and solid state physics – which can be seen easily from the at least 27,927 publications published alone in 2022 which employ DFT.<sup>[12]</sup>

### 2.3. Molecular dynamics using density functional theory

With the DFT the ground state energy of a solid with a fixed ionic potential can be calculated. To go from a static ion configuration to a dynamic one, one has to incorporate the movement of the ions. As the ions are comparatively heavy, quantum effects like tunneling are rare (see also Born-Oppenheimer approximation). Therefore, the ionic movement is usually included by integrating Newtons equations of motion. This approximation is also known as classical path approximation.<sup>[13]</sup> Integrating Newtons equation of motion requires the calculation of the forces acting on the ions. Classically the force is given by  $F_i = \frac{\partial E}{\partial R_i}$ . Calculating this for each ion is rather costly, which is why instead the Hellmann-Feynman theorem is employed: For any parameter  $\lambda$  holds (under the condition that  $\frac{\partial H}{\partial \lambda}$  exists):<sup>[14-16]</sup>

$$\frac{\partial E}{\partial \lambda} = \frac{\partial}{\partial \lambda} \langle \Psi | H | \Psi \rangle = \left\langle \Psi \left| \frac{\partial H}{\partial \lambda} \right| \Psi \right\rangle \quad (2.14)$$

As the Hamiltonian is derivable analytically (see equation 2.13), setting  $\lambda = R_i$  gives an expression for calculating the forces and therefore the possibility to compute a molecular dynamic (MD).

## 2.4. Simulation of the temperature

To incorporate the temperature into a MD the electronic and ionic system have once again to be considered individually. In the electronic system the temperature can lead to excitations of electrons from the valence band into the conduction band. As the temperature is a macroscopic property of a system, which translates in a statistical distribution of microscopic properties, not all valence electrons are excited but only a specific fraction. The excitation statistic for electrons is given by the Fermi-Dirac distribution, which describes the occupation probability of the electronic states:<sup>[1]</sup>

$$W(E) = \frac{1}{\exp\left(\frac{E-\mu}{k_B T}\right) + 1} \quad (2.15)$$

With  $W(E)$  being the occupation probability,  $E$  the energy of an electronic state,  $T$  the temperature,  $k_B$  the Boltzmann constant and  $\mu$  the Fermi energy. Simulating such a statistic is not always possible and will be explained in a later section. The statistic can, however, be discarded in many cases: If isolators or semiconductors are considered, the valence and conduction band are separated by a band gap, which (for typical semiconductors) is between 0.4 eV and 3 eV.<sup>[17]</sup> At room temperature (300 K) the probability for a state which is 0.3 eV above the Fermi energy to be occupied is about  $9 \cdot 10^{-6}$ , therefore basically no redistribution due to the Fermi distribution occurs, which is why the redistribution can be neglected.

The ionic system also has to follow statistics for the temperature; in this case the velocities have to follow the equipartition theorem. The temperature is a measure for the mean velocity of the ions. Setting the thermal energy equal to the kinetic energy leads to:<sup>[18]</sup>

$$\sum_i^N \frac{1}{2} m_i v_i^2 = E_{\text{kin}} = E_T = \frac{3N}{2} k_B T \quad (2.16)$$

A simple method to simulate the temperature is to assign the ions a random initial impulse to fulfil equation 2.16. For this a random number for each spatial coordinate in the range of [-1,1] is assigned to each ion. As the solid body should not move as a whole, the total impulse has to be zero:  $\sum_i \vec{p}_i = 0$ . This is not ensured by random numbers, therefore the impulses are transformed equally to ensure this condition:  $\vec{p}'_i = \vec{p}_i - \frac{1}{N} \sum_i^N \vec{p}_i$ . At last the impulses are scaled with the scaling factor  $\lambda = \sqrt{\frac{E_T}{E_{\text{kin}}(\vec{p}')}}$  to fulfil equation 2.16. After this initial assignment no further control on the temperature is imposed. As with

this restriction no energy can enter or leave the system, ensembles of trajectories using this method are referred to as *NVE* ensembles (particle count  $N$ , volume  $V$  and energy  $E$  are kept constant). This model is suitable if very short timescales are considered or if generally little heat redistribution is expected in the system. Besides the simple modelling this model has the advantage of comparability, since once the starting impulses are generated one can change different parameters in the calculations and compare them with exact the same starting conditions. If, however, systems with more interactions or longer time scales have to be considered this model is not sufficient. Furthermore, the random impulses do not guarantee the simulation of a thermal equilibrium.

To simulate a thermal equilibrium the temperature has to be controlled during the MD. The most simple ansatz for this is to scale the ion velocities after each ionic relaxation. According to equation 2.16 the target temperature  $T_z$  is reached if the current velocities are scaled by  $\sqrt{\frac{T_z}{T(t)}}$ . That leads to a system with a constant temperature. However, this method is not practicable. On one hand, the repeated scaling overpowers the dynamic of the forces in the system, on the other hand, oscillations of the temperature are “normal” in canonic or microcanonic ensembles.<sup>[19]</sup> A more realistic approach is to dampen the scaling. One possibility for this is the Berendsen thermostat, which resembles a coupling to an external heat bath. The Berendsen thermostat controls the scaling using a time constant:<sup>[20,21]</sup>

$$\frac{\partial T(t)}{\partial t} = \frac{1}{\tau}(T_z - T(t)) \quad (2.17)$$

$$\Delta T = \frac{\delta t}{\tau}(T_z - T(t)) \quad (2.18)$$

With  $\tau$  being the time constant. The lower equation is a discretized variant of the top equation, where  $\delta t$  is the relaxation time step. The scaling factor for the ionic velocities is then given by  $\lambda = \sqrt{1 + \frac{\delta t}{\tau} \left( \frac{T_z}{T(t)} - 1 \right)}$ . If  $\tau$  is chosen to be  $\delta t$ , this procedure resembles the direct scaling of the velocities as explained above. In the limit  $\tau \rightarrow \infty$  the velocities are not scaled at all, one gains a microcanonical *NVE* ensemble. Finite values lead to a damped control of the velocities and thus the temperature. As the temperature is controlled the energy of the system cannot be constant, therefore ensembles which such a temperature control are referred to as *NVT* ensembles (particle count  $N$ , volume  $V$  and temperature  $T$  controlled). The Berendsen thermostat is able to simulate a thermal equilibrium, however no canonical ensemble is reached as the Boltzmann-distribution of the velocities is not necessarily fulfilled.<sup>[22]</sup> Therefore, the Berendsen thermostat is useful to generate equilibrail starting configurations, or to conduct simulations where no exact canonical ensemble is needed.

If a canonical ensemble is needed, another thermostat has to be employed. One thermostat capable of doing so is the Nosé-Hoover thermostat<sup>[23]</sup>. This thermostat does not control the temperature with an external heat bath, but introduces an additional internal degree of freedom, an additional “particle”. The system with this “particle” will be referred to as “extended” system  $\tilde{S}$ , while the “real” system  $S$  has the original number of particles. Both systems are coupled to each other with the variable  $s$ :<sup>[19,22,23]</sup>

$$\tilde{r} = r, \quad d\tilde{t} = \tilde{s} dt, \quad \tilde{s} = s, \dot{\tilde{r}} = \tilde{s}^{-1} \dot{r}, \quad \dot{\tilde{s}} = \tilde{s}^{-1} \dot{s} \quad (2.19)$$

These equations shows that  $s$  acts as a time scaling factor between the systems. Now a “mass”  $Q$  and a “velocity”  $\dot{\tilde{s}}$  is assigned to the additional particle in  $\tilde{S}$ . The particle can also be influenced by a potential. The corresponding Lagrange function of  $\tilde{S}$  is given by:

$$L = \sum_i \frac{m_i}{2} \tilde{s}^2 \dot{\tilde{r}}_i^2 - U(\tilde{r}) + \frac{1}{2} Q \dot{\tilde{s}}^2 - g k_B T_0 \ln \tilde{s} \quad (2.20)$$

The last term of this equation corresponds to the potential of the fictitious particle, which is chosen so that a canonical distribution is reached in the System  $S$ . Using the Lagrange function one can derive the equations of motion in  $\tilde{S}$ :<sup>[19,24]</sup>

$$\ddot{\tilde{r}}_i = \frac{\tilde{F}_i}{m_i \tilde{s}^2} - \frac{2\dot{\tilde{s}}\dot{\tilde{r}}_i}{\tilde{s}} \quad (2.21)$$

$$\ddot{\tilde{s}} = \frac{1}{Q\tilde{s}} \left( \sum_i m_i \tilde{s}^2 \dot{\tilde{r}}_i^2 - N_{\text{df}} k_B T_0 \right) \quad (2.22)$$

While these equations results in a canonical ensemble in  $S$ , the time steps in  $S$  are not equidistant due to the time scaling  $s$ . To remove the explicit dependence on  $s$  the variables are transformed back into the system  $S$  and simplified using  $\gamma = \frac{s}{\dot{s}}$ :<sup>[19,22]</sup>

$$\ddot{r}_i = \frac{F_i}{m_i} - \gamma \dot{r}_i \quad (2.23)$$

$$\dot{\gamma} = \frac{-k_B N_{\text{df}}}{Q} T(t) \left( \frac{T_0}{T} - 1 \right) \quad (2.24)$$

These equations are known as Nosé-Hoover equations, which are solved using equidistant time steps. It can be seen that  $Q$  remains as a parameter. With ever larger values for  $Q$  the system approaches the microcanonical limit, with smaller values for  $Q$  the influence of the thermostat is strengthened and the forces acting in  $S$  become more and more neglectable. In order to choose  $Q$  correctly the effective relaxation time  $\tau$  is introduced with  $\tau^2 = \frac{Q}{N_{\text{df}} k_B T_0}$ . For an adequate description of a system the reciprocal value  $\frac{1}{\tau}$  is chosen to be of the order of the characteristic frequency of the system, which brings the oscillations due to the thermostat to an order equal to the oscillations in the microcanonical ensemble<sup>[19,22]</sup>.

It is to notice that the Nosé-Hoover formalism requires apart from the energy conservation in the extended system  $\tilde{S}$  that the center of mass does not move<sup>[24]</sup> and that  $S$  is an ergodic system, i.e. that each accessible mircostate is assumed by a system given enough time (or more concrete, the time average of one system is the same to its ensemble average).<sup>[22,25]</sup> Especially for small or stiff systems this is not always the case, which leads to unphysical oscillations when the thermostat is applied.<sup>[25]</sup> To circumvent this problem one can couple the extended system  $\tilde{S}$  with another system  $\tilde{S}$  and build a chain of Nosé-Hoover

thermostats. The accordingly called Nosé-Hoover-chain formalism enables the description for non ergodic systems.<sup>[25]</sup>

## 2.5. Phonons

Besides using molecular dynamics, the phonons of a crystal can also be used to gain insight on the dynamic of the system. As established in chapter 2.1, the full description of a system can generally be divided into two differential equations, one for the electronic system in a fixed potential and one for the ionic system with stepwise constant electronic forces,  $-\frac{1}{2} \sum_k \frac{m_e}{M_k} \frac{\partial^2}{\partial R_k^2} + E(R))\Phi(R) = \epsilon\Phi(R)$ .  $E(R)$  is the total energy gained from DFT plus the ion-ion interaction energy,  $\sum_{k < l} \frac{Z_k Z_l}{|R_k - R_l|}$ . Would one solve this equation, one would gain the complete energy surface for the ions and thus could predict the behaviour of the systems dynamics. Such a complete solution is rarely possible, instead a Taylor expansion of the energy around the equilibrium coordinates is done:

$$E = E_0 + \sum_{k,\alpha} \frac{\partial E}{\partial u_{k,\alpha}} \cdot u_{k,\alpha} + \frac{1}{2} \sum_{k,\alpha,k',\alpha'} u_{k,\alpha} \cdot \underbrace{\frac{\partial^2 E}{\partial u_{k,\alpha} \partial u_{k',\alpha'}}}_{I_{\alpha,\alpha'}^{k,k'}} \cdot u_{k',\alpha'} + \dots \quad (2.25)$$

Here, the  $u_{k,\alpha}$  are the displacements of the  $k$ th atom in direction  $\alpha$  from its equilibrium position. The constant zeroth order term is of no concern and can be renormalized, the first order term is 0, as the first derivative of the energy are the forces, which are by construction 0 at the equilibrium position. Omitting the third and higher orders, the second order term describes collective oscillations in the crystal, the so-called phonons.<sup>[1]</sup> By assuming a plane wave solution for the oscillations and by Fourier transforming the force-constant matrix  $I_{\alpha,\alpha'}^{k,k'}$  (see equation 2.25) one arrives at following eigenvalue equation:<sup>[1,26]</sup>

$$D_{\alpha,\alpha'}^{k,k'}(q) \quad \epsilon_{mk,\alpha q} = \quad \omega_{m,q}^2 \epsilon_{mk,\alpha q} \\ \text{with } D_{\alpha,\alpha'}^{k,k'}(q) \quad = \quad \frac{1}{\sqrt{M_k M_{k'}}} \sum_a I_{\alpha,\alpha'}^{k,k'} e^{-i\mathbf{q} \cdot \mathbf{r}_a} \quad (2.26)$$

Here, the dynamical matrix  $D$ , the phonon wave vector  $q$ , the polarization vector  $\epsilon_{mk,\alpha q}$  and the phonon frequency  $\omega$  are introduced. From this equation one can see that each phonon mode has a specific frequency, and that all atoms experience displacement in one phonon mode. The phonon thus are indeed collective oscillations of the atoms. Solving this equation one gains  $3N_{\text{nucl}}$  phonon modes which are linear independent of each other. Any displacement can therefore be decomposed into the phonon modes. It is to note that like electrons the phonons also show particle character, their energies are quantized via their frequency. Unlike electrons however, phonons are bosons, meaning they are not subject to the Pauli principle and one mode can be occupied several times, with a higher occupation relating to higher amplitudes of the oscillations.<sup>[27,28]</sup> This results in an other occupation probability, the Bose-Einstein distribution  $n = \frac{1}{e^{\frac{\hbar\omega}{kT}} - 1}$ .<sup>[1,29]</sup> Since this distribution is dependent on temperature and frequency, one gains insight in the dynamics, as high frequency modes are more probable to occur at high temperatures.

While diagonalizing equation 2.26 is straightforward from a computational point of view, the challenge in computing phonons is the construction of the force constant matrix  $I$ . One possibility is to manually displace the atoms in a periodic manner to explicitly calculate the needed derivatives. This method is referred to as frozen phonon approach.<sup>[30,31]</sup> However, it requires the use of supercells to access different phonon wave vectors.<sup>[26,31,32]</sup> A more elaborate approach is to consider the variation of the potential as a perturbation of the system. Following the Hellmann-Feynman theorem, the second derivative of the energy is given by:<sup>[32]</sup>

$$\frac{\partial^2 E}{\partial R_i \partial R_j} = \int \frac{\partial^2 V(r)}{\partial R_j \partial R_k} \rho(r) dr + \int \frac{\partial \rho(r)}{\partial R_i} \frac{\partial V(r)}{\partial R_j} dr + \frac{\partial^2 E_N(R)}{\partial R_I \partial R_J} \quad (2.27)$$

With  $R$  being nuclear coordinates,  $V$  the electron-ion potential and  $E_N$  the ion-ion interaction. This equation includes the linear response of the density,  $\frac{\partial \rho(r)}{\partial R_i}$ . The linear response can be evaluated by doing a Taylor expansion for the density, the Schrödinger equation and the effective potential (equations 2.9, 2.8 and 2.11) for the disturbed system and dropping each term after the first order. By calculating the disturbed wave functions and disturbed energies using first order perturbation theory one arrives at a self-consistent set of coupled equations for the disturbed values:<sup>[32]</sup>

$$\Delta \rho(r) = 2 \sum_i^{N_e} \phi_i^*(r) \Delta \phi_i \quad (2.28)$$

$$\left( -\frac{1}{2} \nabla^2 + v_{\text{eff}} - \epsilon_i \right) \Delta \phi_i = -(\Delta v_{\text{eff}} - \Delta \epsilon_i) \phi_i \quad (2.29)$$

$$\Delta v_{\text{eff}} = \Delta v + \int \frac{\Delta \rho(r')}{|r - r'|} dr' + \left. \frac{\delta E_{\text{xc}}}{\delta \rho} \right|_{\rho=\rho(r)} \Delta \rho(r) \quad (2.30)$$

$$\Delta \epsilon_i = \int \phi_i^* \Delta v_{\text{eff}} \phi_i dr \quad (2.31)$$

Where the  $\Delta$  designates the disturbed quantities. While these equations are coupled and have to be solved self-consistently, they bear the advantage to be projectable onto different phonon wave vectors, which on one hand, again simplifies the solution of the equations and on the other hand, allows access to individual phonon modes without the need of a supercell.<sup>[32]</sup> Each phonon calculation in this work uses this perturbation theory approach and was calculated using the PHonon code from QUANTUM ESPRESSO.<sup>[33,34]</sup>

## 2.6. Excited states within density functional theory

As already shown in its derivation, the density functional theory is a ground state theory. However, if we want to describe a full electron dynamic also systems with excited electronic states, for example due to optical excitation, have to be considered. To describe the properties of excited states in general perturbation approaches like the GW approximation or the time dependent DFT can be used.<sup>[35,36]</sup> However, these methods are numerically expensive and therefore only partly useful for dynamics which encompass large time frames with many relaxation steps. Nevertheless one is able to gain insight on those

states approximately with the DFT by introducing small modifications.

One possibility is to look at a charged system. If one wants to occupy the lowest unoccupied state (LUMO) in a system, one can use a system with an additional electron, thus the formerly unoccupied state is now occupied. It has to be stressed that this is of course no excitation of the system, as the number of particles is not conserved. This kind of description is only possible if the “origin” of the electron would have little or no influence on the system, especially on the excited electron. A possible origin for the electron would be deep trap states which usually only interact locally if at all with the system. Due to this restriction this ansatz is very limited in its use. It is to note, that by adding one electron to a neutral system one usually arrives at an uneven electron number and an overall spin in the system. This requires switching from the Kohn-Sham equations (equation 2.12) to the spin-unrestricted KS-equation, where the one-particle wave functions, and (potentially) the exchange-correlation functional are spin dependent. Furthermore, another restriction has to be fulfilled, the integral over the spin density  $m(r) = \sum_i^{N_{\text{el}}^{\uparrow}} \phi_i^{\uparrow} - \sum_i^{N_{\text{el}}^{\downarrow}} \phi_i^{\downarrow}$  has to equal the overall spin.<sup>[37]</sup> While this method is quite restricted it is by no means without use; most notably one is able to gain an estimate of the excitation energy by adding and removing electrons. The first excitation energy is given by the energy needed to remove one electron from the system (ionization energy) added to the energy the system gains by adding one electron (electron affinity). This results in  $E_{\text{ex}} = E(N+1) + E(N-1) - 2E(N)$ , where  $N$  is the number of electrons in the ground state and  $E$  are the respective total energies. This method is also referred to as  $\Delta$ -scf.<sup>[38]</sup>

A more flexible possibility is the usage of the “constrained” density functional theory (c-DFT). While DFT aims to describe the ground state, c-DFT can access excited states. c-DFT is an umbrella term for DFT methods which have to fulfil one or several secondary conditions during the minimization of the energy, therefore a “ground state” with additional restrictions is calculated.<sup>[39,40]</sup> These restrictions can take various shapes, in this work the constraint of certain KS states being occupied and total magnetizations is utilized. To describe excited states by special KS states an additional condition for the occupation numbers is introduced. The occupation numbers show which (single-particle) electronic eigenstates are occupied, and are introduced to the DFT at the calculation of the electronic density:<sup>[41,42]</sup>

$$\rho = \sum_i^{N_e} |\phi_i|^2 \quad \rightarrow \quad \rho = \sum_i^{N_{\text{KS}}} f_i |\phi_i|^2 \quad (2.32)$$

Where  $f_i$  are the occupation numbers for the eigenstates which can have values between 0 and 1. In the case of “normal” DFT it holds  $f_i = 1$  if  $i \leq N_e$  and  $f_i = 0$  otherwise. The density is therefore constructed in a non-Aufbau scheme, this method is sometimes also referred to as  $\Delta$ -scf<sup>[42]</sup>. To avoid confusion with the  $\Delta$ -scf excitation energy the terminology c-DFT will continue to be used. By changing the values for  $f_i$  one is able to describe different excited states within c-DFT. An one-electron excitation from the highest valence band to the lowest conduction band for example is given by:

$$f_i = \begin{cases} 1.0 & i < N_e \\ 0.0 & i = N_e \\ 1.0 & i = N_e + 1 \\ 0.0 & i > N_e + 1 \end{cases} \quad (2.33)$$

The constraint to a certain magnetization is a variant of this method, where consecutively the highest occupied band of one spin channel is emptied and the highest unoccupied band of the other spin channel is filled, until the desired magnetization is reached. It has to be emphasized that this description is only an approximation. Strictly speaking, the KS eigenstates of the DFT have no physical meaning except for resulting in the correct electron density by summation. However, by the means of empiric observation it could be shown that the KS one-particle states can approximate the true states of the system. Especially for low excited states the c-DFT produces reliable results.<sup>[42]</sup> For example c-DFT shows good results in describing Indium nanowires on silicon<sup>[43]</sup>, organic dyes<sup>[44]</sup> and Rydberg states.<sup>[45]</sup> Furthermore, c-DFT enables the access to higher excitation and to specific states, like a triplet excitation. Similar to  $\Delta$ -scf, c-DFT also allows the calculation of excitation energies, where the excitation energy is given straightforward as  $E_{text{extrmex}} = E^*(N) - E(N)$ , where  $E^*(N)$  is the total energy of the c-DFT excited state, and  $E(N)$  the total energy of the ground state.<sup>[46]</sup> However, since c-DFT is based on further approximations, the  $\Delta$ -scf excitation energy, if available, is usually more accurate. The c-DFT, DFT and molecular dynamics simulations conducted in this work are calculated using the QUANTUM ESPRESSO pw program package.<sup>[33,34]</sup>

## 2.7. Interband transitions

With the possibility to describe excited states one can principally conduct molecular dynamics for optically excited system. However, one excited state does not describe the whole excitation dynamic. For a typical optical excitation the electron is not excited to the lowest conduction band, but can reach energetically higher states depending on the excitation energy. The excited electron then begins to relax, where on one hand, its state cross energetically lower states and on the other hand, the electron can “hop” to other states. By the means of these processes the electron relaxes after a while to the lowest state in the conduction band. Usually, the electron stays in this state for a considerably longer time than in the higher states, as the band gap to the ground state is considerably larger than to the other states.<sup>[47]</sup> This leads to the fact that most effect due to the optical excitation happen in this first excited state. In photo chemistry this finding is referred to as Kasha’s rule: The electrons in molecules relax fast and without emission to the lowest excited state.<sup>[47]</sup>

In order to go beyond Kasha’s rule and to describe the transitions directly one can use the Schrödinger equation, in which the nuclei potential is set to be fixed according to the Born-Oppenheimer approximation:

$$i\hbar \frac{\partial}{\partial t} |\Psi\rangle = H_{\text{el}}(r, R(t)) |\Psi\rangle \quad \text{with} \quad |\Psi(r, R, t)\rangle = \sum_j c_j(t) |\phi(r, R(t))\rangle \quad (2.34)$$

Here  $|\Psi\rangle$  is the many-particle wave function and  $H_{\text{el}}(r, R(t))$  the electronic Hamiltonian which depends parametrically on the positions of the ions  $R$ . The many-particle wave function is expended in the bases of its orthonormal eigenstates  $\phi_k$  and projected onto a single state:<sup>[48,49]</sup>

$$\begin{aligned} i\hbar \frac{\partial}{\partial t} \sum_j c_j(t) |\phi_j(r, R(t))\rangle &= H_{\text{el}}(r, R(t)) \sum_j c_j(t) |\phi_j(r, R(t))\rangle - |\langle \phi_k | \cdot \\ \Rightarrow i\hbar \dot{c}_k &= \sum_j c_j \left( V_{kj} - i\hbar \left\langle \phi_k \left| \frac{\partial \phi_j}{\partial t} \right. \right\rangle \right) \end{aligned} \quad (2.35)$$

The matrix element  $V_{kj}$  is given by  $\langle \phi_k | H_{\text{el}} | \phi_j \rangle$ . With this equation the occupation numbers  $c_k$  are developed, which are the probabilities to find a system in the given electronic state out of a set of evenly prepared systems. The specification of an ensemble of systems is important, as only a statistical statement for the whole quantum mechanical ensemble is given, and no statement for the occupation in a single MD trajectory is made. This means that on one hand, for the complete description of an excited dynamic a statistical analysis of several pure state trajectories has to be conducted, and on the other hand, a rule has to be found for the switching of single trajectories between pure states in a way that equation 2.35 is fulfilled.

One such rule is Tully's fewest switches surface hopping (FSSH) algorithm. The idea behind this algorithm is to have the trajectories jump as little as possible between the states. Assuming the opposite shows the reason for that: If many trajectories oscillate between the states, the movement of the particles is governed by a mean force, as the forces of the states alter as well. This behaviour is, however, unphysical, since as soon as a particle enters a region of weak interaction, it should behave according to the state it had while entering this region.<sup>[48]</sup> If one would use the Schrödinger occupation probabilities directly as hopping probabilities, the trajectories could also switch states in this weak interaction regions. To circumvent this problem the constraint of switching as little trajectories as necessary is introduced – if the occupation probabilities do not change, the trajectories will not change either. With this condition the probability for a single trajectory to hop to another state is given by:<sup>[48]</sup>

$$\begin{aligned} P_{k \rightarrow j} &= \frac{b_{jk} \Delta t}{a_{kk}} \quad \text{with} \\ b_{kl} &= 2 \left( \Im(a_{kl}^* V_{kl}) - \Re \left( a_{kl}^* \left\langle \phi_k \left| \frac{\partial \phi_l}{\partial t} \right. \right\rangle \right) \right) \end{aligned} \quad (2.36)$$

Here the  $a_{kl}$  are the elements of the density matrix which is constructed with  $a_{kl} = c_k c_l^*$ . The hopping probability is therefore directly governed by the interaction of the wave functions at the specific time point as seen in the quantity  $b_{kl}$ .

While the FSSH algorithm itself is now described completely, it can not be used directly for DFT based MDs, as neither the multi-particle wave functions nor their eigenbasis are known. A typical ansatz is, analogous to the Hartree-Fock theory (see chapter 2.8.3), to approximate the multi-particle wave function with the Slater determinant of the KS single particle wave functions. Since the KS-eigenvalues are already used to approximate the many particle eigenvalues (like in the case of band structures), this approximation seems

reasonable. If only states from a single DFT calculation are used, it further simplifies the numerical analysis. The KS-wave functions are orthogonal and diagonalize  $H_{\text{el}}$ , therefore  $V_{kl}$  simplifies to  $\delta_{kl}\varepsilon_k$  and the product of Slater determinants simplifies to a scalar product of one-particle orbitals.<sup>[49]</sup> This method is a wide spread tool for the calculation of non-adiabatic MDs.<sup>[50]</sup> However, it lacks a direct calculation of the excited states, and the forces used to develop the trajectory stem from the ground state and are therefore independent from the excited state, an approximation also known as “neglect of back reaction” (NBRA).<sup>[50]</sup>

In order to describe the excited states more accurately and go beyond the NBRA approximation, in this work the excited states are calculated directly. As already shown, c-DFT calculations are capable of doing so. As these calculations are independent from each other, the wave functions do not stem from a single basis and are no longer orthogonal. Expanding the Schrödinger equation with a non-orthogonal basis set results analogous to 2.35 in:<sup>[51,52]</sup>

$$i\hbar \sum_j S_{kj} \frac{\partial c_k(t)}{\partial t} = \sum_j \left( V_{kj} - i\hbar \left\langle \phi_k \left| \frac{\partial \phi_j}{\partial t} \right. \right\rangle \right) \quad (2.37)$$

Where  $S_{kj} = \langle \phi_k | \phi_j \rangle$  represents the overlap matrix. This equation is solvable, however it is more complicated and hard to interpret. Therefore, one usually performs a transformation to orthogonalize the orbitals. Here the orthogonalization chosen is the orthogonalization in adiabatic molecular orbitals (AMO). As a first step, the non-orthogonal (diabatic) Hamilton matrix is constructed:

$$H_{kj}^{\text{DMO}} = \frac{E_k^{\text{dia}} + E_j^{\text{dia}}}{2} S_{kj} \quad (2.38)$$

With  $E_k^{\text{dia}}$  are the total energies of the corresponding c-DFT calculations. Using this matrix, the transformation matrix  $T$  is constructed as solution to the following eigenvalue problem, and then used to transform the wave functions:<sup>[51]</sup>

$$H^{\text{DMO}} T = S H^{\text{AMO}} T, \quad H^{\text{AMO}} = \text{diag}(\epsilon^{\text{AMO}}) \quad (2.39)$$

$$|\Psi^{\text{AMO}}\rangle = |\Psi\rangle T \quad (2.40)$$

Here  $\epsilon^{\text{AMO}}$  are the eigenvalues (eigenenergies) of  $H^{\text{AMO}}$ , which is the Hamilton matrix in the orthogonal (adiabatic) basis. With this transformation  $V_{kl}$  again simplifies into a delta function and the Schrödinger equation is again directly solvable.

In practical application for a trajectory one ionic relaxation step is conducted and the wave functions for both start- and end position are calculated using c-DFT calculation and the scheme explained above. The scalar product is calculated as a finite difference between the Slater determinants of those positions. After the transformation the Schrödinger equation is solved, the occupation numbers developed, and the hopping probabilities are computed using the FSSH algorithm. Using random generated numbers it is decided whether the

trajectory hops to a different state (and to which). The now occupied state is also referred to as active state. The forces of the active state are then used for another ionic relaxation step, and the procedure begins anew.<sup>[52]</sup> A graphical summary of the surface hopping procedure is shown on the title page of the theory section (p. 4). The surface hopping calculations conducted in this work were performed using the (slightly modified) LIBRA-X program package.<sup>[52]</sup> The modifications are covered in section A.

## 2.8. Localized states in density functional theory

### 2.8.1. Problems of the density functional theory

As already seen in previous sections, the density functional theory can be principally exact, but the exchange-correlation energies have to be approximated and there are restrictions due to the numerics, like the choice of the basis set. This leads to errors and problems, of which the most relevant for this work, the delocalization error, will be explained in further detail. The delocalization error is an umbrella term for different effects which makes strongly localized electron densities difficult to describe in DFT, leading to the tendency for the density to over-delocalize in DFT. One such effect is due to the basis set. Usually the KS equations are not solved in real space but in the reciprocal  $k$  space. This is done since crystals are periodic structures, what, according to Bloch's theorem, leads to wave functions consisting of a lattice-periodic function and a phase factor. Therefore, plane waves are a natural choice for the basis set. As already stated, only a limited number of plane waves can be considered, and low wave numbers are preferred over high wave numbers. A strong localization in real space, however, corresponds to a delocalization in reciprocal space, meaning that many plane waves are needed for the description<sup>[3]</sup>, making the basis set a limiting factor for the localization. This problem is a minor one though, as it can partially be mitigated by the usage of fitting pseudo potentials and a sufficiently high cutoff energy.

Another more fundamental problem poses the self interaction error (SIE). As the name states, it is an error due to an unphysical interaction of the electron density with itself. The cause for this error lies in the Hartree term. The Hartree term  $E_H = \frac{1}{2} \int \int \frac{\rho(r)\rho(r')}{|r-r'|} dr dr'$  represents the classical Coulomb interaction between the electrons. This term is only dependent on the whole density  $\rho$ , there is no possibility to differentiate between the single electrons. Therefore, one electron can interact with itself, the additional Coulomb repulsion leads to the delocalization of the electrons.<sup>[53,54]</sup> Principally this error should be compensated by the exchange-correlation functional; however, since this functional is only approximated this compensation does not occur fully. There are methods to counteract this error explicitly like the Perdew-Zunger correction.<sup>[55]</sup> However, those methods are often numerical unstable and/or have missing error compensation.<sup>[56]</sup> This is why usually other methods are used to compensate the SIE. Two of them, the DFT+U method and the hybrid functionals, are explained in the following sections.

### 2.8.2. DFT+U

The DFT+U method is based on the Hubbard model. The Hubbard model is a tight binding model for solid states and describes electrons which are localized at atomic orbitals placed in a fixed lattice. These electrons are tightly bound, which means that there is no long range interaction between the electrons. The electrons experience only an “on-site” electron-electron interaction (corresponding to a potential in the Hamiltonian), and

a nearest neighbour interaction which includes the possibility for one electron to “hop” to an adjacent site (corresponding to the kinetic energy of the electron). Using the second quantization procedure, the Hamiltonian can be written as:<sup>[57,58]</sup>

$$H_{Hub} = U \sum_i n_{i\uparrow} n_{i\downarrow} - t \sum_{\langle i,j \rangle, \sigma} (c_{i,\sigma}^\dagger c_{j,\sigma} + h.c.) \quad (2.41)$$

The indices  $\langle i, j \rangle$  include all nearest neighbour pairs,  $n_{i\uparrow}$  and  $n_{i\downarrow}$  are the spin dependent number operators at the  $i$ -th atom and  $c_{i,\sigma}^\dagger$  and  $c_{j,\sigma}$  are the spin dependent creation and annihilation operators.  $t$  scales the amplitude for the electron hopping, while  $U$  controls the strength of the on site interaction. The ratio between  $U$  and  $t$  dictates the eigenenergies and electron distribution.<sup>[58]</sup>

The idea of the DFT+U method is to incorporate an explicit on site interaction correction to the regular DFT calculation (the  $U$  term in the Hubbard model). The  $t$  term is not included explicitly, the kinetic energy of the electrons is described well by the DFT. This correction is included by adding the site dependent  $U$  term and subtracting any on site interaction (also called double counting term) due to DFT. A general form for the corrected energy of the system is given by:<sup>[58]</sup>

$$E_{DFT+U}[\rho] = E_{DFT}[\rho] + E_{Hub}[\{n_{mm'}^{I\sigma}\}] - E_{dc}[\{n^{I\sigma}\}] \quad (2.42)$$

With  $E_{DFT}[\rho]$  being the energy of the regular DFT calculation,  $E_{Hub}[\{n_{mm'}^{I\sigma}\}]$  the energy due to the Hubbard-U term (which is dependent on the occupation matrices of the localized states  $\{n_{mm'}^{I\sigma}\}$ ) and  $E_{dc}$  is the on-site energy included in the DFT calculation (which is dependent on the number of localized electrons). The occupation matrices of the localized states are constructed using the projection of KS wave function onto a localized basis set, atomic orbitals for example:  $n_{mm'}^{I\sigma} = \sum_{k,\nu} f_{k\nu}^\sigma \langle \Psi_{k\nu}^\sigma | P_{mm'}^I | \Psi_{k\nu}^\sigma \rangle$ . As the Hubbard model is only applicable for strongly localized states, the correction is also only applied to electrons which have the tendency to localize strongly, namely d and f electrons. The other electrons are usually more delocalized and therefore not subject to Hubbard U corrections and are described by the means of usual DFT.

The exact form of  $E_{Hub}$  and  $E_{dc}$  is not set in stone, there is variety especially for the double counting term. An often used option is to compare the  $U$  term with the Hartree-Fock theory (see below), in which the on-site electron-electron interaction is written as:<sup>[57,58]</sup>

$$\begin{aligned} E_{Hub}[\{n_{mm'}^I\}] &= \frac{1}{2} \sum_{\{m\}, \sigma, I} \left\{ \langle m, m'' | V_{ee} | m', m''' \rangle n_{mm'}^{I\sigma} n_{m''m'''}^{I-\sigma} \right. \\ &\quad \left. + (\langle m, m'' | V_{ee} | m', m''' \rangle - \langle m, m'' | V_{ee} | m''', m' \rangle) n_{mm'}^{I\sigma} n_{m''m'''}^{I\sigma} \right\} \end{aligned} \quad (2.43)$$

Here  $V_{ee}$  is the electron-electron Coulomb potential. The double counting term has the form:<sup>[58]</sup>

$$E_{\text{dc}} [\{n_{mm'}^I\}] = \sum_I \left\{ \frac{U^I}{2} n^I (n^I - 1) - \frac{J^I}{2} [n^{I\uparrow} (n^{I\uparrow} - 1) + n^{I\downarrow} (n^{I\downarrow} - 1)] \right\} \quad (2.44)$$

With  $U$  being again the on site interaction and  $J$  the exchange interaction (which is included in DFT by means of the exchange-correlation functional).

Using a multipol expansion of the electron interaction as well as a mean for the interaction integrals the Hubbard term can be written as:<sup>[58]</sup>

$$\langle m, m'' | V_{\text{ee}} | m', m''' \rangle = \sum_k a_k (m, m', m'', m''') F^k , \quad (2.45)$$

$$F^0 = U = \frac{1}{(2l+1)^2} \sum_{m,m'} \langle m, m' | V_{\text{ee}} | m, m' \rangle , \quad (2.46)$$

$$\frac{F^2 + F^4}{14} = J = \frac{1}{2l(2l+1)} \sum_{m \neq m', m'} \langle m, m' | V_{\text{ee}} | m', m \rangle \quad (2.47)$$

Here  $F$  are the radial Slater integrals of the Coulomb interaction and the  $a^k$  products of Clebsh-Gordan coefficients (which are only dependent on the angular part of the wave function). Depending on the azimuthal quantum number of the state  $m$ , only a limited number of Slater integrals is needed ( $F^0, F^2, F^4$  for d electrons and additionally  $F^6$  for f electrons).

This formulation of the Hubbard correction is invariant of the rotation and therefore independent on the choice of basis set.<sup>[59]</sup> However, it is complicated as two parameters,  $U$  and  $J$ , have to be optimized. In this work a simplified variant is utilized where  $J$  is neglected, only the 0-th term of the multipol expansion is considered. This also means neglecting the exchange correction, which therefore is only applied at the level of the DFT exchange-correlation functional. The resulting inaccuracies can, however, often be compensated by adjusting the  $U$  parameter accordingly. This result in following expression for the energy correction:<sup>[57,58]</sup>

$$\begin{aligned} E_{\text{U}} [\{n_{mm'}^{I\sigma}\}] &= E_{\text{Hub}} - E_{\text{dc}} \\ &= \sum_I \frac{U^I}{2} \text{Tr}[n^{I\sigma} (1 - n^{I\sigma})] \end{aligned} \quad (2.48)$$

Choosing the localized orbitals in a way that the occupation matrices are diagonalized it holds:

$$E_{\text{U}} = \frac{U}{2} \sum_{I,\sigma} \sum_i \lambda_i^{\sigma I} (1 - \lambda_i^{\sigma I}) \quad (2.49)$$

Here  $\lambda_i^{I\sigma}$  are the eigenvalues of the occupation matrices. This equation shows that the

Hubbard energy is minimized if the localized orbitals are either completely occupied (1) or unoccupied (0). Usually this leads to a stronger localization of the electrons and thus counteracting the self interaction error. In explicit, if an orbital is more than half occupied before the Hubbard correction is applied, it tends to be occupied fully after and vice versa.<sup>[60]</sup>

This model has  $U$  as its only parameter to be chosen. The value for  $U$  can be adjusted manually to reproduce experimental results like the electron paramagnetic resonance spectrum. Alternatively  $U$  can be chosen in a way to counteract another inherent error of DFT, the derivative discontinuity error. The derivative discontinuity error describes the wrong behaviour of the DFT total energy in respect to a fractional electron number. In reality the energy would have to change piecewise linearly with discontinuities at integer electron numbers. DFT, however, predicts a quadratic behaviour.<sup>[61,62]</sup> Since according to Janak's theorem the KS eigenvalues are equal to the derivative of the total energy in regard to the occupation numbers,<sup>[63]</sup> the derivative discontinuity error causes the band gap to be underestimated.<sup>[62]</sup> As it can be seen in equation 2.48, the Hubbard-U correction also shows a quadratic behaviour with changing fractional occupation (of the localized states). With a fitting choice of  $U$  one can reproduce the piecewise linear behaviour of the energy and thus increase the band gap.<sup>[58,59]</sup>

In summary DFT+U is able to describe localized states better than plain DFT and predict the band gaps and energies more precise. In some cases (like NiO and La<sub>2</sub>CuO<sub>4</sub>) using DFT even results in qualitative wrong results while DFT+U describes the system accurately.<sup>[64,65]</sup>

### 2.8.3. Hybrid functionals

Another method to better describe the localization are hybrid functionals. In contrast to the DFT+U method the localization is not forced explicitly, but rather a certain quantum mechanical aspect, the exchange interaction is described more accurately. The exchange interaction is a pure quantum mechanical effect due to the indistinguishability of identical particles. For fermions the many particle wave function is antisymmetric, it changes sign upon the exchange of two particles. However, if two identical particles are swapped, the wave function remains the same, which means that the wave function has to be equal to zero. Therefore, there can be no two fermions which occupy the same quantum state, a fact known as Pauli principle.<sup>[66,67]</sup> This results in a repulsive "force" between the fermions. Since electrons are also fermions they experience a repulsion both to the Coulomb interaction as due to the Pauli principle. Since the DFT does not use many-particle wave functions let alone their symmetries, the exchange interaction is not described intrinsically in the DFT and has to be approximated in the fittingly called exchange-correlation functional. As basis for the approximation (in the LDA approximation) the exchange interaction of a homogeneous electron gas in dependence of the electron density is used. However, this approximation is not valid for all systems, it fails especially for highly localized electron densities (which by definition break the assumption of a homogeneous density). That problem can be bypassed by using hybrid functionals, which include the exchange interaction explicitly. In order to explain this in more detail, the Hartree-Fock theory has to be discussed.

The Hartree-Fock theory is a method to (approximately) solve the many body problem of several electrons in a fixed potential, namely  $H\Psi = E\Psi$  with  $H =$

$\sum_k^{N_e} \left( -\frac{\hbar^2}{2m_e} \Delta_k - \sum_K^{N_k} \frac{Z_K}{|r_k - R_K|} + \frac{1}{2} \sum_{l,l \neq k}^{N_e} \frac{e^2}{|r_k - r_l|} \right)$ . One starts with an ansatz for the many particle wave function. This ansatz consist of a product of several-one particle wave functions. To include the antisymmetry of the wave function a Slater determinant is employed:[68]

$$\Psi = \begin{vmatrix} \psi_1(r_1)\chi_1(m_s) & \psi_2(r_1)\chi_2(ms) & \cdots & \psi_N(r_1)\chi_N(ms) \\ \psi_1(r_2)\chi_1(m_s) & \psi_2(r_2)\chi_2(ms) & \cdots & \psi_N(r_2)\chi_N(ms) \\ \vdots & \vdots & \ddots & \vdots \\ \psi_1(r_N)\chi_1(m_s) & \psi_2(r_N)\chi_2(ms) & \cdots & \psi_N(r_N)\chi_N(ms) \end{vmatrix} \quad (2.50)$$

Here the  $\psi$  represent the spacial part of the one-particle wave functions and the  $\chi$  the spin part of the wave functions. Both spacial and spin part are orthonormal, it holds  $\langle \psi_i | \psi_k \rangle = \delta_{ik}$ ,  $\langle \chi_i | \chi_k \rangle = \delta_{ik}$ . Since the Hamiltonian can act only on two spacial parts of the wave functions at once, the calculation of the expectation value separates into a sum over integrals over one to two one-particle wave functions:[1]

$$\begin{aligned} E = & \sum_k \int \psi_k^*(r_k) \left( -\frac{\hbar^2 \Delta_k}{2m_e} + V(r_k) \right) \psi_k(r_k) d^3 r_k \\ & + \frac{1}{2} \sum_{kl, k \neq l} \int \psi_k(r_k)^* \psi_l(r_l)^* \frac{e^2}{|r_k - r_l|} \psi_k(r_k) \psi_l(r_l) d^3 r_k d^3 r_l \\ & - \frac{1}{2} \sum_{kl, k \neq l} \delta_{s_k s_l} \int \psi_k(r_l)^* \psi_l(r_k)^* \frac{e^2}{|r_k - r_l|} \psi_k(r_k) \psi_l(r_l) d^3 r_k d^3 r_l \end{aligned} \quad (2.51)$$

This energy eigenvalue is minimized using Ritz's variation principle with the condition of orthonormal one-particle wave functions. The minimization holds the Hartree-Fock equation:[69]

$$\begin{aligned} & \left( \frac{\hbar^2 \Delta}{2m_e} + V(r) + e^2 \underbrace{\sum_k \int \psi_k^*(r') \frac{1}{|r - r'|} \psi_k(r') d^3 r'}_{= \int \frac{n(r')}{|r - r'|} d^3 r'} \right) \psi_l(r) \\ & - e^2 \sum_k \delta_{s_k s_l} \int \frac{\psi_k^*(r') \psi_l(r') \psi_k^*(r)}{|r - r'|} d^3 r' = \varepsilon_l \psi_l(r) \end{aligned} \quad (2.52)$$

The upper row describes the kinetic energy of the electrons, the ionic potential as well as the classical Coulomb interaction (Hartree-term). The lower row stems from the anti-symmetry of the wave function and is called Fock exchange term. It is to notice that the electron corresponding to the wave function  $\psi_l$  does not interact with the other electrons individually, but rather as a mean potential. Since the equation for the one-particle wave function  $\psi_l$  include all other  $\psi_k$  as well it can be seen that these equations have to be solved self-consistently.

By construction, the Hartree-Fock theory includes the exchange interaction. However, there are also disadvantages to this method. In contrast to the DFT, which can principally

find the exact ground state energy, the Hartree-Fock theory can not, as the choice of a specific ansatz in most cases can not represent the correct wave function. Therefore, the ground state has always a higher energy than it would have in reality.<sup>[70]</sup> Furthermore, the electrons-electron interaction occurs via the bare Coulomb potential rather than via a screened one. This unscreened potential leads to an overestimation of the band gap.<sup>[71]</sup> Last but not least, the probability to find an electron at a specific place is independent on the probabilities of the other electrons, as they only interact due to a mean potential. Therefore, two electrons can exist close to each other without experiencing a stronger Coulomb repulsion. This can lead to a stronger localization of electrons within the Hartree-Fock theory.<sup>[72,73]</sup>

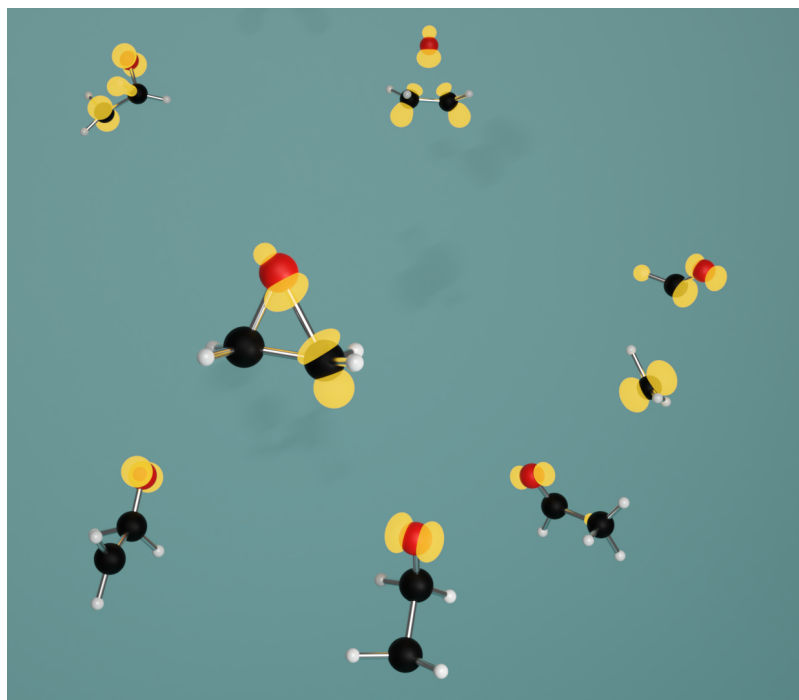
Hybrid functionals now combine the Hartree-Fock theory with the DFT. Formally the exchange part of the exchange-correlation functional of DFT is removed and replaced by the exact exchange of the Hartree-Fock method. In practice first the one-particle wave functions are calculated and optimized as Kohn-Sham wave functions within DFT. Those optimized functions are used for a single iteration for the self-consistent Fock-Term. The therefore corrected wave functions are then again optimized with DFT, this procedure is repeated self-consistently. Since the DFT tends to underestimate the electron localization (and underestimate the band gap) and Hartree-Fock tends to overestimate the electron localization (and overestimate the band gap) the combination of both can cancel out both errors.<sup>[71,74]</sup> Typically not the whole exchange part of the DFT functional is replaced, but only partially. This mixing factor between DFT exchange-correlation functional and exact exchange, often chosen at around 25 % exact exchange, holds another possibility to further optimize the system.

## Results and discussion

For the full description of an optically excited system, several steps have to be taken into account. First, there is the excitation of the system itself, which is an interaction of an electromagnetic field with the solid, which elevates one or several electrons to excited configurations. Second, the electronic and structural relaxation occurs, leading to a lowering of the now occupied electronic eigenenergies. Third, the electrons may further relax by hopping to a lower electronic state, which in return triggers the second step again. At last (at least if the temperature is not taken into account), the excited electrons hop back to their ground state, and the system relaxes.

This relaxed configuration is, however, not necessarily identical with the initial ground state of the system, as the relaxation in excited states may lead the system into a local minimum, or might right out permanently change the system by breaking bonds. For each state in which the system resides for a prolonged amount of time, the relaxation process may lead to several phenomenon, like the formation of polarons, excitons or magnons. This vast amount of interactions makes it difficult to describe the full excitation process; for some systems the validity of the commonly used methods to describe the process is questionable, for many more systems the computational costs are far to high.

Therefore, a compromise has to be made: The more effects one wants to include, the easier to describe the system has to be – the main aspect of this being the amount of atoms in the system. For the first discussed system only the interaction with the light itself is cut from the description, the whole hopping and relaxation process is included. In order to do so, a sufficient small system needs to be chosen: The oxirane molecule.



First reference system: Oxirane

---

### 3. First reference system: Oxirane<sup>2</sup>

#### 3.1. Introductions

As a first reference system on which electron dynamics and their influence on the systems structure are investigated, the oxirane molecule is studied. Oxirane, also known as ethylene oxide ( $C_2OH_4$ ), is an epoxide with a ring consisting of two C and one O atom, and two H atoms each as appendices to the C atoms as shown in figure 1 (leftmost picture). Oxirane sees some industrial applications; it is a raw material for several other chemicals<sup>[76]</sup> and its poisonous properties, for example, are used for sterilization purposes.<sup>[77]</sup> However, the property which is of interest for this work is its reaction to light exposure, the photochemical decomposition. If oxirane is exposed to light with a wavelength lower than 185 nm, it decomposes into its components. This decomposition has already been studied experimentally as well as theoretically, making it a good candidate for the test of the methods introduced in chapter 2.<sup>[78–81]</sup> From a computational point of view this system also bears several advantages: Oxirane is a small molecule, which reduces the computation time, which again enables the consideration of longer molecular dynamics or more excited states. Furthermore, as a single molecule there are no periodic boundaries like in a solid which have to be taken into consideration, which is why there is no dispersion of the bands and only one  $k$ -point has to be calculated – a circumstance which proves important for the surface hopping discussion later in this work.

From the experimental side, the photodecomposition has been studied by identifying the end products of the photoreaction via chromatography. Kawasaki *et al.* analysed the ratios of the end products, and concluded that the reaction path for the decomposition is  $C_2H_4O + \hbar\nu \rightarrow CH_3CHO \rightarrow CH_3 + CHO$ , which confirmed an earlier postulation from Gomer and Noyes.<sup>[79,80]</sup> This reaction is shown in figure 1.

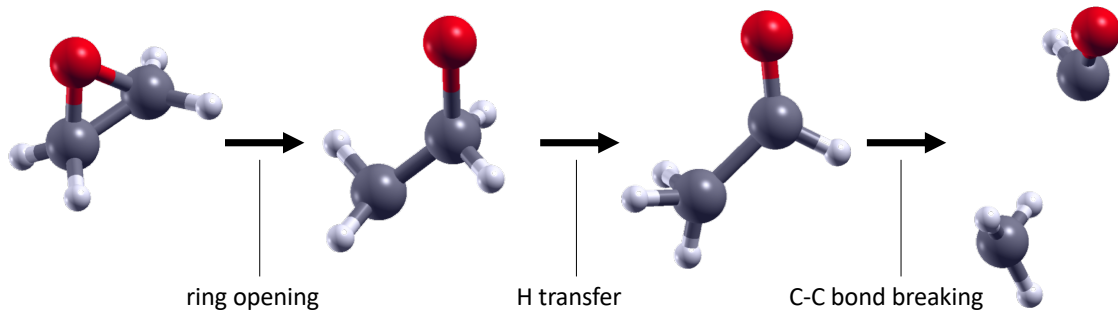


**Figure 1:** The Gomer-Noyes mechanism<sup>[79]</sup> mainly responsible for the photochemical decomposition of oxirane: After an optical excitation the C-O-C ring opens, followed by a proton transfer and ends by a C-C bond breaking.

For the theoretical evaluation of the photoreaction two works are of particular interest. Bin *et al.* calculated the reaction paths with the lowest barriers for the ground state and first excited state using the “state-interaction state-averaged spin-restricted ensemble-referenced Kohn-Sham” method (SSR).<sup>[81]</sup> This method employs a weighted average over different (fractional) occupations and is therefore a multiconfiguration method. That enables a more accurate description of the system, as open shell systems can not be fully described by a

---

<sup>2</sup>The results of the following section were published in Ref. 75

single Slater determinant, thus methods as Hartree-Fock and DFT can only approximate them.<sup>[82]</sup>

Tapavicza *et al.* studied the photodecomposition by the means of time dependent DFT (TD-DFT) molecular dynamics and potential energy surface (PES) hopping using Tully's FSSH and the Landau-Zener method.<sup>[78]</sup> While the later one is roughly explained in chapter 4.9, time dependent DFT is a method which expands on the DFT by the usage of perturbation theory. Using a small, time-dependent perturbation, TD-DFT calculates the linear response function, from which the excitation energies are extracted. For a more detailed explanation of TD-DFT the interested reader may refer to Ref. 83.

Both SSR and TD-DFT are computational expensive methods and can not be used for large systems. c-DFT is not expensive, but does not have a rigorous theoretical foundation. The application of c-DFT to oxirane therefore serves as a kind of “benchmark” for the c-DFT method as realized in the QUANTUM ESPRESSO pw code<sup>[33,34]</sup> (at least for molecules). The following part is structured as follows: First the energies of the ground as well as the first three excited states ( $S_0$  to  $S_3$ ) are calculated and compared with other methods. Afterwards c-DFT is used in conjunction with molecular dynamics and Tully's FSSH algorithm to study the photodecomposition on a non-adiabatic level, identifying the prominent mechanisms, the states responsible for them, as well as the time scale on which the reaction occurs. Hereby the temperature is also taken into account in the *NVE* ensemble as well as in the *NVT* ensemble by using a Nosé-Hoover chain thermostat.

### 3.2. Modelling the static molecule

Since molecules most often exhibit inhomogeneous electron distributions, they are usually described within the generalized gradient approximation<sup>[84]</sup>, which is why the PBE functional is employed. Convergence tests regarding the total (GGA) energy and the KS eigenvalues of the respective excited electronic states in respect to the wave function cutoff and the cell size show, that the Oxirane molecule is described adequately with a cutoff of 70 Ry and a cellsize of  $11 \times 11 \times 11 \text{ \AA}^3$ . This large cell is necessary, as the QUANTUM ESPRESSO pw code is a plane-wave based DFT supercell code that generally applies periodic boundary conditions. This allows the calculation of 3D or 2D periodic structure like solid crystals and surfaces. Non-periodic structures as molecules therefore have to be described in large cells, as a too small cellsize for a molecule results in unwanted effects from the neighbouring images. The convergence of cellsize and cutoff energy is backed up by comparing the electronic densities of the ground states with other DFT-PBE calculations for example in Ref. 78. The calculated ground and excited state electronic densities are shown in figure 2.

The accuracy of the description can also be confirmed by the comparison of the excitation energies. The excitation energy, meaning the energy needed to elevate the system from the ground state  $S_0$  to an excited state  $S_i$ , is the quantity which is usually measured experimentally by the means of optical absorption. Within c-DFT the excitation energy is calculated by the difference between the total energies of the excited system and the system in the ground state,  $E_{\text{exc}} = E_{S_i} - E_{S_0}$ . A comparison with experimental values as well as higher quantum chemical methods is shown in table 1. It can be seen, that while c-DFT slightly underestimates the experimental values, its excitation energies are in good agreement to high effort methods such as hybrid TD-DFT.

Another interesting feature of the electronic densities is their behaviour upon excitation.

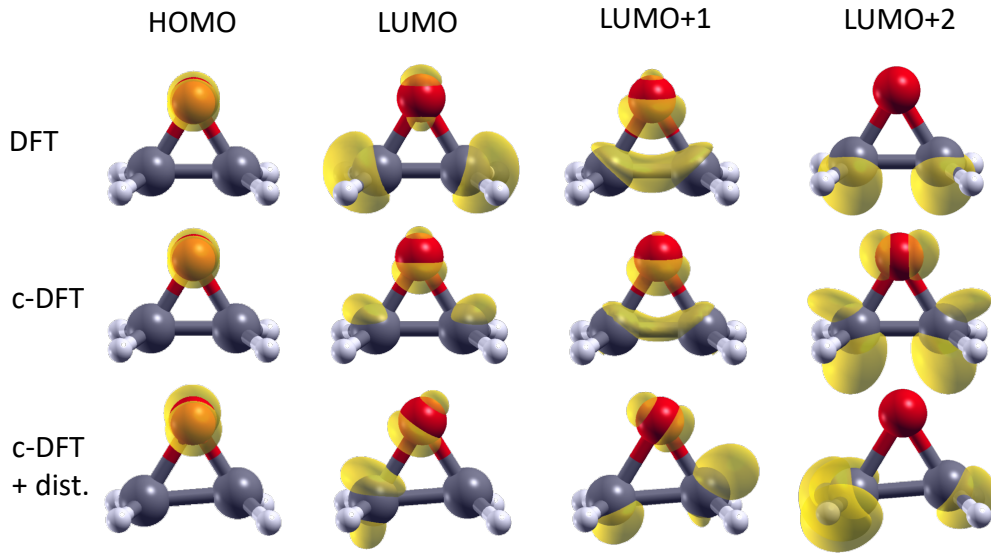


**Figure 2:** Calculated electron densities of the ground state and lowest excited states of oxirane. The top row shows the densities for the highest occupied molecular orbital (HOMO), lowest unoccupied molecular orbital (LUMO), LUMO+1, and LUMO+2 in the structural and electronic ground state. The middle row shows the respective densities calculated using c-DFT to describe the corresponding excited state, i.e.  $S_0$ ,  $S_1$ ,  $S_2$ , and  $S_3$ . The bottom row shows the densities with the same excitation configuration for a slightly disturbed geometry with maximum deviation of 0.05 Å for each atom and direction from the ground state geometry.

This becomes first apparent by comparing the densities calculated by DFT and c-DFT, i.e. the densities associated with the KS wave functions of HOMO, LUMO *etc.* calculated with ground state DFT and calculated directly by the non-Aufbau c-DFT. Besides the ground state  $S_0$ , which is by definition the same in DFT and c-DFT, the second excited state  $S_2$  is little affected by the excitation.  $S_1$  though shows a deviation by mixing some aspects of  $S_2$  into its DFT calculated density.  $S_3$  also partially changes its character, it now resembles the  $S_2$  density of Ref. 81. The densities can be seen in the second row of figure 2. The exact form of the density is, however, also very dependent on the geometry of the system. In the ground state geometry the molecule has a twofold symmetric axis as well as two mirror planes (pointgroup  $C_{2v}$ ). If this symmetry is broken by slightly displacing the atoms, the character of the densities also changes. With broken symmetry the electrons accumulate at one half of the molecule, as shown in the third row of figure 2. This will prove essential for the photoreaction.

c-DFT	exp.	TDHF <sup>[85]</sup>	TDLDA <sup>[85]</sup>	TDB3LYP <sup>[85]</sup>
6.69	7.24 <sup>[86-88]</sup>	9.14	6.01	6.69
6.76	7.45 <sup>[87]</sup>	9.26	6.73	7.14
7.26	7.88 <sup>[86]</sup> , 7.89 <sup>[87]</sup>	9.36	6.78	7.36

**Table 1:** Oxirane singlet excitation energies (in eV) for (PBE) c-DFT in comparison with other computational methods as well with experimental data.

### 3.3. The dynamic system: Methods and parameters

With the stationary molecule covered, it is time to have a look at the dynamic system. For a non-adiabatic dynamic the integral timestep for the nuclei equation of motions as well as for the Schrödinger equation have to be chosen. Additionally, the parameters for the thermostat (if used) have to be chosen as well as the rate of updating of the occupation. The rate of occupation updates is a feature which is related to the smearing method. In regular DFT smearing is a method to tackle the computational issues in metallic systems or systems with a small bandgap. As introduced in chapter 2.2, the energetically lowest  $N_e$  KS-states are occupied with  $N_e$  the number of electrons, the states above do not contribute to the density. Since the eigenenergies of each state change during the self-consistency cycle, this poses a problem if the band gap is small enough (or non-existent as in the case for metals), as unoccupied states then start switching positions with occupied ones. This causes different states to contribute to the density in each iteration, preventing a self-consistent solution. Smearing solves this problem by introducing occupation numbers like in c-DFT, which are, however, not fixed like in c-DFT, but follow a distribution function. The distribution is dependent on the energies of the eigenstates in respect to the Fermi energy of the system. With this the states above and close to the Fermi energy are partially included in the density, with stronger contributions the closer they are to the Fermi energy, which again enables a self-consistent solution. Typical distributions used for this are the Fermi-Dirac distribution,<sup>[89]</sup> the Gauss distribution or the Marzari-Vanderbilt distribution,<sup>[90]</sup> whereby the first one describes a thermal distribution of electrons, and the latter one belongs to the class of “cold smearing”, i.e. distributions which aim at changing the forces of the system as little as possible while improving numerical stability.

In c-DFT the problem mentioned above is even more prominent. Occupied states tend to lower their eigenenergy while unoccupied ones tend to raise their energy. This gives again rise to the state switching problematic, especially if a state inside the conduction band is occupied. Therefore, a smearing is again desirable. However, the implementation of smearing in c-DFT is not straightforward, as there is no well-defined Fermi energy. In order to employ a smearing nonetheless, we expand on an ansatz from Ref. 52. The occupations are calculated by a sum of occupations of the same system (same eigenvalues) with different numbers of electrons. For these, the Fermi energies are defined and a smearing is used for each number of electrons. The total occupation  $n$  is given by:

$$n_{\text{tot}} = \sum_{i=1}^{N_{\text{KS}}} f_i (n(\varepsilon_f(i)) - n(\varepsilon_f(i-1))) \quad (3.53)$$

Here  $f_i$  are the occupation numbers of the c-DFT,  $\varepsilon_f(i)$  the Fermi energy of the system with  $i$  electrons and  $n(\varepsilon_f)$  the occupation numbers for the system with a generic distribution dependent on the Fermi energy  $\varepsilon_f$ . The resulting distribution circumvents the switching problem. Furthermore, there could also be a physical effect due to the smearing, Ref. 52 suggests that the c-DFT smearing could mimic a system described by a multiconfigurational method.

The non-adiabatic dynamics are calculated using a modified version of the c-DFT based surface hopping code LIBRA-X. The modifications to this code are listed in chapter A. For the trajectories a nuclear integration step of 0.25 fs and a Schrödinger equation integration step of 5 as is chosen. The trajectories are propagated for 250 fs. A smearing implemented

as explained above employing the Fermi-Dirac distribution with a broadening of 0.01 Ry is used. The occupation is updated every 30 scf cycles, which leads only to a smearing if the switching problem prevents convergence (usually convergence takes between 7 and 10 cycles). For the thermostat a Nosé-Hoover chain thermostat with a chain length of 5 and an characteristic relaxation time of 24.4 fs is chosen. This corresponds with a frequency of  $1367\text{ cm}^{-1}$  which is between most of the characteristic frequencies of oxirane ( $1000\text{-}3000\text{ cm}^{-1}$ ),<sup>[91]</sup> fulfilling the guideline introduced in chapter 2.4. Since Tullys surface hopping is a statistical procedure, a sufficient large number of trajectories have to be taken into account. Therefore, for each temperature considered 50 trajectories with and without thermostat are calculated. Each trajectory starts from a disturbed groundstate geometry, where each atom is displaced randomly for a maximum of 0.05 Å in each Cartesian coordinate, and in the  $S_2$  excited state. Furthermore, each atom is assigned an initial velocity corresponding to the temperature as explained in chapter 2.4. The temperatures which were taken into account are 30 K, 77 K, 100 K, 150 K, 300 K and 400 K.

As already stated the goal is to identify the excited states which causes or prohibits the photodecomposition, as well as the time scale of it. In order to do so, the reaction products have to be identified and compared to the average occupation numbers. Therefore, geometric criteria have to be found to classify the structures. For the Gomer-Noyes process, the first step lies in the opening of the CCO ring, which is characterizable by the O-C-C angle. This is followed by a proton transfer from one C atom to the other, characterizable by the number of protons on each side of the molecule. At last the CC bond breaks, characterizable by the C-C distance. There are also other products that can occur, like the abstraction of oxygen, the ring opening between the C atoms or an abstraction of a single H atom. These products can also be identified by a combination of geometric criteria as well as their time of occurrence. The parameters are listed in table 2. To identify the different products, following naming conventions are used:  $\text{C}_2\text{H}_4\text{O}$  is the molecule in its geometric ground state, for distorted states the symbols are sorted by on which side of the molecule they are. For example, the structure after the ring opening is referred to as  $\text{CH}_2\text{COH}_2$ , after the H transfer as  $\text{CH}_3\text{COH}$ . If the molecule dissociates a “+“ is used, after the C-C bond breaking it is referred to as  $\text{CH}_3 + \text{COH}$ .

reaction prod.	max. O-C-C angle	max. # H ions at C	C-C dist.	min. C-H dist.	min. C-O dist.
$\text{C}_2\text{H}_4\text{O}$	< 100°	2	-	< 1.8 Å	< 2.0 Å
$\text{CH}_2\text{COH}_2$	> 100°	2	< 2.6 Å	< 1.8 Å	< 2.0 Å
$\text{CH}_2 + \text{COH}_2$	-	2	> 2.6 Å	< 1.8 Å	< 2.0 Å
$\text{CH}_3\text{COH}$	-	3	< 2.6 Å	< 1.8 Å	< 2.0 Å
$\text{CH}_3 + \text{COH}$	-	3	> 2.6 Å	< 1.8 Å	< 2.0 Å
$\text{O} + \text{C}_2\text{H}_4$	-	-	-	-	> 2.0 Å
$(2)\text{H} + \text{H}_2\text{C}_2\text{O}(\text{H})$	-	-	< 2.6 Å	> 1.8 Å	< 2.0 Å
$\text{CH}_3 + \text{CO} + \text{H}$	-	3	> 2.6 Å	> 1.8 Å	< 2.0 Å
$\text{CH}_2 + \text{H} + \text{COH}$	-	3	> 2.6 Å	> 1.8 Å	< 2.0 Å

**Table 2:** Geometrical parameters used to determine the reaction products.

The average occupation numbers seem straightforward to compute. However, a word of caution is in order. Since the smearing is first applied after 30 scf cycles, each excited state is calculated with a (possibly) different smearing. This might lead to a change in their energetic ordering, as one state might experience smearing while the other does not. Due to the diagonalization in equation 2.40 this leads to a swap of the states. If one of these states is the active state, a hop between those states is probable, as the character of the states is retained during the swap. This means a hop between states is registered, while in reality only one state is temporarily energetically lower than the other one. To account for this, the occupation numbers are compared with the energetic ordering of the PES of the c-DFT calculations and swapped back before averaging if necessary. To circumvent this problem from the beginning one could opt for a shorter update interval for the smearing; however, this could lead to deviation of the forces if the smearing affects states which should not interact with each other. This could be mitigated by using a cold smearing distribution like the Mazari-Vanderbilt distribution; however, at this point in time other smearing methods besides Fermi-Dirac were not implemented (see also section A).

### 3.4. Results: Statistics of the *NVE* and *NVT* ensemble

We begin the analysis by comparing the average occupation numbers for the trajectories calculated within the *NVE* ensemble. For the temperatures of 100 K and 300 K these are shown in figure 3. It can be seen that within 80 fs for the majority of the trajectories the

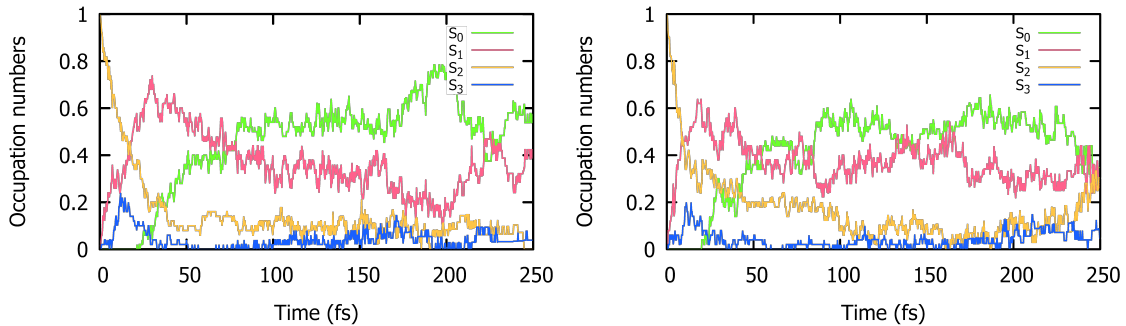


**Figure 3:** State populations for *NVE* calculations modelling an initial temperature of 100 K (lhs) and 300 K (rhs). Occupation numbers are averaged over 50 trajectories.

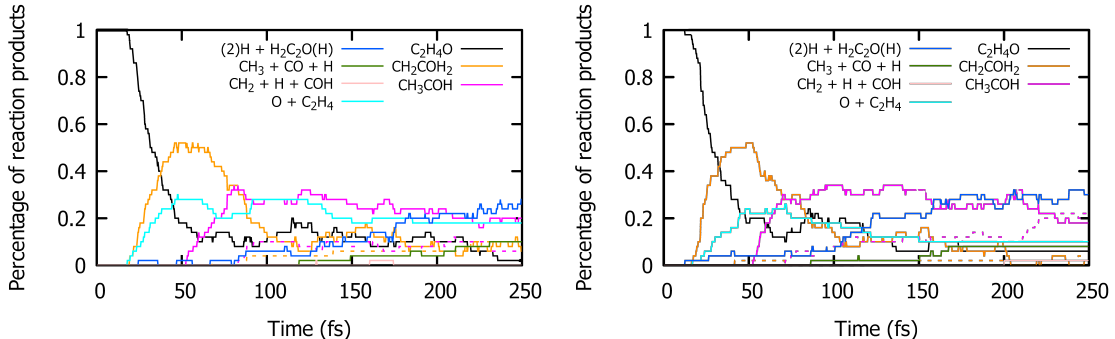


**Figure 4:** Reaction products over time in the microcanonical *NVE* ensemble for temperatures of 100 K (lhs) and 300 K (rhs). Dashed lines correspond to dissociated variants of  $\text{CH}_2\text{COH}_2$  and  $\text{CH}_3\text{COH}$  respectively. The peaks show very similar shapes and positions, indicating little influence of the temperature on the reaction times.

excitation is transferred from  $S_2$  over  $S_1$  to  $S_0$ , though a considerable amount stays in  $S_1$ . The corresponding percentage of reaction products is shown in figure 4. Here the Gomer-Noyes mechanism can be identified as the most prominent one, as indicated by the rise of the percentage of the  $\text{CH}_2\text{COH}_2$  product (the ring opening) within the first 40 fs, followed by a rise of the  $\text{CH}_3\text{COH}$  product (H transfer) within the first 80 fs. The last step in the mechanism, the C-C bond breaking, however, is not present in as large quantities as in the experiment, though a similar low bond breaking rate is found in the theoretical work of Tapavicza *et al.*<sup>[78]</sup> The calculated times for the reaction steps also coincide. Next to the Gomer-Noyes mechanism there are two other processes which give rise to other products, the oxygen and hydrogen abstraction. Those usually occur from the  $\text{C}_2\text{H}_4\text{O}$  geometry. While the O abstraction reaction is generally reversible, the H abstraction tends to be permanent. For all these reactions, the temperature has little influence on the excitation dynamics, the occupation numbers and the reaction times are mostly the same. However, there is an influence of the temperature on the O and H abstraction reaction, or more specifically their quantities. With higher temperatures there are less O abstractions and more H abstractions (see also figure 4). For the O abstractions the symmetry breaking is the reason for this. As will be shown below, for the O abstraction to occur, the C-O-C ring has to be as close as possible to a mirror symmetry regarding the O ion. With higher temperature this required symmetry is broken quickly, leaving the reaction no time to happen. The H abstraction is only driven thermally and therefore straightforward, with higher temperature there is more kinetic energy available for the reaction to occur. Similarly more C-C bond breakings are observed at higher temperature.

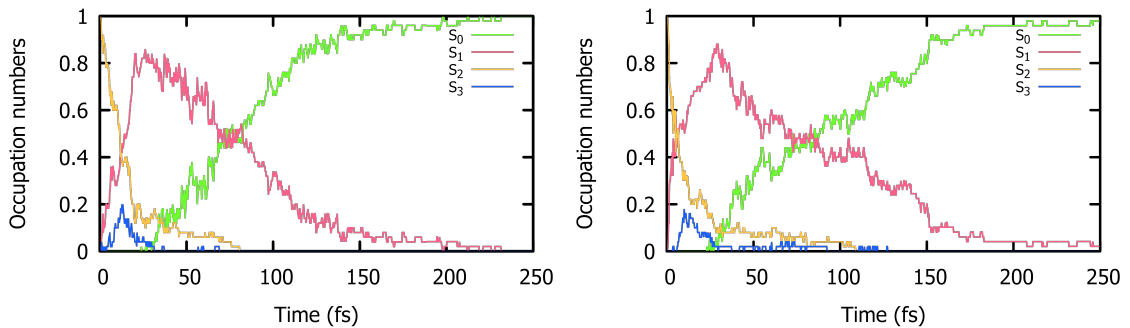


**Figure 5:** State populations for *NVT* calculations modelling an initial temperature of 100 K (lhs) and 300 K (rhs). Occupation numbers are averaged over 50 trajectories.

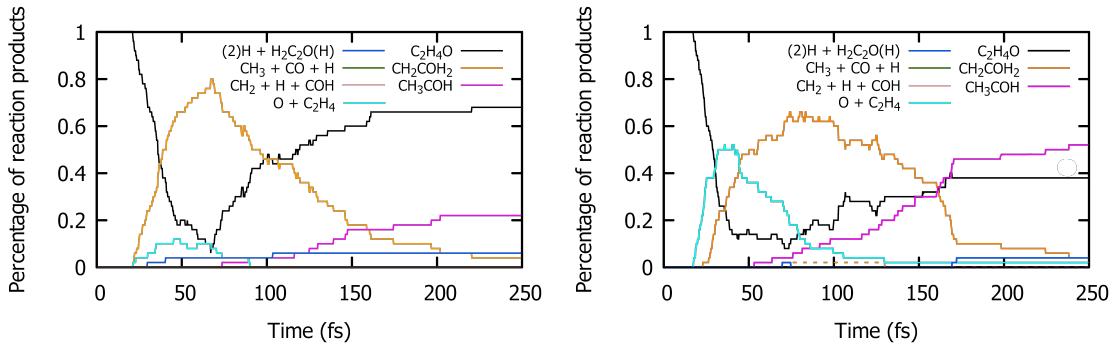


**Figure 6:** Reaction products over time calculated in the canonical *NVT* ensemble at temperatures of 100 K (lhs) and 300 K (rhs). Dashed lines correspond to dissociated variants of  $\text{CH}_2\text{COH}_2$  and  $\text{CH}_3\text{COH}$  respectively.

This changes as soon the trajectories in the *NVT* ensemble are considered. Again, we begin with the occupation numbers, which are shown for the temperatures of 100 and 300 K in figure 5. A more rapid quenching of the  $S_2$  state to the  $S_1$  state can be observed, while the  $S_3$  state is almost completely suppressed. Furthermore, nearly all trajectories end in  $S_0$  state at the end of the simulation, in contrast to the *NVE* ensemble. This different behaviour is also reflected in the reaction products shown in figure 6. Most prominent is the absence or quenching of reaction products which require a dissociation of the ions. For those reactions to occur the respective ions have to have a comparatively high amount of initial kinetic energy, or have to be propelled by the excited state and thus gain more kinetic energy. In both cases this additional energy is dissipated due to the thermostat, which hinders or reverses the bond breaking. The remaining reactions are now also heavily dependent on the temperature. With higher temperatures the trajectories remain longer within the  $\text{CH}_2\text{COH}_2$  state, and more trajectories perform the H transfer. As will be shown below, the H transfer is driven only thermally, therefore a decrease of this reaction with lower temperature is obvious. This results in most trajectories ending in the  $\text{C}_2\text{H}_4\text{O}$  geometry at low temperature while for high temperatures the majority ends within the  $\text{CH}_3\text{COH}$  geometry as shown in figure 7 rhs.

These end products are also listed in terms of their yields and compared to experimental values in table 3. Since no C-C bond breakings are observed in the *NVT* ensembles, reactions with and without bond breaking will not be differentiated. For the O abstraction the *NVE* ensemble shows a closer agreement to the experimental values than the *NVT* ensemble, which generally shows less abstractions. In case of the H abstraction the *NVT* ensemble also shows less abstractions than the *NVE* ensemble, though this time the *NVT* ensemble is closer to the experiment. This difference might lie in the origin of the reactions. In both cases the thermostat overestimates the energy dissipation. As already stated, the H abstraction reaction needs a great amount of excess kinetic energy – a rarity within a thermal equilibrium. However, the calculations do not start from a thermal equilibrium, but rather from a random velocity distribution, in which this may occur more often. This error is compensated by the thermostat, making the *NVT* ensemble more accurate. In case of the O abstraction the reaction is driven by the  $S_1$  state (as will be shown below), provided a symmetry of the C-O-C ring is given. Therefore, it is not driven thermally. The movement of the O ion, however, is slowed by the thermostat, which has now no error to compensate, it rather overcompensates. Furthermore, the O abstraction almost always occurs at the beginning of the trajectory and within a short time frame, where the energy

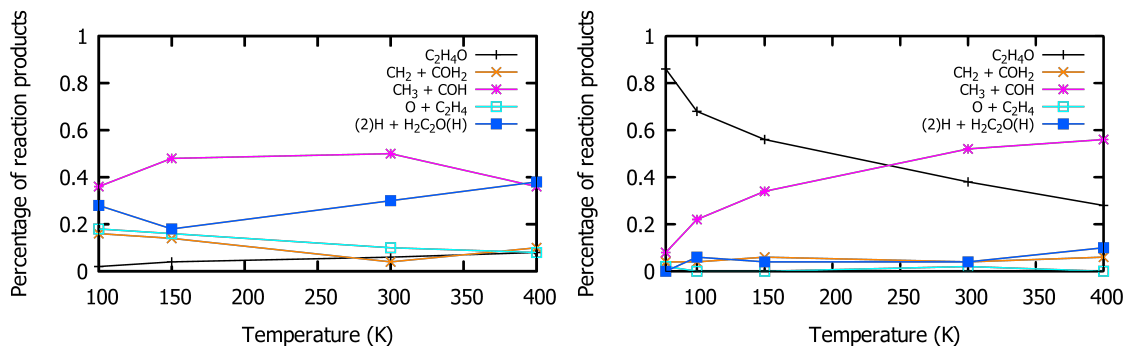


**Figure 7:** Percentage of end products over temperature after 250 fs integration time calculated in the microcanonical *NVE* (lhs) and canonical *NVT* ensembles (rhs). For the sake of clarity of presentation, products with and without C-C bond breaking are not discriminated.

temperature/K	NVE				NVT					Exp. 77
	100	150	300	400	77	100	150	300	400	
CH <sub>3</sub> +COH	1	1	1	1	1	1	1	1	1	1
CH <sub>2</sub> +COH <sub>2</sub>	0.42	0.29	0.08	0.28	0.50	0.18	0.17	0.08	0.11	0.00 - 0.17
O+C <sub>2</sub> H <sub>4</sub>	0.50	0.33	0.20	0.22	0.25	0.00	0.00	0.04	0.00	0.10 - 0.58
(2)H+H <sub>2</sub> C <sub>2</sub> (H)	0.78	0.38	0.60	1.06	0.00	0.27	0.12	0.08	0.18	0.08

**Table 3:** Calculated reaction yields after 250 fs simulation time compared to experimental data after optical excitation with 174 - 147 nm light<sup>[80]</sup>. All yields are normalized to the CH<sub>3</sub>+COH formation. Reactions with and without C-C bond breaking are not discriminated.

dissipation is likely to have little influence on the trajectory. The occurrence of CH<sub>2</sub>+COH<sub>2</sub> product though is overestimated by both ensembles, at least for low temperatures. For high temperatures the *NVT* ensemble has a good resemblance.

### 3.5. Results: States during the Reaction

At last the states responsible for the reactions are identified. In order to do so the occupation numbers are compared to the reaction products (cf figures 3, 4 and 5, 6). It is evident that the shape of the peaks of the S<sub>1</sub> state and the CH<sub>2</sub>COH<sub>2</sub> product as well as the S<sub>0</sub> state and the CH<sub>3</sub>COH product are similar; the ring opening therefore occurs in the S<sub>1</sub> state and the H transfer in the S<sub>0</sub> state. For the ring opening this can be underlined by means of the electronic densities during the reaction. The densities shown in figure 8 indicate the repulsion of the O ion. This finding is in line with Kasha's rule, though it contradicts the findings in Ref. 78, where the S<sub>2</sub> state was identified. That deviation is most likely due to the sensitivity of the excited states to changes of the occupation numbers as well to structural distortions (see figure 2). The transfer of the H ion in the S<sub>0</sub> state, however, is again in accordance to Ref. 81. This transfer is driven thermally, wherefore it can not be observed by the means of electronic densities. However, it can be shown that the reaction would not occur, if the molecule is still in the S<sub>1</sub> state, as it is repelled by the density located at the C ion (see figure 9).

Further evaluation of the structure shows that the majority of the H transfers occur if the H ions opposite to the O ion are rotated 90° around the C-C bond axis (see middle geometry of figure 9 for example), which is in agreement with the findings in Ref. 81. This is more prominent in trajectories without thermostat, in *NVE* trajectories the transfer can also occur at a smaller angle. This is again due to the lack of energy dissipation in the *NVE* ensemble, allowing a less optimal reaction path. The H abstraction reaction is driven thermally, it can occur in every state. The O abstraction, however, can be driven by the S<sub>1</sub> state as well as by the S<sub>2</sub> state. In the geometric ground structure both states are symmetric in shape with electron densities located at the C and O ions, see figure 2. This leads to a overall repulsion directed away from both C atoms. Since these two states contribute the majority of active states at the beginning of the trajectories, as well as the distortion of the molecule being most likely the smallest at the beginning, the reaction mainly also occurs at the beginning. An example of this reaction is shown in figure 10.

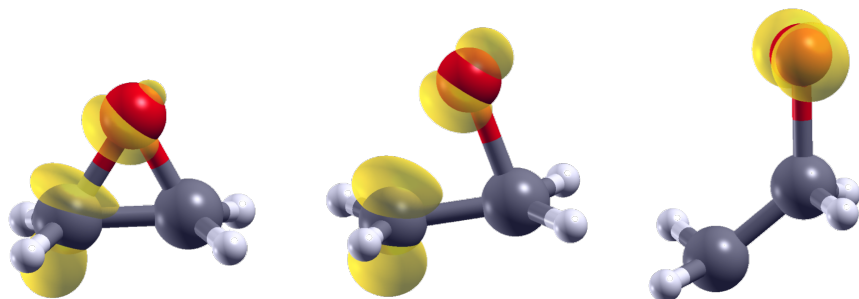


**Figure 8:** Electronic densities of the active  $S_1$  during the ring opening reaction for an example trajectory after 5, 15 and 30 fs. A slight asymmetry causes the O ion to be repelled from one C ion.

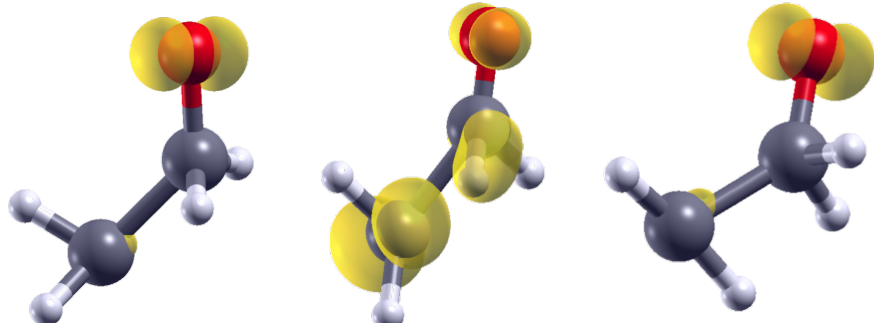


**Figure 9:** Electronic densities of the active state for an example trajectory of an inhibited H transfer. The transfer begins at the left image (after 135 fs) in the  $S_0$  state by moving one H atom from one C atom towards the other, and rotating the opposite H-atoms. Midway in the reaction the system switches to the  $S_1$  state, which causes a repulsion of the H atom (mid figure at 145 fs). This repulsion causes the molecule to revert to its previous structure, as shown in the right figure (at 155 fs again in the  $S_0$  state).

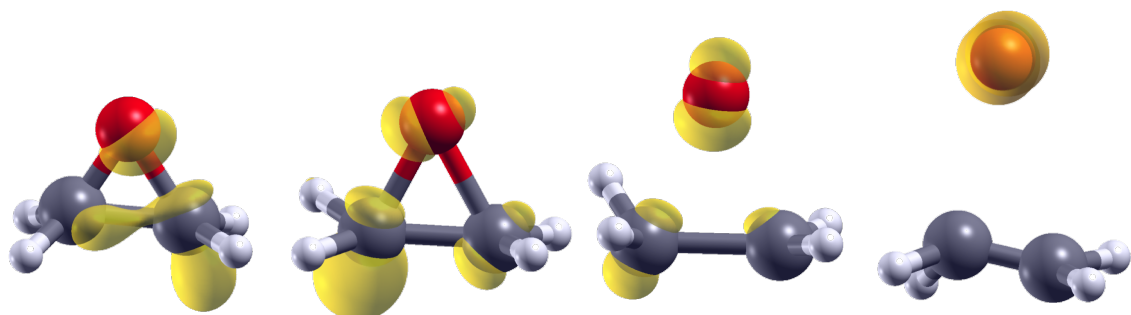
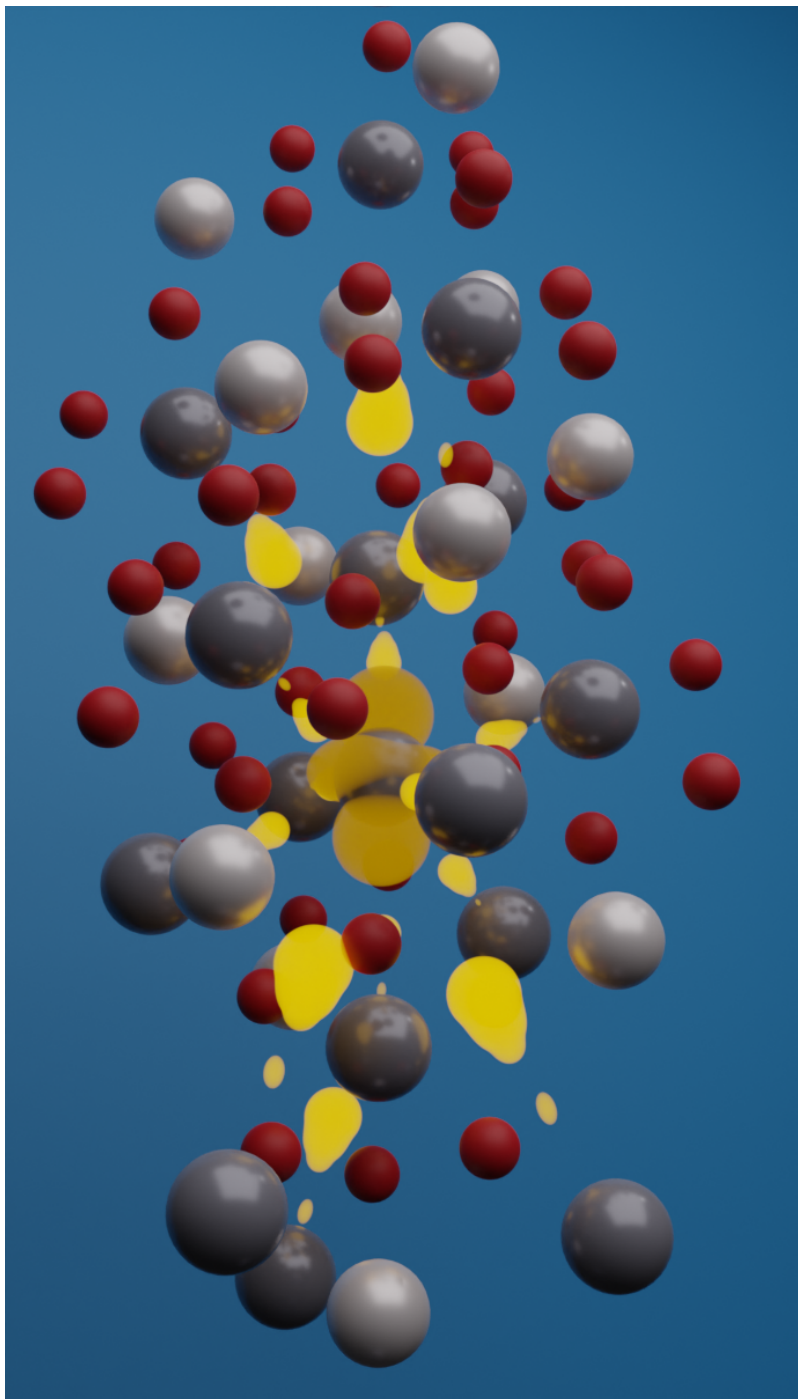


**Figure 10:** Electronic densities of the active state during an O abstraction reaction of an example trajectory. The first two frames (0 and 10 fs) are governed by the  $S_2$  state which symmetrizes the slightly asymmetric starting structure. With the C and O atoms being virtually symmetric, both the  $S_1$  and  $S_2$  state repulse the O atom (see also figure 14), in this case the  $S_1$  state is responsible for separating the O atom from the molecule (third and fourth frame, at 20 and 35 fs).

In summary, using c-DFT molecular dynamics and FSSH electron hopping, the Gomer-Noyes mechanism could confirmed to be the prominent photoreaction in oxirane. The whole reaction usually occurs within the first 90 fs of the trajectories. The ring opening is driven by the  $S_1$  state, in accordance to Kasha's rule, while the rest of the reaction occurs in the  $S_0$  ground state. Beside the Gomer-Noyes mechanism the abstraction of H and O atoms was observed, where the first one is driven thermally and can occur in every state, while the later one is driven by the  $S_1$  or  $S_2$  state. The computed reaction yields largely agree with experimental data; however, the  $NVE$  ensembles overestimate the H abstractions due to the start from a thermal non-equilibrium configuration as well as the neglect of energy dissipation, while the  $NVT$  ensemble underestimates the amount of O abstractions due to an unrealistic fast dissipation within the beginning of the trajectories. This shows that the modelling of the energy dissipation via a thermostat is important and non trivial even in the sub picosecond range. Furthermore, these calculations show, that c-DFT is a viable approach for modelling excited states, even compared with high end, computational expensive methods. With this knowledge we now turn towards a larger system with more dimensions and interactions: The polaron formation in the lithium niobate crystal.



Polaron formation in lithium niobate

---

## 4. Polaron formation in lithium niobate<sup>3</sup>

### 4.1. Introduction: Lithium niobate and polarons

Lithium niobate (LN) is a crystal with a magnitude of optical applications. It can be used as a waveguide, for frequency doubling in lasers, optical switches and other non linear optical applications.<sup>[93–96]</sup> LN has the structural formula  $\text{LiNbO}_3$  with a standard unit cell containing 10 atoms. It consists of two sublattices, the negatively charged O ions, which form a closely packed octahedral lattice, and the positively charged Nb and Li ions, which resides in the octahedra as shown in figure 11. This structure, however, is not completely rigid, the sublattices can shift relatively to each other for example, which results in the material being easily polarizable.<sup>[97]</sup> The comparatively small size makes it possible to study effects and properties which occur on a larger scale like crystal defects or phonons by applying a super cell approach. Together with the rich amount of effects in this crystal it makes for an ideal testing ground for the further application of electron dynamic simulations. We in particular study the polaron formation in lithium niobate. But before we can go into more detail on how electron dynamics can be used to study polarons, we first have to clarify what polarons are.

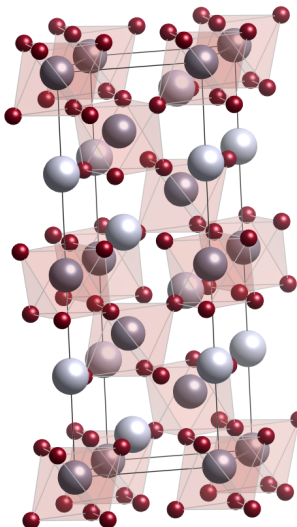


**Figure 11:** Lithium niobate shown in its hexagonal unit cell. Nb atoms are indicated by a dark grey color, Li by a light grey, O atoms are red. The O octahedra are shown as guide to the eye.

Polarons are quasi particles which consists of a charge carrier, meaning an electron or hole, and a lattice distortion. In order to understand the concept of the polaron one can first consider an electron which is travelling through a crystal, or alternatively an excess electron which is localized at some place in the crystal. This electron introduces Coulomb forces to the ions in its vicinity. These ions are repulsed (or attracted) to the electron which causes the mentioned lattice distortion and therefore polarizes the crystal in the vicinity of the electron. This causes the bare Coulomb potential of the electron to be screened, which therefore does not interact with electrons or ions which are farther away. As the electron moves through the crystal other ions are displaced, or, from another point

---

<sup>3</sup>The results of the following section were published in Ref. 92. Several figures of this article have been reused, in accordance with the Creative Commons licence 4.0 <https://creativecommons.org/licenses/by/4.0/legalcode>

of view, the electron is followed by a “cloud” of distortions. Often this distortion field is associated with phonons, and as the distortion field follows the electron, the polaron can be described as a quasi particle made of a charge carrier and a phonon.<sup>[98,99]</sup> Strictly following this definition polarons can not occur, or only exist weakly bound, in materials where the electron-phonon interaction is only weak.<sup>[100]</sup> In the case of ferromagnetic materials, LN in particular, polarons are often viewed in a broader way, the distortion is not restricted to phonons and polarons can therefore also exist in a static system.<sup>[99]</sup>

## 4.2. Polaron in lithium niobate: Types and classifications

In summary, the polaron consists of a charge carrier (an electron or a hole for example) which is localized strong enough to cause a lattice distortion, and the localization itself. Depending on how these effects occur and how strongly they are pronounced, the polarons are categorized into several categories. Firstly they are distinguished by the “size” of their localization. A weakly localized carrier occupies a large amount of space (several lattice sites), which causes many ions to be displaced, though the displacement is rather small. These polarons form if long distance interactions are prevalent in the solid. If the carrier is strongly localized it occupies a small amount of space (i.e. a single lattice site or its close vicinity), and causes less ions to be displaced, but the displacement is more significant. These polarons form if the short distance interactions are prevalent. Accordingly to the size of the localization these polarons are referred to as large and small polarons.<sup>[100,101]</sup> Secondly the polarons are divided on how the carrier localizes. One possibility is that the carrier localizes spontaneously, for example due to a small already existing lattice distortion. The following lattice distortion stabilizes the carrier, which then cannot travel freely through the crystal anymore, it is trapped at its current position. Since the localization of the carrier itself causes this trapping, this kind of polaron is referred to as self trapped electron (or self trapped hole) or as free polaron (as no external force binds the polaron to its place).<sup>[99]</sup> In contrast the polaron can also form at a lattice defect which causes the carrier to localize. The carrier is then bound to the defect and additionally trapped by the lattice distortion. Since the carrier is bound to the defect one can refer to it as charged defect or as bound polaron.<sup>[102]</sup> Lastly the polarons are characterized by the type of charge carrier. If the charge carrier is not an electron, but rather the absence of it (a hole), the polaron is called a hole polaron. If two excess electrons are present in the system, they can both form polarons, which then again couple together. These polarons are called bipolarons and consist usually of a bound and a free polaron. At last if the charge carrier is a single electron no further specification is made.

In lithium niobate several types of polarons have been confirmed by means of magnetic resonance studies, optical absorption experiments and DFT.<sup>[99,103,104]</sup> There is the small free polaron, which locates at a regular Nb site. The small bound polaron, which localizes at a defect, forms at a Nb<sub>Li</sub> antisite.<sup>[103–105]</sup> The hole polaron is reported to form at O sites, and the bipolaron consists of a small bound polaron at a Nb<sub>Li</sub> site and a small free polaron at an adjacent Nb<sub>Nb</sub> site.<sup>[103–105]</sup> For the small free polaron and the small bound polaron the structure and DFT parameters were already modelled in Ref. 104. With these models as a basis we try to answer the questions of the time frame which the polarons need to form, the different formation steps of the polarons and their time scales as well of the mechanisms which causes the electron to localize. As core of the simulations we again use an ensemble of molecular dynamics. As a first step it is necessary to be able to identify if a polaron occurs during a MD.

### 4.3. Detection of polarons

For this we first have a look at how polarons are observed experimentally. Most commonly polarons in LN are observed by the means of pump-probe absorption experiments. In these experiments the crystal is exposed to laser radiation for short femtosecond time intervals repeatedly for several nanoseconds. After a set delay a weaker probe pulse is sent through the crystal. This light is then detected again (either in reflection or in transmission direction) and analysed by the intensity. By comparing the input and output intensity the changes in absorption due to the pump pulse can be observed.<sup>[106]</sup> This change in absorption is usually explained using the following scheme: Upon the pump pulse electrons are excited into the conduction band of the crystal. They then relax to the lowest conduction band. Following this the wave function of the electrons spontaneously collapses, the electrons localize at a lattice site. The surrounding lattice screens the electron and thereby lowers its energy into a mid gap state.<sup>[107]</sup> From this mid gap state multiple excitations are possible. On one hand, the electron can be excited to the conduction band, resulting into a delocalization of the electron. On the other hand, if there is a suitable acceptor site, the electron can be excited to another polaronic state, which could for example be an already distorted Nb site or an antisite. This process is a sub process of the so-called polaron hopping (the other sub process being polaron movement through thermally activated phonons), which transports the polaron through the crystal and thus contributes to the electric conductivity.<sup>[99,108]</sup> Both the excitation to the conduction band and the (non-adiabatic) polaron hopping show a spectral signature and are thus measurable in the absorption experiments.

It is therefore clear that the position of the lowest conduction band, i.e. the would-be polaronic state, is linked directly to the absorption and thus the experimental defining criterion of a polaron. In contrast to the experiment though we are not confined to observing the polarons only after they have formed. Using the electronic density of the DFT the localization of the electron can also be observed and differentiated from the screening process due to lattice relaxation. However, it is both tedious and storage intensive to compare the MDs by their electron densities for a large amount of trajectories, furthermore the storage of these densities is not implemented in the used code. Luckily there are other criteria which can also identify the localization of an electron. First one can utilize the fact that the polaron which forms in LN is a small one and therefore strongly localized. A strong localization in real space is accompanied by a state with little dispersion in reciprocal space. This means that a straightening of the lowest conduction band indicates the localization of the electron. Another method for identifying the localization is the local magnetic moment. When the electron localizes it carries a magnetic spin moment. A drastic increase of the magnetic moment therefore indicates the formation. Last but not least the surrounding lattice can be observed. Once the electron localizes, the relaxation process of the surrounding lattice begins. In case of LN this means that the surrounding negatively charged O ions are repelled by the charge. The average distance of those ions can be used as indicator for when the relaxation occurs. It is therefore suited to describe the end of the whole polaron formation and can also roughly show the end of the electron localization. With the parameters defining the polaron formation process discussed, we now have a look on the conceptually most simple polaron, the free small polaron.

### 4.4. Modelling the free polaron

The free small polaron is one the most occurring polarons in LN, as it can localize at any non defect Nb because it requires only the self trapping. It is relative loosely bound

to its site with an excitation energy of around 1 eV.<sup>[104]</sup> In order for a polaron to form an “additional” electron which is not necessary for the bonds of the crystal is needed. Experimentally such a free electron is created by the excitation of the crystal due to a laser. Instead of modelling this excitation with c-DFT like in the case of oxirane, this time it is modelled by a charged system instead. As stated in chapter 2.6 this is technically no excitation, but a different system entirely, and therefore is usually more limited in its significance. However, in this case the model is sufficient. First, the hole left in the valence band can form a hole polaron. With a hole polaron formed its influence on the crystal is only local, and since we are only interested in the free polaron we can discard it. Furthermore, the free electron does not necessarily need to stem from the same spacial region of the crystal, limiting the influence of a hole even more. Last but not least LN can contain deep trap states (either through impurities or targeted doping) like in the case of iron impurities.<sup>[109,110]</sup> An excitation from these deep trap states will also leave the crystal largely unaltered. Therefore, the more simple modelling with a charged system and groundstate DFT is reasonable.

For the further construction of the model it has to be considered, that the polaron is on one hand, a local occurance and on the other hand, is generated only in comparatively low quantities; there are considerably more Nb ions which house no polaron than ones which do. Therefore, it is not possible to construct the polaron in the standard LN unit cell, a supercell approach has to be utilized. Explicitly a  $2 \times 2 \times 2$  supercell containing 80 atoms is used. A straightforward approach to construct the free polaron now would be to recreate the conditions in the experiment: Add an electron to the system (the excitation), distort the geometry of the ideal LN (the thermal displacement of the atoms) and relax the system. Afterwards the polaron should have formed at a random Nb site. However, while the arbitrariness of the site leads to many easily detectable free polarons in absorption experiments, it poses a problem for the modelling in DFT. First, the detection of the polaron can be problematic, as all the mentioned criteria have to be checked for each possible atom site. While this can be overcome, one of the inert problems of DFT, the self interaction error, interferes. As stated in chapter 2.8.1, the self-interaction error hinders the electron to localize in small areas. In this case that means that in the ground state structure, in which the Nb atoms are all equivalent, the electrons are delocalized over the Nb sites. The atomic displacements caused by the temperature designates some Nb atoms; however, the perturbation is not strong enough to overcome the self interaction error and will still result in an electron delocalized over all Nb sites. The electron therefore needs a stronger “motivation” to collapse on a Nb site.

This extra motivation comes in form of the DFT+U method. As explained in more detail in chapter 2.8.2, the DFT+U method introduces an energy term dependent on the occupation of certain localized states (usually *d* or *f* electrons). This term increases the energy of partially occupied states and therefore encourages the states to be either completely occupied or empty. For the construction of the polaron the U term is only applied to a single Nb ion. The surrounding ions are displaced according to their charge, the negatively charged O ions are moved away from the Nb ions, the Li ions are moved closer. This configuration makes the localization of the electron energetically favourable. After that the system is relaxed, resulting in the formation of the polaron. Afterwards the other Nb ions are also treated with the +U method, the values are determined self-consistently to compensate for the derivative discontinuity error. These steps lead to the model from Ref. 104, the free polaron modelled within a  $2 \times 2 \times 2$  LN supercell charged with one electron, a kinetic energy cutoff of 85 Ry, normconserving PBEsol pseudopotentials, a  $2 \times 2 \times 2$  Monkhorst-Pack grid

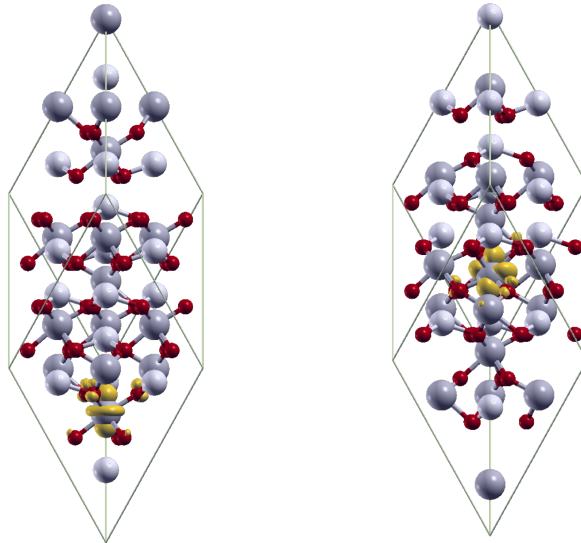


**Figure 12:** Structure and electronic density of the free (lhs) and bound (rhs) polaron.

and U corrections of 4.9 eV for the polaron site Nb and 4.7 eV for each other Nb ion. The resulting electronic density is shown in figure 12.

This model is now employed to study the formation of the polaron. The idea is rather straightforward: Starting from a thermal equilibrium an electron is added to the uncharged system. Afterwards a molecular dynamic is performed and the criteria for the polaron formation checked. Since MDs are comparatively computational expensive it is useful to verify beforehand if polarons can form under such conditions. In order to do so a molecular dynamic of the ideal system using a Berendsen thermostat at low temperature (50 K) was conducted to generate distorted geometries. Afterwards the system is charged and relaxed. With no ion velocity present, in order for the polaron to form, the system has only to overcome the small deviations due to the temperature. However, for each of the three tested starting geometries no polaron formation could be observed, the electron delocalizes instead. This indicates that with this model also no polaron will form in a MD, where the ion movement can additionally obstruct the formation. In order to increase the possibility of polaron formation, the Hubbard U term was removed from all but one designated Nb ion, in other words going one step back in the construction procedure of the free polaron model. With this new parameter the tests were repeated. Unfortunately, even with only one Nb designated no polaron formation could be observed.

It appears that the geometries leading to the formation of a free polaron only occupy a small area in configuration space. With only a single ion designated it is very improbable to achieve a fitting configuration. In the experiment this “problem” is overcome due to the large amount of possibilities. As a reference, in the absorption experiments from<sup>[111]</sup> a magnitude of  $10^{12}$  electrons are excited, leading to an excitation density of roughly  $1.2 \cdot 10^{18} \text{ cm}^{-3}$ . Considering the unit cell of LN a density of  $1.8 \cdot 10^{22} \text{ cm}^{-3}$  Nb ions is to be expected. This gives the electron  $1.5 \cdot 10^4$  possibilities to localize onto which ensures the formation of polarons despite it occupying only a small area in configuration space. In the simulation we can either specify a single Nb ion where the polaron should form, this, however, reduces the number of configurations drastically, or treat all ions the same, which increases the number of configurations but is not feasible, since the electron tends to delocalize in this case. Due to this the formation dynamics of the free polaron could

not be studied, we focus on the bound polaron instead.

#### 4.5. Modelling the bound polaron

For a bound polaron to form an external potential well is required. In the case of LN this potential comes in the form of a defect, i.e. a Nb ion occupying a Li site. This defect is designated as  $\text{Nb}_{\text{Li}}$ , or more specifically according to its charge state  $\text{Nb}_{\text{Li}}^{5+}$  in its regular state or  $\text{Nb}_{\text{Li}}^{4+}$  if a polaron occupies the defect site.<sup>[99]</sup> Typically modelling a defect is more challenging than an ideal crystal, especially because a larger unit cell is needed to incorporate the defect. For the free polaron a  $2 \times 2 \times 2$  supercell was already established. By replacing one Li ion by a Nb ion a Li/Nb ratio of 0.88 is simulated. For reference, the Li/Nb ratio of ideal, stoichiometric LN would be 1, which can not be manufactured. The near stoichiometric probe used in Ref. 111 for example is around 0.984. The commonly used Czochralski method<sup>[112]</sup> to grow LN congruently yields a ratio around 0.94.<sup>[113]</sup> The model therefore approximates the congruent quota acceptably, therefore the same cell as for the free polaron can be used. The bound polaron can be expected to form more reliably than the free polaron in a MD: On one hand, the defects produces a potential well independent of the electron, which encourages the collapse of the electron onto the site and further stabilizes it. On the other hand, the density of Nb defects is far lower than the one of regular Nb sites. Using the LN unit cell as a basis, congruent LN has a NB antisite density of  $5.84 \cdot 10^{20} \text{ cm}^{-3}$  and stoichiometric LN has a density of  $1.46 \cdot 10^{20} \text{ cm}^{-3}$ . This reduces the possibilities for a single electron to 486 and 121 sites respectively. Depending on the growth method and defect model the density can even be lower.<sup>[114]</sup> Despite this considerably lower count, the bound polaron is observed experimentally both in optical experiments<sup>[103]</sup> and magnetic resonance.<sup>[99,104]</sup> This in turn indicates, that the area in configuration space which leads to bound polaron formation has to be larger than for the free polaron, which is again beneficial for the description in a MD. This area in configuration space was in fact calculated in form of a “trapping radius”, i.e. the radius in which the excited electron collapses directly onto the antisite, a quantity which will be referred to later.<sup>[115]</sup>

The construction of the bound polaron is analogous to the free polaron, with the addition of one Li ion being replaced by a Nb ion. Since Nb contains more valence electrons than Li, the surplus of electrons needs to be removed, charging the cell positively. Afterwards one excess electron is added again. An additional Hubbard U correction term is added to the antisite Nb, the ions surrounding it distorted and the system relaxed. Adding the self-consistently calculated U terms for the other Nb ions and keeping the computational parameters of the free polaron leads to the bound polaron model of Ref. 104. The resulting electronic density is shown in figure 12.

With this system the same tests like in the case of the free polaron are conducted. Using a MD with the uncharged system utilizing the Berendsen thermostat at 50 K starting configurations are produced, which are afterwards relaxed including the excess electron. In contrast to the free polaron there are two outcomes: For some relaxations a polaron forms. The majority, however, runs into numerical instabilities. These instabilities usually occur when the localized Hubbard orbitals are partially filled. As explained in chapter 2.8.2, partially filled orbitals lead to higher energies. Depending on the algorithm of the eigenvalue solver for the KS equations this can introduce non-positive definite matrices, which prevents an iterative solution of the equations. Since for the polaron formation the regime of partially filled orbitals needs to be crossed, the majority of trajectories shows

this problem. To circumvent this numerical problem, the penalty of partially filled orbitals has to be reduced, i.e. by reducing the U value. Therefore, first the Hubbard U term for the regular Nb ions was removed and afterwards the U value for the antisite was reduced incrementally. At a value of  $U = 2.2\text{ eV}$  for the antisite Nb each starting configuration leads to polaron formation after relaxation. Additional tests with starting configurations at 300 K lead to the same result. With the set of parameters determined, the molecular dynamics can be conducted.

## 4.6. Molecular dynamics: Parameters and starting configurations

To conduct the MDs adequate starting configurations have to be generated first. Similar to the tests, this is achieved by conducting a MD in the uncharged system while utilizing a Berendsen thermostat for the chosen temperatures. The first 700 fs of the MDs are discarded to ensure that a (quasi) thermal equilibrium is reached. Using the mean distance of the O ions to the antisite Nb as a measure, it can be shown that the system is equilibrated sufficiently, as both amplitude and frequency of the O ion oscillation are mostly stable. Afterwards starting geometries and velocities are taken in 50 fs intervals from the MDs, resulting in 41 trajectories per temperature. This interval does not coincide with the O oscillation frequency, which ensures that the starting configurations are not too similar. The starting configurations are then used in new MDs in the charged system which no longer employ a thermostat. The choice of leaving the thermostat out of the picture is due to the improved comparability, as all MDs now only depend on the starting configuration. Additionally to the MDs in the charged system, MDs with the same starting configurations in the uncharged system are conducted in order to study the influence of the excess electron on the atomic movement. These calculations are performed for the temperatures of 20 K, 100 K, 200 K, 300 K, 600 K and 1200 K. To summarize the numerical parameters, all MDs use a kinetic energy cutoff of 85 Ry, a  $2 \times 2 \times 2$  Monkhorst-Pack  $k$ -point grid, PBEsol pseudopotentials, a Hubbard U correction of 2.2 eV applied only to the antisite Nb, as well as an ionic integration time step of 1 fs. The MDs in the charged system are conducted spinpolarized with the excess electron being restricted to be in the spin up channel. For the MDs which employ a thermostat a Berendsen thermostat with a time constant of  $\tau = 20$  fs is used.

### 4.6.1. The influence of the starting configuration

In order to generate a sufficient amount of starting configurations, the MDs with thermostat need to simulate a long trajectory, over 2 ps. Since this MD is not parallelizable, this is a choke point for the calculations. It would be advantageous to find another method to generate starting configurations. As explained in chapter 2.4, the initial velocity can be set using random velocities, which are scaled to fit the temperature. However, an approach for the atomic displacement is also needed. For this approach the displacements of the ions obtained by the MD with thermostat (at 200 K) are fitted using a Gauss function. Using this function as distribution, several amplitudes for the displacements are generated. The direction in which the displacement occurs is selected randomly. Together with the randomly generated velocities 50 new starting configurations are generated for the charged system. The MDs are conducted and the polaron formation and electron localization time determined using the methods and thresholds explained in the next section. Compared to the times for the thermostat generated starting configurations the mean localization time differs by 5 fs and the formation time by 8 fs, which is an acceptable accuracy. This shows

that if the magnitude of the displacements can be estimated, the random approach is most likely sufficient or at least gives a good idea for formation times. However, in the case of LN we did not know the amplitudes without conducting the MDs, which is why this method was not feasible. Additionally, this test gives an insight on the statistical relevance of the calculations: If 41 trajectories were no sufficient sample size, there would be virtually no chance that the randomly generated structures lead to similar formation and localization times. This means that 41 trajectories are sufficient to describe the system with statistical accuracy.

#### 4.7. Analysing the trajectories: Thresholds and additional methods

In order to analyse the trajectories reliable thresholds for the polaron formation have to be found. As already explained, the dispersion of the lowest KS conduction band, its position in the band gap, the mean O ion distance to the nearest neighbours as well as the local magnetic moment are suitable criteria. To investigate the individual formation steps we differentiate between the time which is needed for the electron to localize, referred to as electron localization time (or short localization time), and the time which is needed for the full polaron to form (localization + relaxation), referred to as polaron formation time. The time between the localization and formation time is the time which the lattice needs to relax and is therefore referred to as relaxation time. First the formation time is considered. As stated before, there is a direct connection between the position of the lowest conduction band minimum in the band gap and the absorption properties of the material. For a direct comparison the dielectric function  $\epsilon$  can be utilized. The dielectric function contains multiple optical properties of the system, like the refraction index or the absorption. The absorption in particular is contained within the imaginary part of the function, in which a peak shows an increased absorption.<sup>[1]</sup> The dielectric function is calculated within the regime of the independent particle approximation by constructing the Green functions on the basis of the calculated KS eigenvalues and solving the Dyson equation for the susceptibility. The interested reader may refer to Ref. 116 for an in detail explanation of the calculation of absorption spectra. The calculation of the dielectric function is done using the YAMBO program package.<sup>[117,118]</sup>

The dielectric function is calculated for different structures along a MD trajectory at 200 K. Since the optical properties of the system are known to be described accurately with the set of Hubbard U values of 5.2 eV for the defect Nb and 4.7 eV for the other Nb, those parameters are also used for the calculation of the dielectric functions, while the MD is performed at U=2.2 eV for only the defect Nb. The KS levels of the trajectory, its average defect Nb-O bond length, and the local magnetization at the defect as well as the dielectric functions at chosen points together with the dielectric function for the fully relaxed polaron are shown in figure 13. Noticeable many of the before mentioned criteria coincide by their peak positions. This is to be expected, as the polaron formation is a self-reinforcing process, the localized electron increases the bond length which in term increases the localization. Furthermore, it is apparent that a defect KS level deeper in the band gap results in absorption peaks at higher energy. The closest approximation of the dielectric function of the fully relaxed polaron is reached at a KS level 0.78 eV below the conduction band. This value is used as criterion for the completion of the polaron formation. However, a word of caution has to be in order for this choice. The dielectric function of the fully relaxed polaron has a peak close to the experimentally measured one (at 1.6 eV), thus it appears that the comparison is a quantitatively one. However, the situation in the experiment is not the same as in the simulation. In the experiment a multitude of polarons

are measured, which are all in different states due to their oscillations. This results in a broadened absorption peak at a lower energy than a fully relaxed polaron would assume. The absorption peak therefore would be expected at a higher temperature, but since DFT with PBEsol tends to underestimate the band gap (and subsequently absorption energies), this is compensated. For this reason the comparison with the experiment is rather of a qualitative nature. Nevertheless, this is sufficient for a definition for the polaron formation in the simulation.

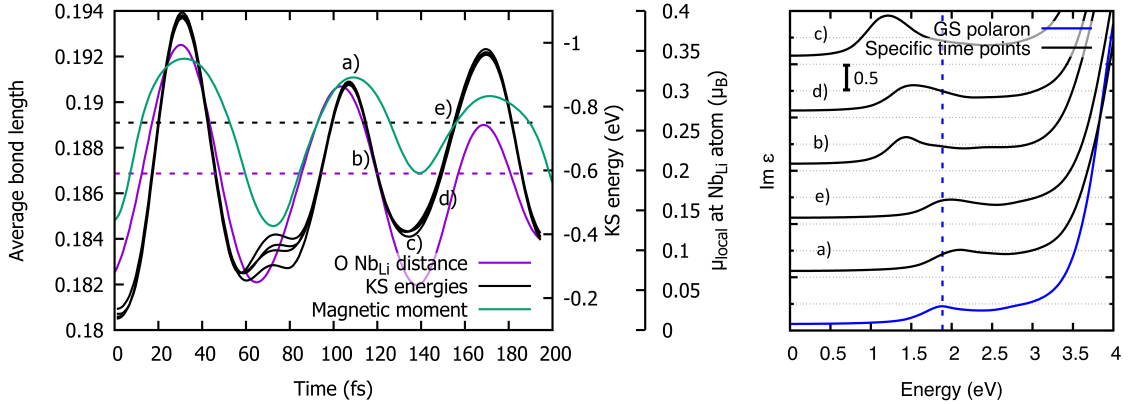


**Figure 13:** Left: Evolution of the Kohn-Sham eigenvalues of the uppermost occupied electron state at the four non-equivalent  $k$ -points and the sum of distances between the  $\text{Nb}_{\text{Li}}$  defect and the nearest O atoms surrounding the defect taken from a prototypical MD run at 200 K. Dashed lines show the equilibrium distance and eigenvalues. Right: Dielectric function calculated for snapshot structures at the times indicated in the left graph. For better visibility the functions are shifted vertically. In addition the dielectric function for the ground-state polaron is shown. The dashed line marks the peak maxima of the ground state dielectric function for better comparability.

For the electron localization the parameters of choice are the local magnetic moment and the dispersion of the Kohn-Sham states. To determine a threshold for these parameters the electron density is employed. The electronic density is plotted for several trajectories at all considered temperatures in 5 fs intervals. For each trajectory the first structure in which most of the density is located at the defect Nb and only residual parts are left outside is identified by visual inspection. An example of such development of electronic density is shown in figure 14. For those structures the KS dispersion as well as the local magnetic moment are extracted. These values are acceptably close to each other, regardless of the temperature. On the basis of these values the thresholds are determined, with the local magnetic moment exceeding  $0.18 \mu_{\text{B}}$  and the maximum of the difference of the KS energies falling below 0.04 eV. These definitions, however, lack of a description of the stability of the localization. Not every rise in magnetic moment will lead to a polaron and especially for the KS dispersion there can be random convergences which do not correspond to stable localizations. To account for this two additional criteria are added. First, the localization needs to be stable for a prolonged time. The criteria are checked for several consecutive time steps corresponding to a 15 fs time frame. The electron is only considered localized if the criteria are fulfilled for at least 85 % of these time points. Second, only localizations which lead to actual polarons are considered. This is achieved by first determining the first occurrence of a polaron by the criterion explained in the last paragraph and then checking the criteria described in this paragraph from this point on backwards. An example trajectory with the criteria, the electronic density and the band

structures is shown in figures 15 and 14. For the stability of the polaron the same method is used: If the above mentioned criteria are not fulfilled for 85 % of a 15 fs time interval the polaron is considered quenched. Generally the local magnetic moment as well as the KS dispersion predict the localization with only 1-3 fs difference. However, the local magnetic moment has a slightly better accuracy and the advantage of being a single parameter, while there are 3 KS differences to be accounted for. Therefore, this criterion is used for the evaluation of the mean localization times.

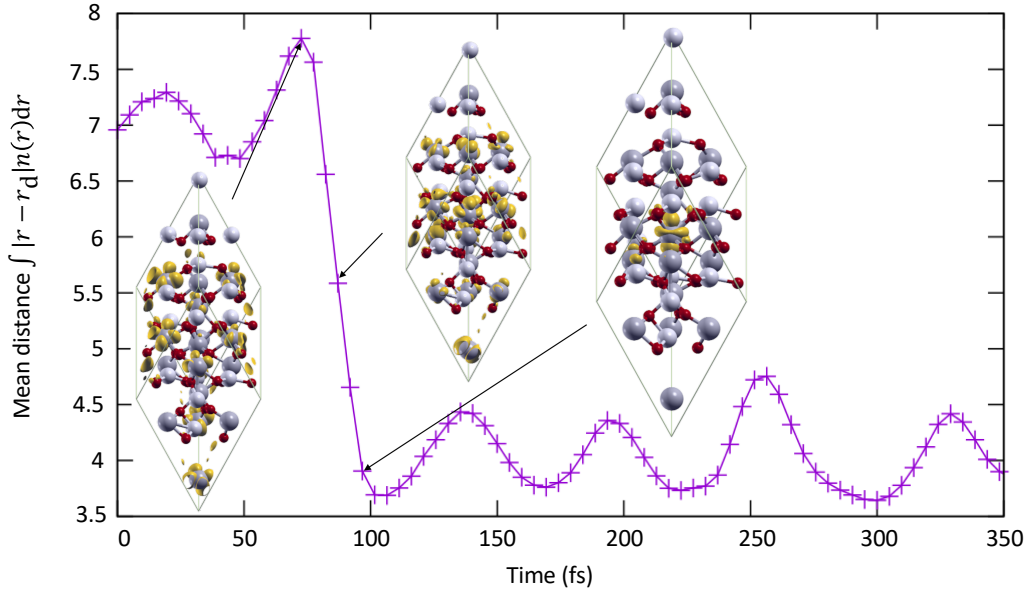


**Figure 14:** Evolution of the mean distance of the excess electron to the  $\text{Nb}_{\text{Li}}$  antisite atom during a MD performed at 300 K. Insets show the excess electron localization. It is to note that the electron localization coincides with the increase in magnetic moment in figure 15.

For the last part of the analysis the influence of the lattice dynamics on the polaron formation is studied. In order to do so the phonons of the system are considered. Phonons, the quantized lattice vibrations of a crystal, play an important role in the polaron formation, as a localized “phonon cloud” is an integral part of the quasi particle. The phonons are calculated using the harmonic approximation, diagonalization of the dynamic matrix and linear response to calculate the matrix as elaborated in chapter 2.5.

To describe the full system the phonons of the 80 atom supercell would have to be analysed. This poses two problems. On one hand, phonon calculations are more prone to errors the bigger the cell. On the other hand, the supercell consists of  $2 \times 2 \times 2$  single unit cells plus the defect. This results in a folding of the phonon bands, which makes the interpretation more difficult. To avoid these problems, the phonons of a  $1 \times 1 \times 1$  unit cell (without defect) at  $q = 0$  are calculated. A selection of those modes is shown in figure 16. All modes together form – by construction – a complete orthogonal basis set in the  $1 \times 1 \times 1$  unit cell. The influence of these modes on the polaron formation is studied by only considering a  $1 \times 1 \times 1$  subcell centred around the defect Nb in the  $2 \times 2 \times 2$  supercell. The motion of the atoms inside this sub cell is projected onto the phonon displacement vectors. Using the amplitude of these projections one can calculate the contribution of the modes to different structural parameters. As already stated the most prominent one for the polaron formation is the mean distance of the closest O ions to the defect. By comparing the phase and the absolute contribution of the modes to the mean distance one is able to identify the modes important to the polaron formation.

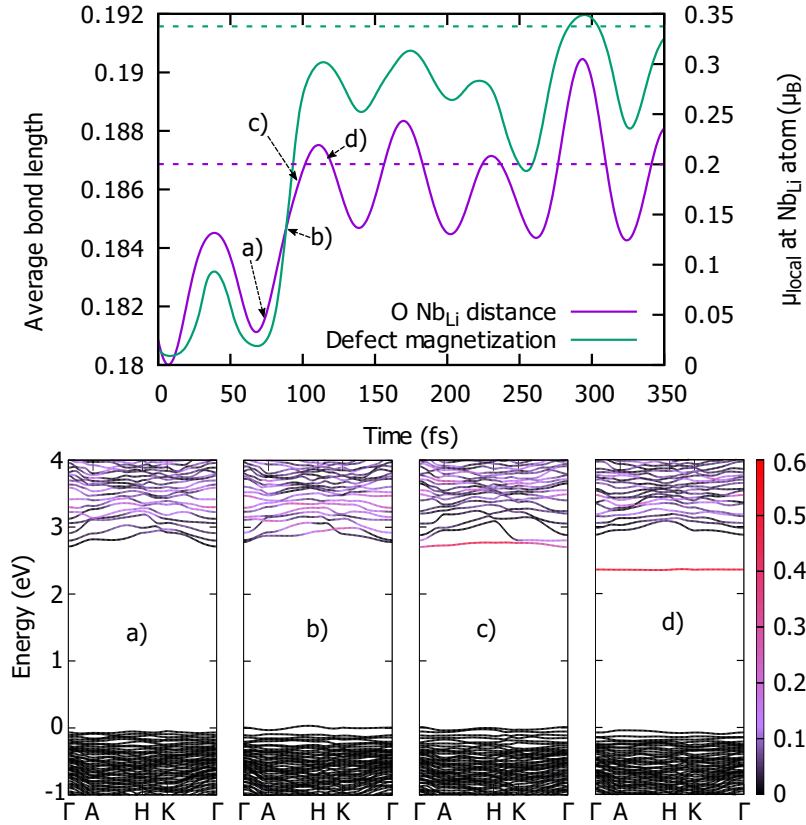


**Figure 15:** Evolution (same MD as in Fig. 14) of the local magnetic moment at the defect Nb<sub>Li</sub> and the average bond length between the Nb<sub>Li</sub> atom and the nearest O atoms surrounding the defect. Dashed lines mark the magnetizations and O positions that correspond to the ground-state polaron. For specific times, complete band structures are shown exemplarily, with colors indicating the electron localization. The increase in magnetic moment is apparently accompanied by a reduction of the dispersion of the lowest state.

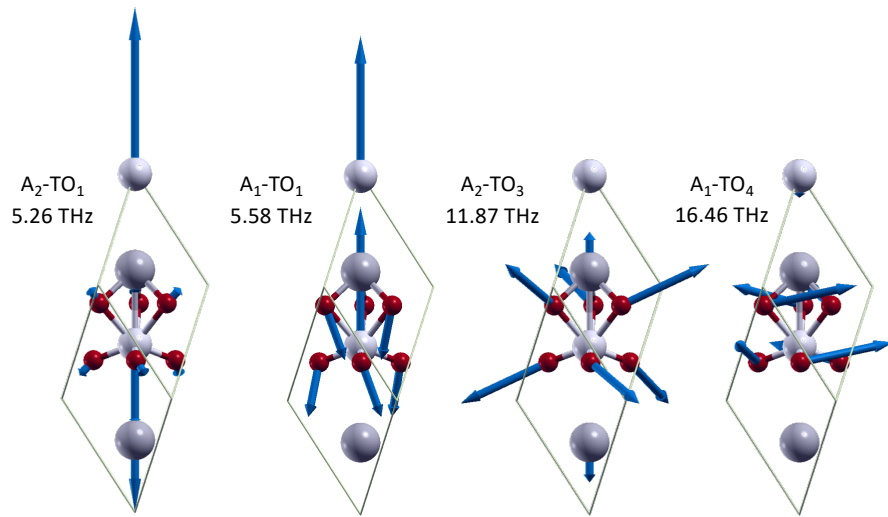


**Figure 16:** Subset of phonon modes for the LN unit cell. The first two modes,  $A_2\text{-TO}_1$  and  $A_1\text{-TO}_1$ , are low frequency modes which are mainly shear motion between the O ions and the surrounding lattice. The higher frequency  $A_2\text{-TO}_3$  and  $A_1\text{-TO}_4$  modes are breathing modes of the O ions. All four modes were found important for the polaron formation.

## 4.8. Results

With all tools for the analysis explained, we can now discuss the results, beginning with the localization and formation times.

### 4.8.1. Localization and formation times

Those are shown (in dependence on the temperature) in figure 17. Though not very pronounced, a tendency can be observed. Higher temperatures lead to longer localization and formation time, while the time between those two (relaxation time) is mostly constant. It seems that the thermal motion obstructs the polaron formation. As already shown in chapter 4.5, a relaxation from a disturbed system leads to polaron formation, the polaron formation is therefore without a barrier. Without external forces the atoms are hence accelerated towards a polaronic configuration. Additional velocity by the temperature is most likely to move the atom from the “ideal” path, leading to longer formation times. This effect becomes even more pronounced if the ground structure (therefore at 0 K) of congruent LN is considered. If an electron is added to the ground state it is already partially localized at the  $\text{Nb}_{\text{Li}}$  site, leading to a fast formation. Disturbing this structure is more likely to move it into a configuration in which the electron can not localize directly. Figure 17 also shows the minimum polaron life time. While in the last section a clear definition for the stability was given, the adjective “minimum” had to be included, as many polarons – especially for low temperatures – stayed stable for the whole duration of the molecular dynamic, it could be stable for much longer. In fact, for the two lowest temperatures of 100 K and 200 K all formed polarons are stable for the simulation time. Due to this, the life time is not shown for very low temperatures, and shown as a dashed line for the middle temperatures. Nevertheless a clear dependency can be seen, with lower lifetimes for higher temperatures.

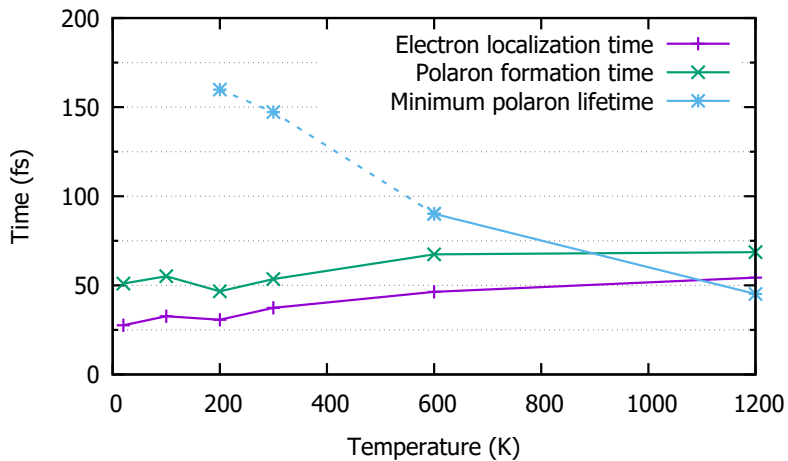


**Figure 17:** Dependence of the average times required for electronic localization, polaron formation, and polaron quenching on the simulation temperature. At low temperatures many polarons live longer than the simulation time, making the calculated average lifetime unreliable. This is indicated by both the term “Minimum polaron lifetime” and the dashed line.

Experimentally, the polaron formation times have been reported in a wide range between 70 fs and 400 fs for congruent LN,<sup>[107,111,119–121]</sup> with even higher times around 1500 fs for stoichiometric LN.<sup>[111]</sup> Our results between 50 fs and 80 fs lie on the low end of this range. Instead they fit much better to the experimental values for free polarons which are lower

than 100 fs.<sup>[111,120]</sup> This effect is most likely due to the neglect of polaron hopping in our simulations. As already stated, polaron hopping is the process of one electron hopping from one lattice site to another one, creating a new polaron at this site while quenching the other one. It is assumed that most electrons first form free polarons, as there are many more Nb<sub>Nb</sub> sites than Nb<sub>Li</sub> sites. After this the electrons can hop from site to site, until eventually they will get close enough to an antisite, where they are trapped as a bound polaron. This assumption is backed up by the observation, that the formation time in stoichiometric LN is longer than in congruent LN. Due to the lower defect concentration the average distance between the initially excited electron and the defect is larger. This means more hops are needed for the electron to get close enough to the antisite to collapse onto it. The distance at which this collapse is inevitable was already introduced as trapping radius. The trapping radius is temperature dependent and was calculated on basis of Monte Carlo simulations in Ref. 115. At a temperature of 350 K the radius is around 8.6 Å, it decreases with higher temperatures and vice versa, which further solidifies our finding of shorter formation times at low temperatures. Since our unit cell has a lattice parameter of 11 Å, the electron is bound to localize directly at the defect and to not take a detour as a free polaron. With only the direct localization as an option, the bound polaron has the same formation mechanism as the free polaron, which brings its formation time also in the regime of the free polaron.

The effect of the trapping radius getting smaller with higher temperatures can already be seen implicitly by the rise in polaron formation time with rising temperature. However, it is more apparent if the distribution of the formation times is considered. At low temperatures, the distribution is characterized by a peak within the first 20 fs, many electrons are even localized straight from the beginning. After this peak the formations are distributed more evenly. The distribution is shown in a simplified manner in figure 18. At low temperatures the trapping radius expands and more configurations lead to directly trapped electrons. With higher temperatures this peak flattens more and more, as less configurations ensure the direct formation. This corresponds to a smaller trapping radius.

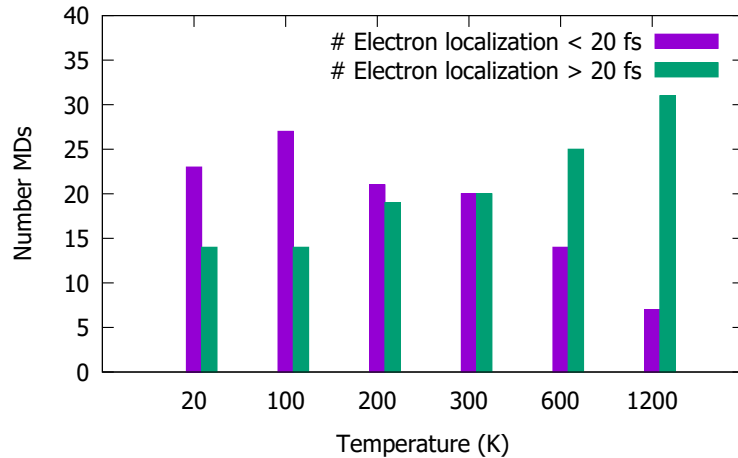


**Figure 18:** Number of trajectories with electron localization times above and below 20 fs depending on the temperature.

Another interesting feature becomes apparent, if the trajectories are considered which do not lead to polaron formation within the simulated time frame. Considering the temperature range between 100 K and 300 K basically all trajectories lead to polaron formation.

For the temperatures of 20 K, 600 K and 1200 K this is not the case. For 600 and 1200 K this is obvious from the previous findings, higher temperatures impede the formation and stability of polarons. For 20 K the situation changes. With a large trapping radius, most electrons localize fast at the defect. If the starting configuration does, however, not lead to an immediate localization, there is little thermal motion to reach a configuration inside the trapping radius. In the regime between 100 K and 300 K there is enough thermal motion to escape those configurations, but not enough to overly hinder the formation.

#### 4.8.2. The influence of the Hubbard U

As already seen in the construction of the bound polaron, the Hubbard U value is a critical parameter which influences the polaron formation. It is therefore important to get an estimate on how large this influence is on the localization formation times. As already stated, higher values can lead to numeric instabilities. If the convergence threshold for the self-consistency cycle is raised – which lowers the accuracy – several trajectories, however, do converge. In order to compare the parameters, MDs were conducted at 200 K with  $U=4.7 \text{ eV}$  at the antisite, where the starting configurations were the same as for the MDs with  $U=2.2 \text{ eV}$ . Those MDs are divided into early electron localizations and late electron localizations and compared. For the early localizations little changes occur, with localization times being maximally 3-5 fs earlier in the case of  $U=4.7 \text{ eV}$ . For late localizations two cases can occur. In one case the localization stays qualitatively the same, with deviations of 5-8 fs. In the other case the electron localizes substantially earlier (10-40 fs). This case occurs if the electron is close to localizing (or even already partially localized) in the  $U=2.2 \text{ eV}$  case. A higher U binds the electron more strongly and has a stronger influence on the structure, therefore the electron localization can occur at higher ion velocities. This in turn increases the trapping radius, which enlarges the early-localization peak in the distribution. This is also the reason why the short localization times are barely effected, as they start in a nearly trapped configuration also in the 2.2 eV case. However, it is difficult to quantify this effect, as the range in the shortening of the localization times is large. Nevertheless for the low to middle temperature range it can be largely discarded, as it only effects a fraction of the trajectories with long localization times, and many electrons localize early. For higher temperatures this effect becomes more important, as more trajectories have late localizing electrons. Overall a higher Hubbard U value leads to shorter localization times, with the effect being small at low temperatures and becomes more important at high temperatures.

Considering the opposite directions, MDs were calculated using no Hubbard U correction. Like earlier, MDs with early and late electron localizations are compared. For the short localization times the electron takes around 5 fs longer to localize, for the long localization times around 10 fs. The trapping radius seems to be not as much influenced as by the increasing of the Hubbard U value. However, it is to mention, that the stability of the polaron diminishes. While for  $U=2.2 \text{ eV}$  most polarons stay stable until the end of the calculation, for  $U=0 \text{ eV}$  the electron de- and relocates while the O ions oscillate.

As a final test, the full “spectroscopical” set of  $U=5.2 \text{ eV}$  for the antisite Nb and  $U=4.7 \text{ eV}$  for the other Nb<sup>[104]</sup> is considered. This set shows a different behaviour than the previous ones. Here no late electron localizations are observed, the electron is either localized directly at the antisite, or no polaron forms. This is explainable due to the effect of the U correction to promote either fully occupied local orbitals or empty ones, partially filled ones are unfavoured. As seen in figure 14, during a MD at  $U=2.2 \text{ eV}$  with late localization, the

excess electron is localized evenly at the non defect Nb ions in the beginning. With such a distribution, changes in electronic occupation between those atoms are disadvantageous, as the energy which one electron loses by lowering its occupation, the other one gains by raising its occupation. The self-interaction error then ensures that the evenly distributed configuration is energetically favourable. The Nb antisite is empty in this configuration, which is again favourable. In order to move the electron to the antisite, both U values lead to unfavourable configurations, as all electrons are partially occupied in the intermediate steps. This set of U values hence “freezes” the electrons in their starting occupation – either at the antisite or the other Nb. This set is therefore not suitable for a MD.

#### 4.8.3. Lattice relaxation

At last we study the influence of the lattice motion on the electron localization and relaxation times, beginning with the relaxation times. As already stated the localization of the electron causes the surrounding oxygen cage to expand. The maximum of this expansion roughly corresponds to the formation criterion as can be seen in figure 13 and 15. We study the influence of the lattice motion by projecting the motion of the ions in a 1x1x1 subcell around the defect onto the LN phonon modes as explained in chapter 2.5. By considering their proportion on the mean O distance to the defect their impact on the relaxation is assessed. We identify four modes,  $A_2TO_1$ ,  $A_1TO_1$ ,  $A_2TO_3$  and  $A_1TO_4$  (nomenclature used from Ref. 122) which are especially important for the O-cage expansion. Those modes are shown in figure 16. To gain a clearer picture, the trajectories with excess electron are compared to the one without excess electron but with otherwise same starting conditions, which shows the influence of the electron. Four such comparisons are shown in figure 19, where on the left hand side the trajectories with excess electron and on the right hand side without excess electron are shown. Those trajectories were conducted at 600 K and were chosen as they display the further discussed features most clearly and have the electron localized within the first 5 fs, which makes the comparison easier. For all trajectories prominent features of the modes, like the “double-peak” of the  $A_2TO_1$  mode in 19 a) and b), the steep decline of mode  $A_2TO_3$  in c) and d) or the continuous decline of mode  $A_2TO_1$  in e) and f) are existent in both trajectories with and without excess electron. This shows that the electron modifies the modes rather than completely dominating the dynamics, which underlines the importance of the modes for the polaron formation. Generally we observe that modes with lower frequency are altered less than modes with high frequency.

Furthermore, we explicitly find an influence of the phonon phase relation on the relaxation times. For all trajectories holds that once the electron localizes, the O ions begin to be pushed outwards. This process can be either dominated by the high frequency  $A_1TO_4$  and especially the  $A_2TO_3$  mode, or the low frequency  $A_2TO_1$  or  $A_1TO_1$  mode. If the  $A_2TO_3$  mode is in a O-cage shrinking phase, like in figure 19 f), its motion can not be directly inverted by the electron, but only damped (see fig. 19 e) ). In this case the  $A_2TO_1$  mode is altered to expand the O cage for a longer time. Since this mode as a low frequency mode is only modified slightly, this leads to an overall longer relaxation time between 40 and 50 fs in this case. The opposite occurs if the  $A_2TO_3$  (and to a lesser part the  $A_1TO_4$  mode) is in a O-cage expanding phase as in fig. 19 h). In this case the expanding motion of the mode is amplified and leads to a fast relaxation time (here around 20 fs), while the low frequency modes are unaffected. This behaviour might explain the overall slightly shorter relaxation times at higher temperatures, as with higher temperatures the high frequency modes are more often occupied. As a final finding, the increase of the O cage due to the electron leads to a less rigid Nb-O bond. Comparing the frequencies of the O cage motion,

the structure without electron oscillates at around 20.5 THz, while in the case of the excess electron it oscillates around 17.5 THz.

Now we have a look on the influence of the lattice on the electron localization. As stated in chapter 4.3, the common explanation for the electron localization is a spontaneous localization due to a disturbance in the lattice. Such a disturbance should be observable in the MDs, revealing a microscopical mechanism leading to the localization. We again use a decomposition of the ion movements in phonon modes to find such a mechanism. A possible mechanism would be again the O-cage, with the idea that the electron needs enough space to move through the cage to the antisite, which would make it visible by means of the phonons. However, no such dependency could be found. Additionally to the phonons, the localization was studied using the deformation of the O-cage, the minimum O-distance to the Nb antisite, the deformation of the surrounding Nb and Li ions and visual inspection of the structures. Furthermore, a PES with the O-ion movement according to the phonon modes as structural coordinate was calculated in order to find local minima where the electron is delocalized. Despite this different methods no localization mechanism was found, indicating that the localization mechanism does not take place in the direct vicinity of the defect but rather encompasses the whole cell.

#### **4.9. Non-adiabatic potential energy surface hopping in lithium niobate: The problems of a crystal**

Comparing the dynamics of the oxirane molecule and the lithium niobate crystal one might wonder why in one case the electronic relaxation was considered, while the other one starts directly in the lowest excited state. On one hand, this is a question of the computational effort. While oxirane as a molecule has discrete energy levels which are clearly separated, LN has a much denser density of states. If for example an excitation roughly 1 eV above the lowest conduction band spans four KS states for oxirane, it spans 20 states in LN. Correspondingly more excited states have to be calculated for the hopping algorithm. On the other hand, there are fundamental problems in constructing the needed wave function of the system. As stated in chapter 2.7 Slater determinants of the occupied single particle KS orbitals are used to construct the wave function. If an active space which includes the highest valence band state up to the band occupied at the highest excitation is considered, for a single electron excitation there is only one KS state – the one in which the electron is elevated – in the determinant for each excited configuration. However, for a crystal there is no single KS function for one band, but one for each  $k$ -point per band. Due to the lack of periodicity in a molecule this is no problem, since all states show no dispersion and hence are independent of the  $k$ -point. In a crystal the orbitals are dependent on the  $k$ -point, therefore there is no simple choice on how to construct the wave function. One could decide to use a characteristic point to extract the eigenfunctions from, like the Baldereschi point or the  $\Gamma$  point. This leads to a massive underestimation of the hopping rate, for LN the possibility of an electron hopping according to the Schrödinger equation is below 0.1 % within the first 200 fs if the lowest four conduction band states are considered. This is most likely due to the missing interaction between the different  $k$ -points. The conduction bands have a non discardable dispersion, the density of states in fact forms a continuum for the conduction band. This should allow an excited electron to relax to the bottom of the conduction band. If only one  $k$ -point is considered, the majority of those states is ignored. Furthermore, for each  $k$ -point the states may change individually – as seen by the straightening of the band structure in figure 15 (the middle changes independently from the sides) – which makes the interaction between the  $k$ -points even

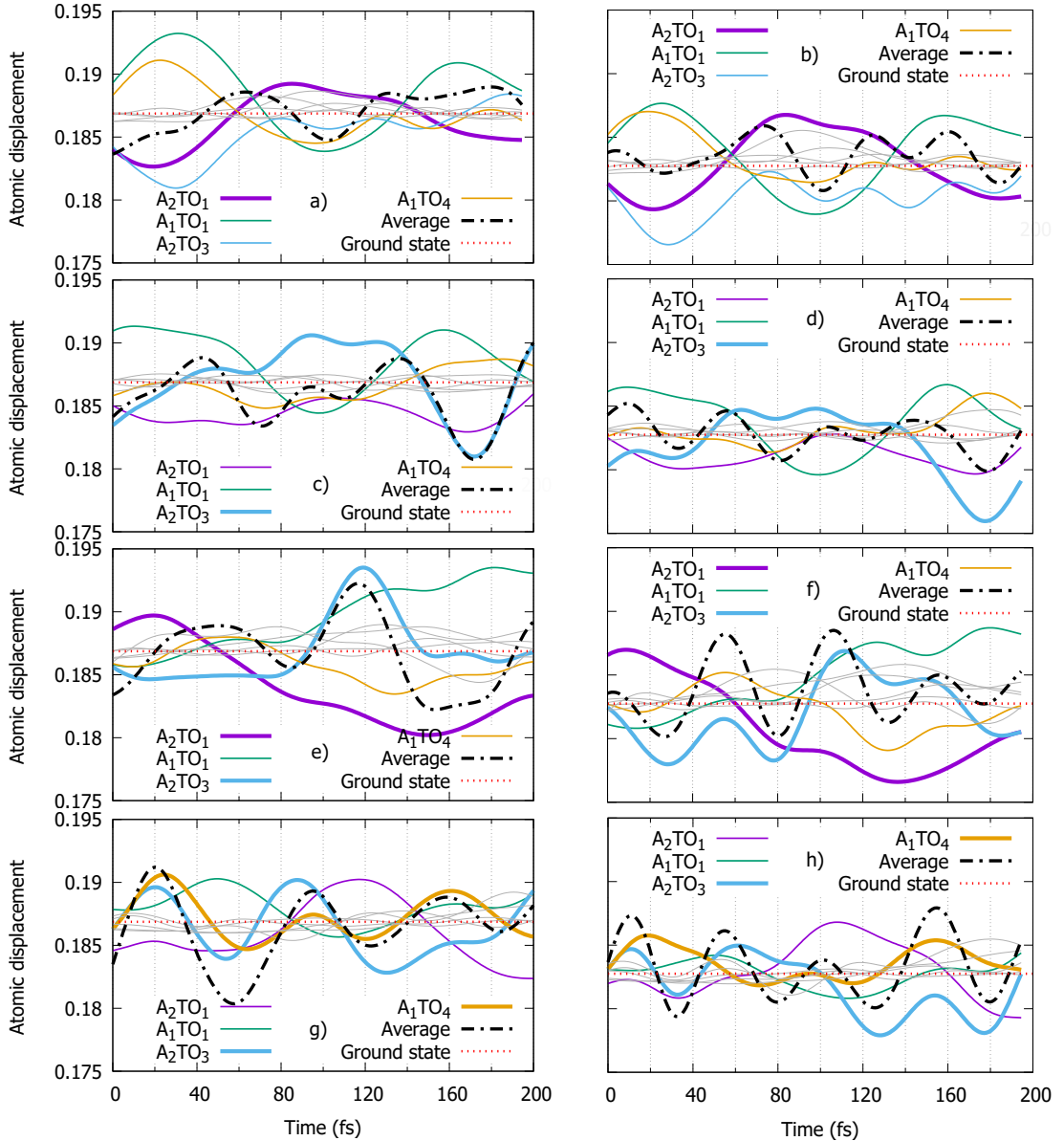


**Figure 19:** Evolution of average O-NbLi distances for eight example trajectories at 600 K with (left) and without (right) excess charge. The trajectories on the rhs have identical starting configurations as their counterparts on the lhs. The atomic movement is projected onto relevant bulk phonon modes (see figure 16) and the O-NbLi distance that would result from an exclusive excitation of the respective mode is shown. The 'ground state' graph shows the average O-NbLi distance for the corresponding relaxed structure at 0 K.

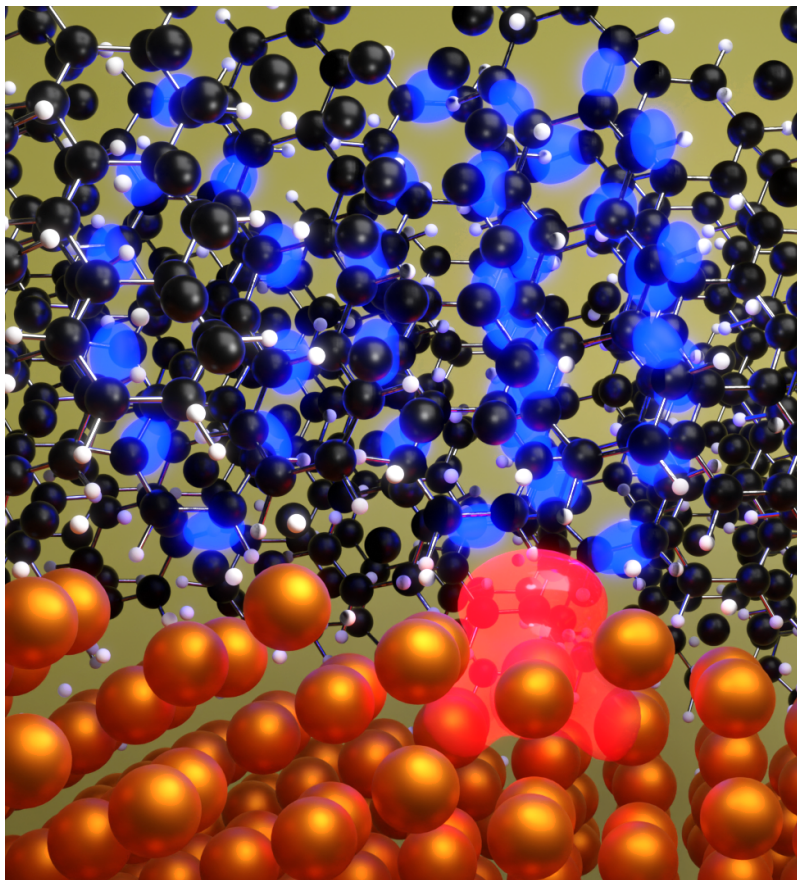
more important. Unfortunately it is not trivial to include such an interaction. Due to their phase relation, the states of the  $k$ -points are always orthogonal to each other, no overlap is possible. A possibility to bypass this problem is to fold the band structure, which overlays the  $k$ -points. This is achieved by increasing the size of the unit cell, a doubling in size in real space corresponds to halving the unit cell in reciprocal space. Due to computational restrictions this is not viable for this system.

Another possibility would be to change the hopping algorithm to get rid of the  $k$ -points altogether. One option would be the Landau-Zener formalism, which estimates the hopping probability by the PESs of the excited states and their derivatives.<sup>[123,124]</sup> This formalism, however, has the disadvantage of not being an *ab initio* formalism, but a phenomenological one. Another possibility could be to change the basis set. If one changes from the calculation in reciprocal space to real space, for example by projecting the wave functions onto a tight binding basis set or a transformation to Wannier functions, one is able to remove the  $k$ -point dependency and implicitly include the  $k$ -point interaction while calculating the overlap between bands. A word of caution is in order, since often new orthogonalities are introduced during such transformations, meaning that the problem might just be moved to another point. However, as we will observe later, the surface hopping algorithm seems to work best for localized states, which increases the probability for such a transformation to improve the hopping rates as Wannier functions can be used to maximise the localization.<sup>[125–127]</sup> Last but not least one could consider explicitly calculating electron-phonon interaction coefficients for impulse carrying phonons. While this methods does not give hopping probabilities during a MD, it can be used to get an estimate on the ratio of the on site interaction and the interaction between  $k$ -points, which in turn could be used to scale the hopping probabilities. Nevertheless, with the methods implemented in the LIBRA-X program package the hopping can not be calculated for this problem, which is why it is not considered above.

In summary molecular dynamics were conducted to study the formation of polarons in lithium niobate. The polarons were modelled by adding an extra electron to the system. For free polarons the self interaction error proved too strong to describe polaron formation in an environment with finite temperature, while the bound polaron could be described using the DFT+U approach. The polaron formation was monitored using the lowest conduction band position, the local magnetic moment at the Nb<sub>Li</sub> site and a decomposition of the atomic movement around the antisite into phonon modes. It shows that the barrier-free polaron formation is hindered by the movement caused by the temperature, leading to longer localization- and formation- (and shorter life-) times at higher temperatures. This is in line with the larger trapping radii at lower temperatures calculated in previous works. The formation time for each trajectory was found highly dependent on the phase of the phonon modes at the electron localization, with short formation times in case of an “outwards“ phase of the high frequency A<sub>1</sub>TO<sub>4</sub> and A<sub>2</sub>TO<sub>3</sub> breathing modes and long formation time for the opposite phase, where the expansion is mainly done via low frequency shearing modes A<sub>2</sub>TO<sub>1</sub> and A<sub>1</sub>TO<sub>1</sub>. The calculated formation times are between 50 fs at low temperatures and 75 fs at high temperatures, setting them at the lower end of experimental values. This is most likely due to the neglect of polaron hopping due to the cell size, which is small enough to only allow for a direct capturing of the electron.

From a computational point of view lithium niobate highlights the need of changing parameters which can occur by switching from a static structure to a molecular dynamic. In this case the Hubbard U values optimized for the optic properties of the polaron in its relaxed ground state are not suitable for molecular dynamics. Furthermore, it shows

the difficulty to describe the surface hopping of highly dispersive states with the  $k$ -point dependent Slater-Determinant approximation of the wave function. With the knowledge gained from the molecular oxirane and the solid lithium niobate, we now move on to the biggest considered system – the exciton dynamic at the silicon-tetracene interface.



Exciton dynamics at the silicon-tetrace interface

---

## 5. Exciton dynamics at the silicon-tetracene interface

As the name already states, the Silicon-Tetracene (Si-TC) interface model consists of two surfaces containing silicon and tetracene. Modelling such an interface poses a challenge, since in order to model a surface one has to capture the transition from the periodic bulk structure to the non-periodic surface. Therefore, more atoms perpendicular to the surface have to be included than in the case of the ideal bulk material. Furthermore, the lattice constants of the materials have to be matched in order to reduce the stress between the surfaces so the interface can form. Finding a common denominator leads to multiple duplications of the cell lateral to the surface. Due to these circumstances the two dimensional interface needs considerably more atoms than the zero dimensional molecule or the three dimensional solid, which of course increases the computational effort. But before going into further details of the model, lets have a look at the components and why this interface is of particular interest.

### 5.1. Silicon, tetracene and solar cells

Silicon (Si) is a semiconductor with an indirect band gap of around 1.1 eV.<sup>[128]</sup> In its monocrystalline form it crystalizes in a diamond structure with a lattice constant of 5.43 Å.<sup>[129]</sup> Due to its mechanical and chemical sturdiness as well as its abundance it has become the preferred semiconductor for all kind of electronic devices.

Tetracene (TC) though is far less wide spread. It is an aromatic hydrocarbon with four carbon rings saturated with hydrogen atoms ( $C_{18}H_{12}$ ), see figure 20. Due to van der Waals interaction tetracene can form crystals with different structures, most notably the bulk phase (also known as TC1) and the thin film phase (also known as TC2).<sup>[130]</sup> Tetracene has its lowest excitation energy of roughly 2.3 eV and is therefore also a (organic) semiconductor.<sup>[131]</sup> As organic semiconductor it finds moderate usage in organic LEDs or field effect transistors.<sup>[132]</sup> It has, however, another interesting property, as singlet fission occurs in TC. For the excitation of one electron, there are two possibilities. In one case the electron is excited with its spin staying the same, resulting in a net spin of 0. This excitation is referred to as singlet excitation and yields the before mentioned excitation energy of 2.3 eV in tetracene. The other option is an excitation where the spin is flipped. This results in a net spin of 1, referred to as triplet excitation. As the triplet excitation contains two unpaired electrons with identical spin, these identical particles are subject to the exchange interaction. The exchange interaction leads to a spatial separation of the electrons, which decreases the energy of the excitation.<sup>[133]</sup> However, this kind of excitation is very improbable, as the flipping of a spin during an excitation is unlikely (also called spin-forbidden).<sup>[134]</sup> In the case of TC the triplet excitation energy is around half the energy of the singlet excitation (it is half the energy of another singlet excitation state to be exact).<sup>[131]</sup> This makes it possible to obtain triplet excitations without needing a spin forbidden process: First a singlet is excited with a net spin of 0. This singlet splits up into two coupled triplets, where one has a spin of 1, the other one of -1. Therefore, a net spin of 0 is retained, the process is spin allowed. Through dissociation processes the triplets decouple which leaves two independent triplets in the TC. This process is referred to as singlet fission.<sup>[135]</sup>

This singlet fission process makes tetracene in conjunction with silicon a candidate for hybrid solar cells. Solar cells consist of two differently doped semiconductors (usually silicon), one with a surplus, one with a deficit of electrons. The difference in electron concentration

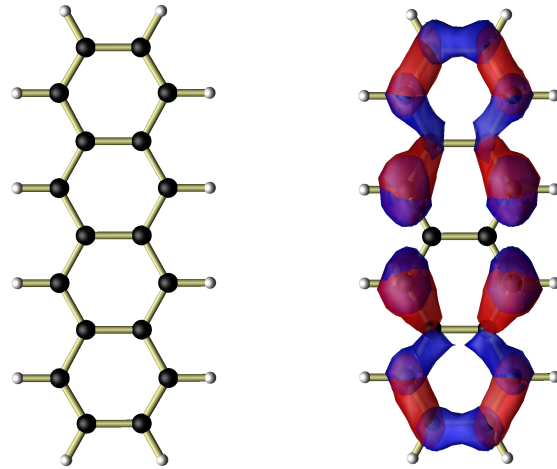


**Figure 20:** Tetracene molecule with (rhs) and without (lhs) triplet excitation. White atoms are H atoms, black ones are C atoms. Blue isosurfaces correspond to the excited electron, red to the hole state.

leads to a diffusion process which creates an electric field between the semiconductors. If an electron is excited in this configuration, the electron and the hole it leaves behind are separated by this field and accelerated towards the contacts, a current is produced.<sup>[136]</sup> Therefore, the creation of electron-hole pairs (also referred to as excitons) is crucial for the functioning of a solar cell. Whether an excitation can occur or not is a question of the energy for the excitation and the band gap of the semiconductor. The source for the excitation is of course the solar radiation, the semiconductor usually silicon. The sun produces a black body radiation at 5800 K, and is hence a wide spectrum.<sup>[137]</sup> However, radiation with energy below the band gap of 1.1 eV can not induce an excitation, radiation with higher energies “waste“ part of their energy, as the energetic position of the electron in the conduction band is irrelevant. Additional effects as a reduced absorption at shorter wavelength decrease the efficiency further. These factors combine into an upper limit for the efficiency of single junction solar cells, the Shockley-Queisser limit, which lies at about 33 % for silicon solar cells.<sup>[138,139]</sup>

This limit is tried to be overcome by the use of hybrid solar cells, where not one, but different semiconductors are utilized. One such semiconductor could be tetracene: Due to its larger band gap it can utilize shorter wavelengths more efficiently. As a result of the singlet fission it can transform one exciton into two excitations with half the energy. With the band gap of Si at 1.1 eV and the triplet energy roughly at 1.25 eV there is the possibility to transfer the exciton from the TC to the Si, where it can contribute to the electricity production. There are two possibilities to transfer the excitation to the silicon: On one hand, the exciton can recombine, which creates a photon which then excites an exciton in the silicon. Due to the recombination of a triplet being spin-forbidden this process is very unlikely to occur. On the other hand, the electron and hole are transported directly into the silicon. For this to occur there has to be an overlap between the wave functions describing the tetracene and the ones describing the silicon. However, no such overlap and thus little to no exciton transfer has been reported.<sup>[140-142]</sup> Increasing the overlap is a task which has been tackled by several experiments and different approaches,<sup>[140,143]</sup> with the hafniumoxynitride interlayer of Einzinger *et al.*<sup>[144]</sup> being one of the more successful ones. Though many experiments were conducted, often there is little known what causes an increase or decrease in the exciton transfer rate. This makes it especially interesting to

look at the problem from a simulation point of view. The following chapter is divided into three sections: First, the ideal Si(111)-TC interface is modelled and its static properties are discussed. Second, a point defect is introduced to the Si surface and the changes in the Si-TC band alignment and exciton localization are observed. In the third part the defect model is used to gain insight in the dynamical properties of the system.

## 5.2. The ideal Si(111)-TC interface

### 5.2.1. Modelling

For modelling an interface first the individual parts have to be considered. While the Si(111) surface is well known and defined, the TC surface can occur in different configurations, depending on the thickness of the TC film. In thick films (more than 20 monolayers) the bulk phase (designated with TC1) is observed. In smaller films the thin film phase (TC2) is observed. Both structures show a zig-zag like orientation of the TC molecules; however, in the case of the bulk phase the molecules show a higher inclination towards the surface (see figure 21). Aldahak *et al.* report an additional phase which forms in very thin films (thinner than three monolayers) and therefore occurs directly at the transition from the Si to the TC.<sup>[130]</sup> This phase is close to the TC1 phase, making the TC1 phase one of the phases of especial interest for the interface. As already stated the main difference between the TC1 and TC2 phase is the inclination of the molecules. In order to gain a simpler model additionally to the TC1 phase a simplified phase is considered. In this phase the volume of the unit cell is reduced in such a way that the molecules have a 90° inclination to the surface, as there is not enough space for the molecules to tilt. Since the upright standing molecules are laterally close, this phase will be referred to as high density (HD) phase. For the sake of simplicity the bulk-like phase will be referred to as low density (LD) phase.

For both models one single monolayer will be considered, thus by keeping the absolute atomic positions fixed, straightening the cell in z direction and adding a vacuum layer in z direction, one gains the unit cells for the respective surfaces. In order to model the interface the lattice constants of both surfaces have to roughly match. In order for this to happen, a common denominator for the lattice constant of Si(111) and the TC models has to be found. For the bulk phase the lattices match for a 1x4 repetition of the TC unit cell similar to the modelling of Ref. 130, for the high density phase the match occurs at a 2x2 repetition of the corresponding TC unit cell. With the planar dimensions of the cell fixed, the height of the cell has to be determined. For this the Si surface has also to be considered. The Si(111) surface is modelled using four Si bilayers, where the one side of the Si is fixed at its bulk positions, this side terminated using H ions. The interface side is also passivated with H ions. Considering an additional vacuum layer of roughly 10 Å and furthermore relaxing the structures, one results in the structures shown in figure 21.

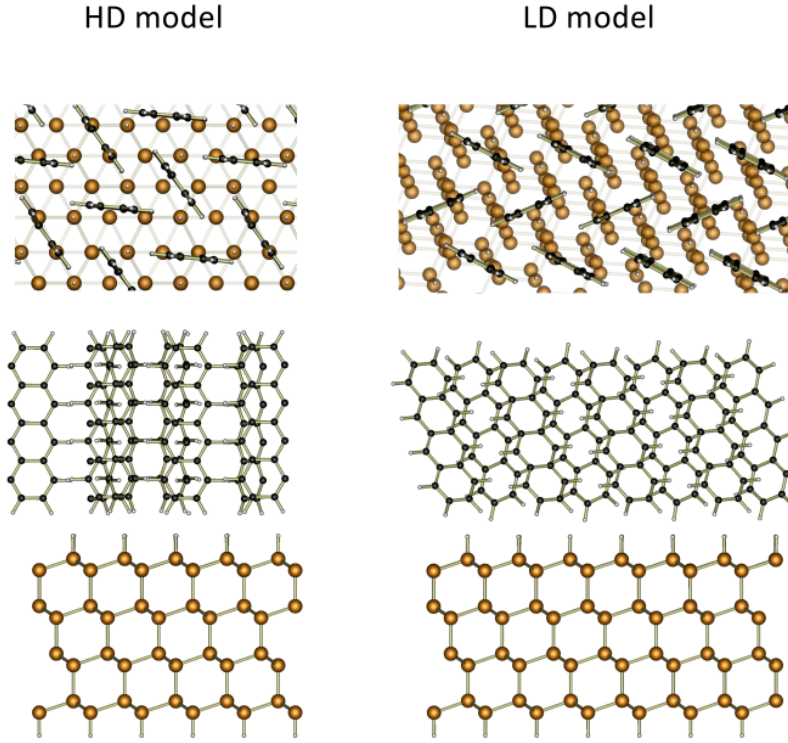


**Figure 21:** Top and side view of the high and low density phase. The top view is oriented along the long axis of the TC molecules, resulting in a  $0^\circ$  and  $25^\circ$  angle to the Si surface normal for the HD and LD model respectively.

With the structural model set all that remains are the computational parameters. For both models a wave function cutoff of 30 Ry and a  $2 \times 2 \times 1$  Monkhorst-Pack  $k$ -point grid is utilized. In order to incorporate the intermolecular van-der-Waals interaction, the DFT-D2 Grimme correction is applied.<sup>[145,146]</sup> If not stated otherwise in the following paragraphs, the system is relaxed using PBE pseudopotentials, with the lowest Si bilayer fixed at the bulk positions as well as with fixed terminating H ions. Afterwards the relaxed structure is recalculated using the HSE hybrid exchange-correlation functional with an exact-exchange fraction of 25 %, a  $k$ -point grid of  $4 \times 4 \times 1$  and a  $q$ -point grid of  $2 \times 2 \times 1$ .

### 5.2.2. Excursion: Which (hybrid) functional to choose?

For an interface the choice of a fitting functional is especially complicated, since two different materials have to be covered. There are several possibilities to approach this problem. First one could consider the PBE0 functional. The PBE0 functional is a parameter free (except for the exact exchange parameter) functional, which is known to work well for a wide set of materials.<sup>[147]</sup> Furthermore, the structure is relaxed with its non-hybrid form, the PBE functional. Second, the HSE functional could be considered. The HSE functional is more limited in its scope, but it is optimized for describing semiconductors, including Si.<sup>[148]</sup> As the silicon side of the interface ends in the Si bulk structure, this functional could be desirable. Apart from that, one could optimize the functional for the TC surface. The probably best functional for this would be the B3LYP functional, which is usually used for describing molecules.<sup>[149,150]</sup> Furthermore, one can change the exact exchange parameter for the functionals. While there are standard values for these parameters, they can be adjusted to reproduce experimental results for example. Last but not least one could use

	HSE-25	PBE	HSE-40	B3LYP	Experiment
$E_{\text{Si bulk}}^{\Delta}$	1.21	0.57	1.64	1.99	1.17 <sup>a</sup>
$E_{\text{TC molecule}}^{\Delta}$	4.68	4.54	4.74	4.69	5.9 <sup>b</sup>
$E_{\text{TC bulk}}^{*(S)}$	2.50	2.90	4.04	3.60	2.32...2.38 <sup>c</sup>
$E_{\text{TC bulk}}^{*(T)}$	1.26	1.24	1.27	1.30	1.25 <sup>c</sup>

**Table 4:** Si and Tc excitation energies (in eV) calculated using  $\Delta$ -scf and c-DFT with different functionals in comparison to experimental data from Refs. 152<sup>a</sup>, 153<sup>b</sup>, and 154<sup>c</sup>. Here  $E^{\Delta}$ ,  $E^{*(T)}$ , and  $E^{*(S)}$  denote band gap or HOMO-LUMO separation, triplet and corresponding excited singlet exciton, respectively.

several hybrid functionals in the same cell, which are confined to a spacial region of the crystal. For this work the PBE0 and “several functionals“ approach are discarded. With HSE and B3LYP available there are more sophisticated functionals than PBE0 for each surface, and the option to use several functionals at the same time is not supported in the used release of QUANTUM ESPRESSO (6.3).<sup>[33,34]</sup> The remaining HSE and B3LYP serve as limits for both surfaces. As an intermediate functional the HSE functional with 40 % exact exchange is considered. With this value the HSE functional reproduces the B3LYP band gap of a single TC molecule. Therefore, the (static) calculations are done with the PBE functional (relaxation), the HSE functional with 25 % exact exchange, the HSE functional with 40 % exact exchange and the B3LYP functional with 20 % exact exchange. The main focus in this thesis will be the PBE and HSE-25 functional. The PBE functional is the only one computationally efficient enough to allow for molecular dynamic calculations. From the other functionals HSE-25 is the most numerically stable one and it predicts both the fundamental silicon band gap and the singlet fission process (the energy of the triplet being half the energy of the singlet) accurately, as shown in table 4. From this argument one might conclude that the other functionals could be omitted completely. The singlet fission process is, however, strictly speaking not a necessary requirement for the modelling of the interface, as it occurs within the TC bulk crystal (for which the values in table 4 are calculated, crystal structure parameters taken from Ref. 151). The properties of the triplet within the TC crystal and at the TC surface do not necessarily have to be the same.

Additionally, it is possible that there is a singlet/triplet configuration for which the other functionals fulfil the fission condition. For the system to be in a singlet or triplet state, only the total spin has to be zero or one respectively. The exact configuration of the excitation is not set in stone. In this work three singlet configurations were tested, the lowest possible one with a HOMO  $\rightarrow$  LUMO excitation in one spin channel (designated S1<sub>s</sub>), one with this excitation in both spin channels (designated S1<sub>d</sub>), and one with empty HOMO and half filled LUMO and LUMO+1 bands in one channel, designated S1.5 (the more realistic HOMO  $\rightarrow$  LUMO+2 excitation could not be calculated because of consecutive band swapping due to the band lowering of the excited state). For the triplet two configurations were considered, one with one triplet excited in the lowest possible state (designated T1), and one where two triplets are excited (designated T<sub>d</sub>). The excitation energies for those configurations are shown in table 5. From these configurations the S1<sub>d</sub> and T<sub>d</sub> configurations fit best both the fission condition as well as the experimental values, as already shown in table 4 (the T<sub>d</sub> energy is halved in this table, as there are two triplets in the system). Besides the energies there are other reasons to choose these two configurations. On one hand, the configurations preserve the amount of excited electrons, in both cases

	HSE-25	PBE	HSE-40	B3LYP
T1	1.22	1.15	1.25	1.25
T <sub>d</sub>	2.52	2.48	2.53	2.6
S1	1.74	1.39	1.97	1.74
S1 <sub>d</sub>	2.50	2.9	4.04	3.60
S1.5	1.87	1.52	2.10	1.97

**Table 5:** Singlet and triplet excitation energies (in eV) in the bulk TC crystal for different functionals and excitation configurations. The HSE-25 T<sub>d</sub> and S1<sub>d</sub> configurations fit the singlet fission process best.

two electrons are excited. On the other hand, the S1<sub>d</sub> exciton stretches from one molecule to the other, which makes the splitting into two coupled triplets plausible.<sup>[155]</sup> By contrast to this, the S1 excitation is localized mainly on one molecule, discouraging such splitting. The S1.5 electron is completely delocalized, while the hole remains on one molecule, but this is mostly due to the technical limitation of half filled orbitals. The corresponding densities can be seen in figure 22.

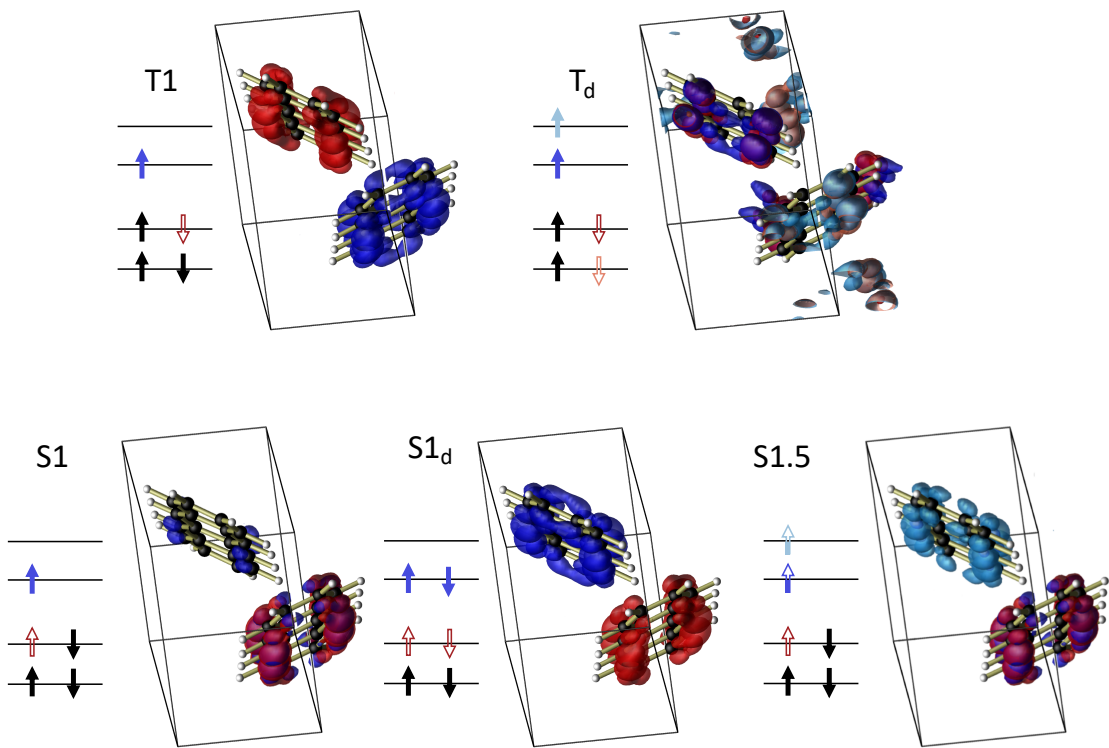


**Figure 22:** Electron (blue) and hole (red) densities for the considered excitation in the TC bulk crystal. Different shades in red and blue designate different bands. Arrows indicate the excitation configuration and correspond to the densities.

While the choice therefore is plausible, it has to be noted that the T<sub>d</sub> configuration results in a total spin of 2, contrary to the situation of the singlet fission, where two triplets with a net spin of 0 occurs. Furthermore, only a non distorted unit cell with only two molecules has been considered. The findings are therefore by no means conclusive. Together with the already mentioned fact that the singlet fission is not necessarily a good criterion to choose a

functional, the band structure and density of state calculations in the following paragraphs are also calculated using the other functionals. However, for the sake of brevity only the HSE-25 results will be shown, and differences using other functionals only mentioned where it applies.

### 5.2.3. Band alignment

To gain a first insight in the system, the partial density of states (PDOS) of the ground state is considered. By projecting the Kohn-Sham wave functions onto the atomic orbitals attributed to the atoms of the Si and TC surface respectively, one is able to identify the states corresponding to each surface. The associated partial densities show the band gaps of the materials and their relative positioning. To gain further insight in which material adjusts to which, the average electrostatic potential is used as a reference. As the lowest Si-bilayer is fixed at the bulk positions, it can be assumed that the lower layers also show the same electrostatic potential as bulk Si. The electrostatic potential averaged in the x-y plane for the interface as well of bulk Si is shown in figure 23, confirming this assumption. In order to avoid effects from the H termination, the average electrostatic potential of the second lowest Si bilayer is computed and set equal to the bulk Si average electrostatic potential. In a last step, the zero point of the energy axis is chosen to be at the maximum of the highest bulk Si valence band. The resulting graph for the high density phase is shown in figure 24 a), where orange lines correspond to Si states and black lines to TC states. Considering only the Si states first, the band gap starts as in the case for bulk Si around 0 eV. The band gap is around 1.3 eV, which is around 0.1 eV larger than for bulk Si. Since the structure is only relaxed using the PBE functional such a discrepancy is to be expected. For the TC states the band gap appears between 1.5 eV and 2.3 eV. For crystalline TC there are no comparable experimental results, but as this band gap is similar to the theoretical results of Ref. 156, the gap is assumed to be described adequately.

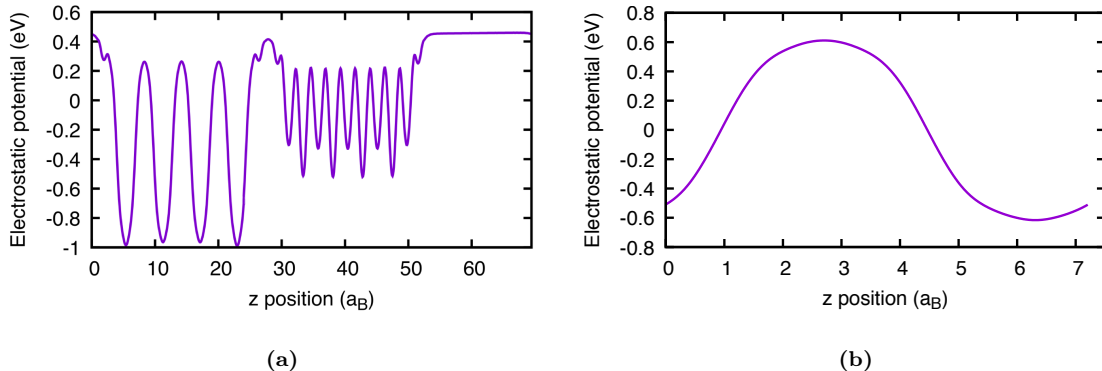


**Figure 23:** Averaged electrostatic potential over the x-y plane for the Si-TC interface (lhs) and a Si unit cell (rhs). The amplitude and frequency of the first four Si layers match their counterpart in the Si unit cell, making the average electrostatic potential a fitting reference for the KS energy levels.

The filled areas in figure 24 a) represents occupied states, i.e. states below the Fermi energy. Therefore, the TC states fill the band gap of the Si states, and since the TC gap resides higher than the Fermi energy almost no band gap can be observed, the system barely has a type II (staggered) alignment.<sup>[157]</sup> Changing the functional changes some details; however, not the implications of the situation. The PBE functional closes the band gap more and even shows an energetic overlap between the TC and Si states at the Fermi energy, creating

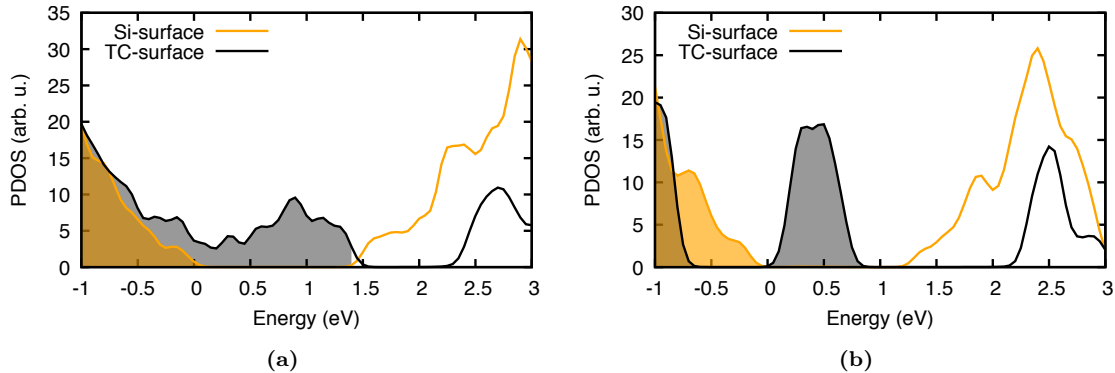


**Figure 24:** Partial densities of states for the ground state of the high density (lhs) and low density phase (rhs) computed with the HSE-25 functional. Orange and black correspond to Si and Tc related states, occupied states (below the Fermi energy) are shaded. The 0 of the energy axis is at the position of the highest Si bulk state. The low density PDOS shows a clear band gap. The high density phase has a diminishing but existing band gap, the small Si-TC overlap at the Fermi energy is only a result of the Gaussian broadening used in the PDOS calculation.

a type III (broken band gap) alignment. The B3LYP functional shows a small band gap, the form and alignment of the bands, however, remain the same. A similar situation occurs in the LD phase as shown in figure 24 b). In the LD phase the TC states are less broadened and the TC band gap is wider. The TC states reside at the Fermi energy, afterwards a small gap follows. This situation does not change regardless of the used functional, with the same widening and narrowing tendencies of the functionals as for the high density phase.

With this system having a smooth transition from the TC states to the Si states it seems to be quasi metallic and one would expect a TC electron to be lifted into a Si state upon an excitation. This is contrary to the observations, as a mixed exciton would require a transfer of the electron between both surfaces. And indeed by introducing a triplet excitation to the system using c-DFT (with an overall positive spin), the exciton is localized fully at the TC surface. So what happens during the excitation? In a simple picture with only one material one would expect a lowering of the now filled state in the conduction band and a rising of the now empty state in the valence band. However, as two materials are involved, the band alignment has to be taken into account. This is shown in figure 25, where the partial density for the excited high density phase is shown spin resolved (spin up positive densities, spin down negative densities). The whole TC density shifts to lower energies in respect to the Si states, where the local TC state density maximum at approximately 0.9 eV in the ground state (figure 24 lhs) now is at 0 eV. The before mentioned effects happen additionally, a state which was formerly in the conduction band is occupied and lowered in energy in the spin up channel, resulting in the peak at 1.3 eV. A state formerly in the valence band is depleted and rises in energy in the spin down channel, resulting in the peak at 0.7 eV. Due to the alignment shift now both the electron and hole are located firmly at the TC surface. Again a similar result is obtained for the LD phase and different functionals do not change the situation fundamentally.

To further substantiate this finding, the opposite fringe case of the HD phase, namely a single flat lying TC molecule at the Si surface was considered. Furthermore, the HD and LD geometries were distorted by calculating one MD trajectory for each phase at 300 K for 2 ps. In none of these calculations a transfer of the triplet to the Si-surface could be observed, in case of the MDs only a delocalization over several molecules could be seen.

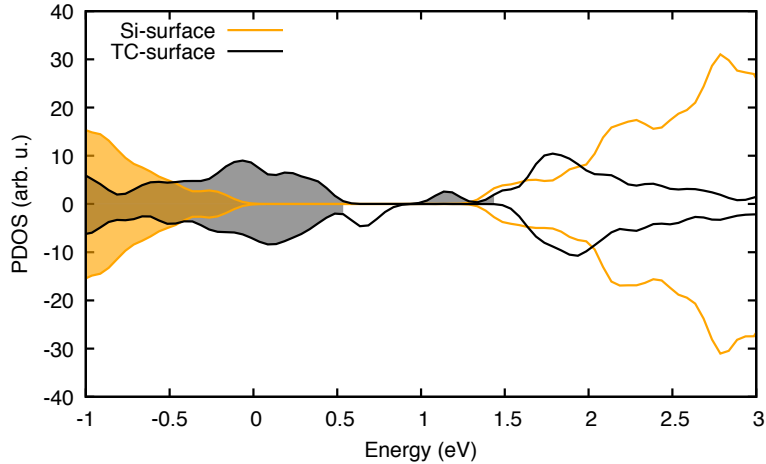


**Figure 25:** Partial density of states for a vertical triplet excitation at the ground state structure of the HD model. Negative and positive PDOS correspond to the spin up and spin down channel, the dashed lines correspond to the Fermi energies. In respect to figure 24 the TC states are moved to lower energies. Directly below the spin up Fermi level and above the spin down Fermi level are two TC peaks which do not occur in the ground state. Those respectively occupied and unoccupied states correspond to a TC localized electron and hole, thus a TC localized triplet exciton.

This clearly shows that a exciton transfer is not to be expected at the ideal interface. However, this study also shows that the band alignment for this interface is quite sensible. By manipulating how the bands align, an exciton transfer might be possible.

### 5.3. Introducing the defect

One possibility to do so might be to introduce a defect to the passivating hydrogen layer (towards the interface). There are two reasons why introducing a defect could be useful. On one hand, defects at interfaces are known to be able to pin the Fermi level close to them, i.e. at the charge neutrality state, which is the energetic position of the half filled defect.<sup>[158]</sup> Pinning the Fermi level should reduce the flexibility of the band alignment, as the TC states above the TC band gap should be empty, and states below should be filled. On the other hand, introducing a defect leads to open bonds at the surface. These open bonds serve as a predestined place for the electron or hole of the exciton to localize onto.

In this case one H ion is removed from the passivation layer, leading to a negatively charged Si surface and a doubly occupied dangling bond (db) at the defect. The removal of one positive charge carrier makes the exciton hole a suitable object to compensate the dangling bond. The electrostatic interaction between electron and hole of the exciton can afterwards pull the electron to the Si-surface, completing the exciton transfer.

In a first step we again look at the partial density of the ground state, displayed in figure 26 for the high density phase. In comparison with the ground state density without defect (figure 24 a) ), several things should be noted. First, the Si states do not move, the valence band maximum is still located at the bulk Si maximum (0 eV), the band gap is also still the same. Additionally to the surface and bulk Si states, the defect state resides at 0.15 eV, therefore in the Si band gap. The Fermi energy is moved substantially towards the defect, and the TC states move with the Fermi energy. This results in an overlap between the band gaps, wherefore the interface appears to be insulating. With the shift of the Fermi

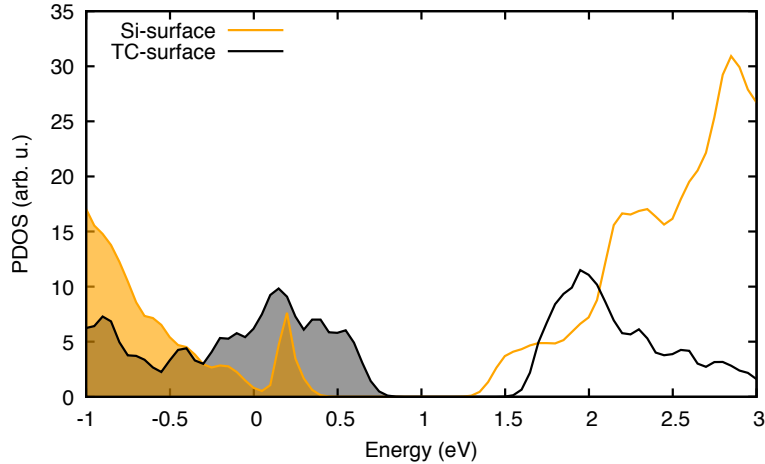


**Figure 26:** PDOS of the ground state of the HD phase with dangling bond. The dangling bond state occurs directly above the Si valence band. The Fermi energy is fixed close to the dangling bond, resulting in a shift of the TC states and creating a band gap.

energy the Si valence band state and especially the defect state are far more probable to be affected by the excitation, a necessary step for the hole transfer. Nevertheless, an excitation from the valence band maximum to valence band minimum appears to lead to an half TC, half Si bound exciton, like in the case without defect.

To verify this assumption, by keeping the structure the same and introducing the triplet one is able to calculate the DOS of the excited system which is shown in figure 27. However, this figure paints a different picture: While the band alignment has indeed not changed, the exciton is purely localized at the TC. To understand why this occurs we have a more differentiated look at the states of the ground state by means of the band structure. This band structure is shown in figure 28. One can see that the Si states dominate the conduction band minimum at  $\Gamma$ ; however, there are also contributions to the lowest band from TC states near  $X$ . By exciting the electron one empties the highest valence band which is purely TC attributed. The lowest conduction band which is mostly Si but partly TC attributed is filled. These bands interact via electron-hole Coulomb interaction which each other. Since the Coulomb interaction is dependent on the distance between the charges, the TC-TC interaction is stronger than the TC-Si interaction. This causes the TC states at the edge of the band structure to be lowered more than the Si states. While they do so they “pull” the mid band TC states with them and form a fully TC localized state, and therefore an exciton localized completely at the TC surface.

A vertical excitation leads to a TC localized triplet exciton. However, the goal is to use the dangling bond at the defect to capture the exciton hole and therefore initiate the transfer. To gain insight on how the system behaves with a half-filled dangling bond (the situation once the hole is captured) a half filled dangling bond is encouraged by considering not the charged system, but the charge neutral one. Once again the PDOS is utilized for analysis, which is now also spin dependent in the ground state due to the uneven number of electrons in the system. The result is plotted in figure 29. As expected, the spin down part of the dangling bond rises in energy. Interestingly two peaks can be observed, one directly at the Fermi energy (the charge neutrality state), which is partially filled, and a completely empty one, which rises towards the conduction band. This is observed for each functional but PBE, where the dangling bond localizes completely at the Fermi energy.

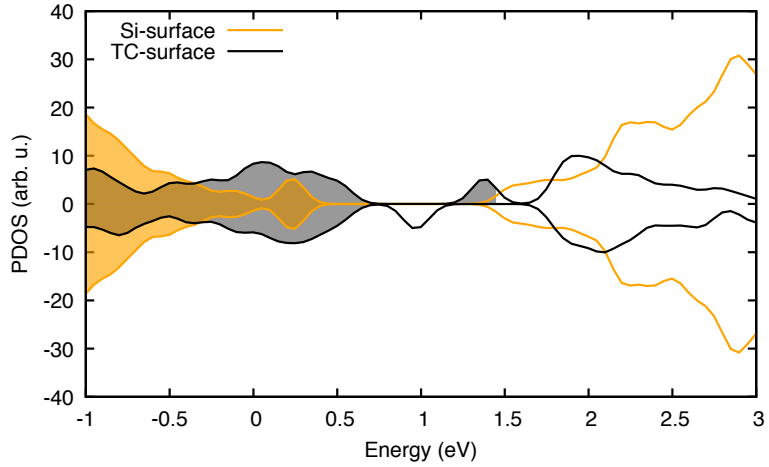


**Figure 27:** PDOS as in figure 26 but with added triplet excitation. As before a TC localized triplet is observed.

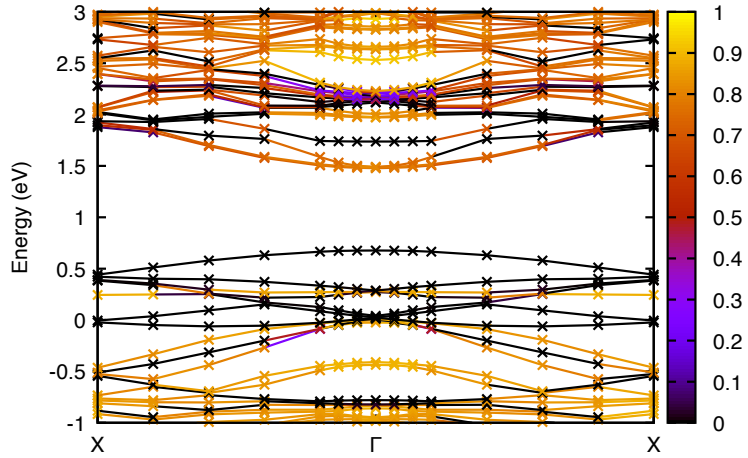


**Figure 28:** Band structure corresponding to the PDOS of figure 26. The highest valence band is completely of TC character, the lowest conduction band has Si localized states at  $\Gamma$  and TC localized states at  $X$ . As the Coulomb interaction between TC and TC states is higher than between TC and Si states an excitation results in the TC localized triplet in figure 27.

It is notable that the energetic change for the dangling bond is accompanied by a lowering of the dangling bond Si atom, it assumes a position closer to its original one without defect. This rises the question if the energetic position of the dangling bond in the charged state can be manipulated by moving the dangling bond atom. And indeed by shifting the defect to the Si surface and shaking up the rest of the structure, the structure relaxation leads to a half occupied dangling bond state. Together with the fully relaxed TC bound triplet structure two stable structures are obtained, which are shown in figure 30. It can be seen that for the half-filled dangling bond the lowest conduction band now is a Si band, in accordance with our earlier findings on the lowest conduction band being determined by the unoccupied hole state. The triplet therefore is fully located at the Si surface. In the following these structures will be referred to as  $\text{Si-TC}_{\text{TC}*}$  for the TC bound triplet structure and  $\text{Si-TC}_{\text{Si}*}$  for the Si bound triplet structure. These two structures are stable for every functional; however, there is a notable difference concerning the energetics. For each functional except B3LYP the  $\text{Si-TC}_{\text{Si}*}$  is energetically favourable, with HSE for

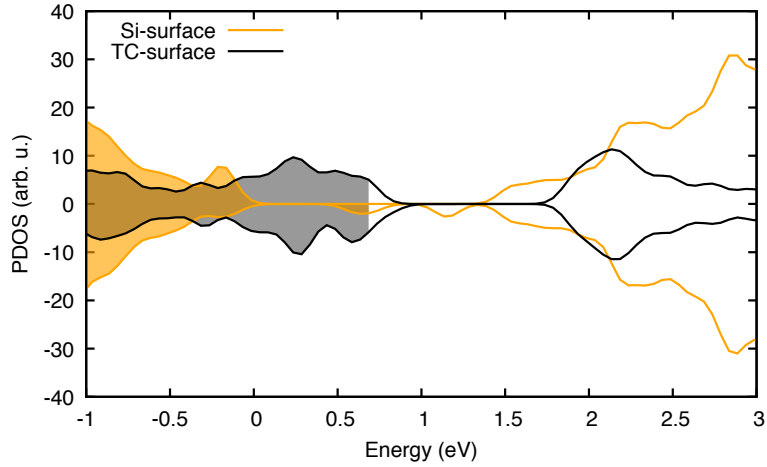


**Figure 29:** PDOS of the uncharged dangling bond HD structure. The dangling bond is therefore half-filled. As to be expected the occupied part moves into the bulk Si states, while the unoccupied part moves to the charge neutrality state. Interestingly another completely empty db state also arises above the Fermi energy.

example there is a difference of 130 meV between those structures. For B3LYP the Si- $\text{TC}_{\text{TC}^*}$  structure is favourable with a difference of 83 meV.

While for the functionals there is no qualitative change, changing to the LD model does change the situation. The TC states experience roughly the same shift as in the high density case, they are also on top of the bulk Si states. However, since the states are less broadened, the dangling bond Si state is now above the TC states and is the highest valence band as seen in figure 31 a). The alignment in the conduction bands does not change substantially in comparison to the HD case. Therefore, the lowest conduction band is a Si state with edge contributions from TC. Similar to the discussion above, by exciting a triplet the Si conduction and valence band states are lowered and raised due to the electrostatic interaction being mainly between Si states, whichfore the triplet is located at the Si. This is shown in figure 31 b). With other words, an excitation from the ground state and following relaxation leads directly to a triplet located at the Si surface. In fact, finding a stable configuration in which the triplet is located at the TC monolayer proves

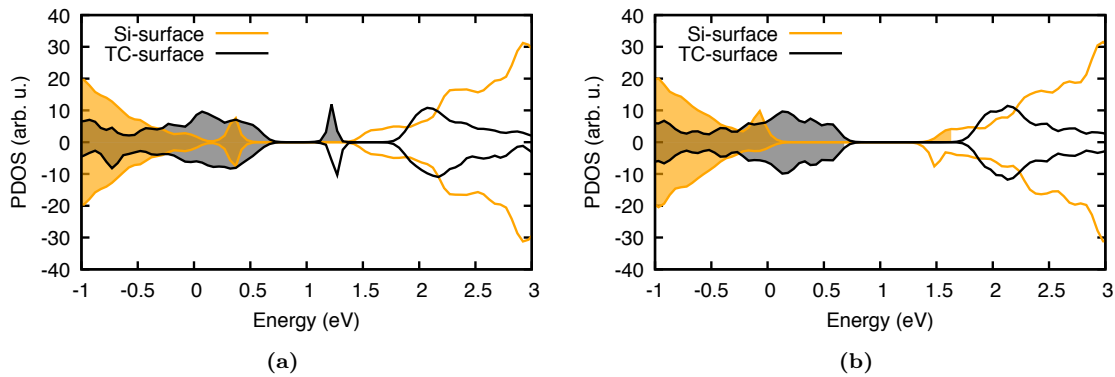


**Figure 30:** PDOS of the HD phase with dangling bond at the TC localized triplet structure (Si- $\text{TC}_{\text{TC}^*}$ , lhs) and the Si localized triplet structure (Si- $\text{TC}_{\text{Si}^*}$ , rhs). Geometrically those structures differ mainly on the z-position of the dangling bond atom, with the atom being higher in the Si- $\text{TC}_{\text{TC}^*}$  structure and lower in the Si- $\text{TC}_{\text{Si}^*}$  structure.

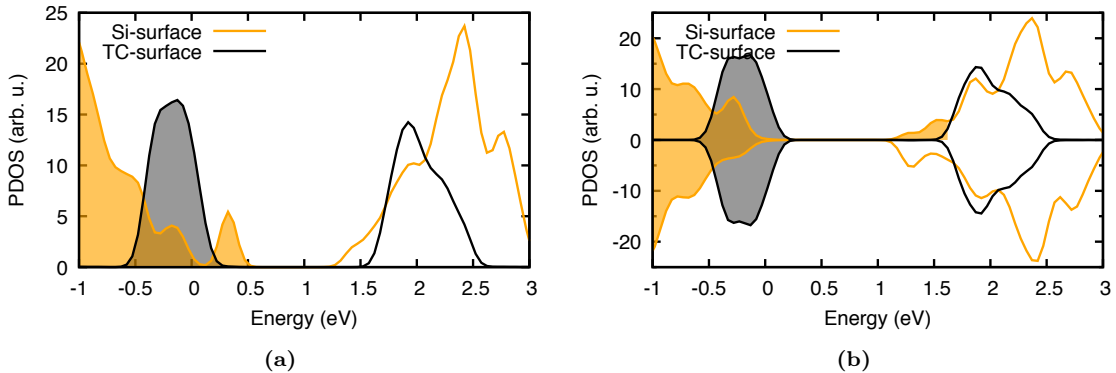


**Figure 31:** PDOS for the LD model with dangling bond in the ground state (lhs) and with excited triplet (rhs). Due to the smaller TC dispersion the dangling bond state is the highest occupied valence band state, while the lowest unoccupied conduction band is also dominated by Si states. This results in a direct excitation of a Si localized triplet, TC localized triplets are unstable in this model.

impossible without external force. Only by either constraining the dangling bond Si atom position to be outside the Si surface or by applying a Hubbard U correction of 12 eV to a single TC molecule a localization at the TC surface can be forced. Due to the non-existent stability of the TC located triplet in the LD model, it will be left out of the later presented MDs and barriers. It has, however, to be kept in mind, since a LD like structure is most likely to be present directly at the interface.<sup>[130]</sup> All calculated times and barriers are therefore upper limits for the TC monolayer.

To summarize at a spatial view, the Si-TC<sub>TC\*</sub> and Si-TC<sub>Si\*</sub> structures differ mainly by the dangling bond position, a db out of the Si surface for the TC bound triplet state, and one inside the Si surface for the Si-TC<sub>Si\*</sub> structure. From an energetic point of view the dangling bond Si state is either below or above the TC valence bands. In order to transform one structure into the other one has to raise/lower the dangling bond in energy and vice versa in space. If, how and why this happens will be probed in the next chapter by means of molecular dynamics.

## 5.4. Dynamics

Starting from the Si-TC<sub>TC\*</sub> structure, a MD using the PBE functional and the Berendsen thermostat is conducted at 300 K. For MD calculations the hybrid functionals will be excluded, as they consume too much computation time. The integration time step for the equation of motion is chosen as 1 fs, the time constant for the thermostat as 15 fs. The resulting trajectory is first analysed by means of the electronic density of the electron and hole state as shown in figure 32. At the starting point both electron and hole are localized at a single TC molecule. As the system becomes disturbed by the thermostat, electron and hole delocalize over the whole TC monolayer. This situation does not change for a while, until around 310 fs the hole localizes at the dangling bond. The electron follows around 330 fs. That confirms the assumption made at the beginning of the last chapter: The hole localizes first at the dangling bond and pulls the electron afterwards to the Si surface via electrostatic interaction. To gain further insight we have a look at the spacial and energetic behaviour of the dangling bond. In figure 33 the four highest valence band KS states for the spin down channel in a single  $k$ -point, the lowest conduction band state for the corresponding spin up  $k$ -point, and the dangling bond z position are shown. As the

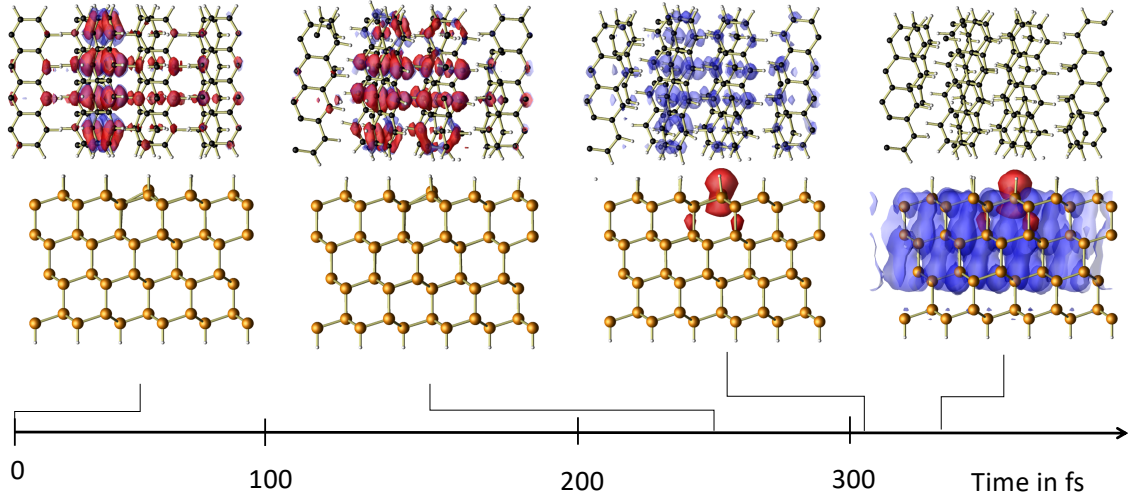


**Figure 32:** Charge densities of the triplet during an exemplary trajectory starting at the  $\text{Si-TC}_{\text{TC}^*}$  structure. The triplet delocalizes over the TC surface, until the hole hops to the dangling bond. The electron follows in a matter of fs due to electrostatic interaction.

system has a triplet configuration the highest valence band is empty, it is the hole state. The dangling bond state – at  $t=0$  the third highest valence band state – is marked red. The vertical dashed lines correspond to the times in figure 32.

Directly apparent is the relation between the dangling bond energy and the dangling bond position. Raising the dangling bond in  $z$  direction causes the KS energy to drop and vice versa. This can be understood by means of the hybridization of the dangling bond state. Raising the dangling bond spatially causes the Si-Si bonds with the surface Si atoms to be inclined. With the three bonds to the surface inclined (and the dangling bond facing outside the surface) the corresponding hybridization is of the  $\text{sp}^3$  type. If the dangling bond is lowered, the db Si atom is planar with the Si surface, there is no inclination towards it. With three planar bonds and the upright standing dangling bond the appropriate hybridization is of the  $\text{sp}^2+\text{p}$  type. This can also be seen in the density of the db state, shown in the insets in figure 33. The  $\text{sp}^3$  like hybridization (left density) has three “bulbs” at the surface Si atoms (only two can be seen due to perspective), and an upward shifted density connecting them. Additionally, there is the relatively large dangling bond as well as a small bulb atop of it which stems from a rest hybridization with another band which it recently crossed. The  $\text{sp}^2+\text{p}$  density has a larger connecting bulb which is at the same height as the surface Si densities. The importance of this re-hybridization is that the  $\text{sp}^3$  hybridization is energetically favourable over the  $\text{sp}^2+\text{p}$  one. Therefore, the energy of the state has to rise when the atom is pushed to the surface – which complies with the findings of the MD.

During the course of the MD the db state rises upwards and downwards and crosses other bands in the process as discussed above. In most of the cases this is not critical, as all those states are occupied. A more problematic crossing is the crossing between the db state and the highest valence band, which is empty due to the excitation. Numerically the occupations stay fixed during the course of the MD, once the crossing occurs the db state is immediately emptied and the other state filled, giving rise to the hole localization at the dangling bond. Physically there is no direct reason for the electron to swap states

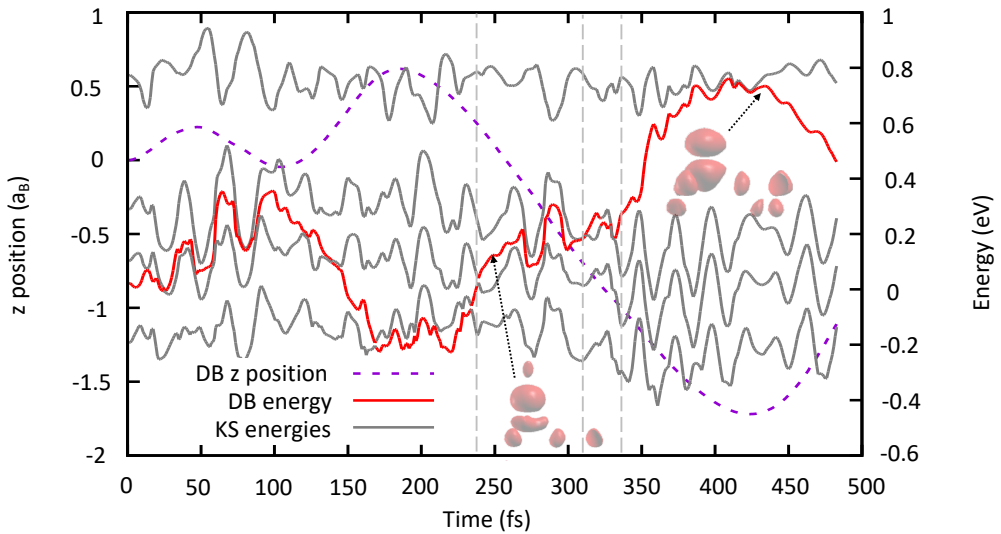


**Figure 33:** Dangling bond z position and KS energies at one  $k$ -point for the trajectory as in figure 32. The KS state corresponding to the dangling bond is marked red. Insets show the charge density of the dangling bond state. Dashed lines correspond to the snapshot times in figure 32. A clear dependency of the db energy and position can be observed. Lowering the dangling bond position further causes a rehybridization of the dangling bond state.

immediately, an according hopping probability has to be calculated. The hopping including level crossings is a bit more complicated than the one used in chapter 2.7 and will be explained in the next chapter.

#### 5.4.1. Surface hopping at interfaces and with level crossings

A general problem of the presented LIBRA-X hopping program is that while one is able to monitor the occupation of specific excited states, one is not able to track the character of the state. In chapter 3.3 there was the case of a first excited state  $S_1$  being temporarily energetically higher than the second excited state  $S_2$  due to different smearing. In this case the states keep their character, and one is able to switch them back after the whole trajectory is computed. Lets now consider the level crossing as in figure 33. At 300 fs the highest occupied state in the spin down channel is the dangling bond state, the lowest unoccupied state is a TC state. Therefore, the “ground state”  $S_0$  corresponds to an occupied db, while the first excited state  $S_1$  corresponds to an unoccupied db. After the level crossing the “ground state” corresponds to an unoccupied db, while the first excited state corresponds to an occupied db. Hence the  $S_0$  and  $S_1$  states change their character. In reality, if no hopping between states occur the dangling bond will stay occupied, and therefore the system changes into its excited state after the level crossing. Since the hopping probability is not only dependent on the wave function overlap but also the current (Schrödinger) occupation number, and since the change is not for one or a few steps but for several 100 fs, it is important to swap the occupation numbers *in situ*. Hence the level crossing has to be detected and the occupation numbers swapped accordingly. However, the program only has memory of the current and next wave functions. Furthermore, the states tend to hybridize at least partially during a crossing. This makes it difficult to impossible to properly register the level crossing.

Due to this problem another approach is chosen: For five prototypical MDs (the one in

figure 33 and four from the 300 K set in section 5.4.2) the ground state trajectory is taken as fixed, and for a time span of roughly 100 fs around the level crossing (250-360 fs in our example) the total energies,  $k$  dependent wave functions and overlaps are calculated. With these fixed values equation 2.35 is solved. While solving the equation, the occupation numbers are swapped at the level crossing (around 340 fs in the example). Using this procedure the occupation numbers for the trajectories are calculated. Due to the necessity to recalculate each trajectory and manually identifying the level crossing, this calculation is only performed for a small number of prototypical MDs. While this is by no means a statistical relevant sample it gives an estimate for the order of the probability. We observe a strong variation of the hopping probability which reaches from as low as 0.1 % to as high as 80 %, which do not only differ for each trajectory, but also for each  $k$ -point within the trajectory. This can again be traced back to (partial) hybridization; however, this time not of atomic states but of Kohn-Sham states. If two states become energetically degenerate they can hybridize, and form two new states which are linear combinations of both original states.<sup>[159]</sup> Being constructed by a linear combination, the new states have an overlap with both original states. If only one of the original states is occupied, the electron can choose freely between both new states in case of perfect hybridization. In fact, a perfectly hybridized state consisting of two states of which one is occupied should ideally be described with a half occupation of both original states within DFT. With other words, if a hybridization occurs during the level crossing for a prolonged time, a high probability of the electron to hop is detected. This reflects in the energetic positions of the states. The db state and the highest valence band state in figure 34 (top) only approach each other for short intervals, and the final crossing happens quickly. Therefore, there is little time for hybridization and a hopping probability of 0.1 % is detected. However, if a trajectory like in figure 34 (bottom) is considered, both states nearly degenerate for a prolonged time, resulting in a hopping probability of 70 %.

With such a variation of hopping probability, can there be a general statement for the transition? For the trajectories with high hopping probability there is little change, as the electron will most likely hop to the lowest triplet state and thus follow the trajectory already calculated. The trajectories with little hopping probability will behave different: If no hopping occurs the dynamic should be governed by the excited state instead. Figure 35 shows what happens if this is considered: Starting from a configuration directly after the level crossing from figure 33 the trajectory is calculated. The excited state nearly immediately slows the lowering of the dangling bond atom, leading to a re-approaching of the two states. At 55 fs and 75 fs there are even two possible switches of the db and the TC state. As already established, the trajectory would switch back to its ground state if no hopping is considered, a circumstance which does not occur as the KS state occupations are fixed during a trajectory. With the two KS states again approaching each other, the hopping probability again increases, as the overlap increases due to increasing hybridization as explained earlier. The calculated 5 % hopping probability for this trajectory are therefore rather a too low estimate then a too high one. Considering the transition times presented in a later chapter, the hopping of the electrons is most likely neglectable.

It is to note that in contrast to the case of lithium niobate we get finite hopping probabilities. The conditions seem similar, both cases consider a defect and both cases consist of crystal structures. So why do we get a hopping probability of 0 in one case, while the other one is finite? This difference has two reasons: First, lithium niobate is a three dimensional crystal. The TC film consists of single molecules which are loosely bound via van-der-Waals interaction into a crystal lattice. Therefore, the TC states are more molecule like

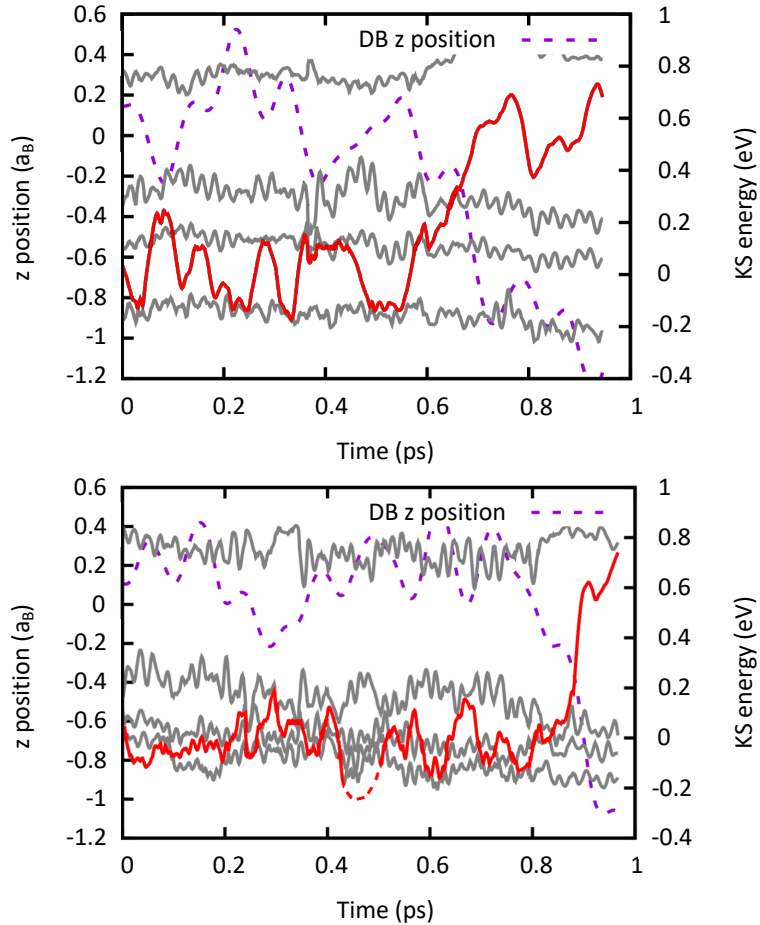


**Figure 34:** Graphs analogue to figure 33 for two other trajectories. The upper one exhibits a sharp crossing between the db and highest TC state at 675 fs, which results in a small overlap and hopping probabilities of 0.1 %. The lower one exhibits a prolonged approach of the two states between 800 fs and 900 fs, resulting in a high hopping probability of 70 %.

than crystal like. The defect state is additionally strongly localized and therefore also has some characteristics of a molecule. Generally it appears that surface hopping is more prevalent at highly localized states, which makes sense as the wave functions of those states are usually highly dependent on the motion of the atoms/molecules at which the density is localized and therefore are subject to quick changes. Besides the oxirane molecule, where this effect can be seen easily by the change of the densities for small geometry variations, the effect can be also seen in different systems, like the reconstructed InP surface for example. The InP surface exhibits occupied and unoccupied surface states which are localized at reconstructed P dimers. The movement of those dimers leads to a finite hopping probability between those states, which is reduced if the motion of those dimers is restricted.<sup>[160]</sup> The second reason for finite hopping probabilities is the fact, that the defect state is occupied in the beginning in the case of the interface, the resulting nearly dispersion-free state (which also goes in hand with the strong localization) can be clearly seen in the DOS. In case of lithium niobate the electron starts delocalized and the state has yet to form. Therefore, the problems with the dispersion mentioned in chapter 4.9 occur fully in lithium niobate, while they are not so prevalent in the interface, wherefore the surface hopping algorithm can be used for the interface and not for lithium niobate.

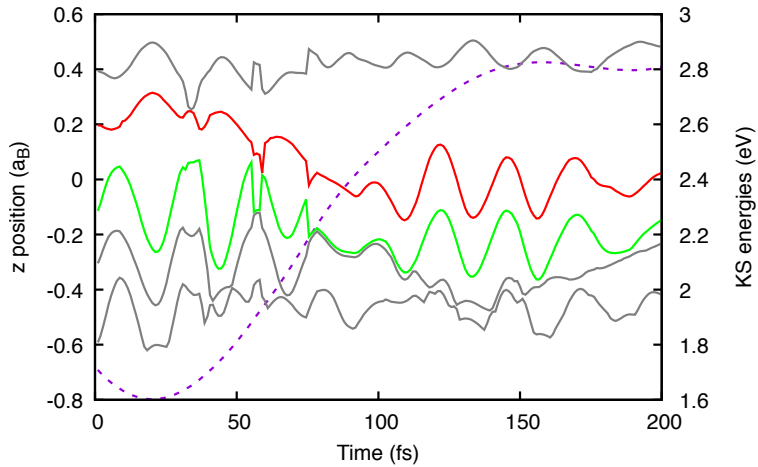


**Figure 35:** c-DFT Molecular dynamic starting at 330 fs of the trajectory in figure 33, i.e. directly after the level crossing. In this MD the dangling bond state (red) is kept occupied and the crossed TC state (green) is still empty. This inverted occupation causes an immediate deceleration of the dangling bond atom, which inverts the movement and pushes the atom upwards. The two states reapproach each other instead of diverging like in figure 33. This reapproaching again increases the hopping probability.

#### 5.4.2. Transfer times

With the transfer mechanism explained it remains to be seen on what time scales this transfer occurs. In order to gain this information one would have to calculate a multitude of trajectories like in the case for the other two systems. That can only be done for the PBE functional, as molecular dynamics with hybrid functionals are computationally not feasible. However, since one of the prominent changes in comparison to the hybrid functionals is the energetic position of the db, it is to be expected that the transfer is impeded if hybrid functionals are utilized. One possibility to compare the functionals is to calculate the activation energy, in explicit the energy barrier for the exciton transfer. One standard method to calculate such a barrier is the nudged elastic band (NEB) calculation.

In a NEB calculation two structural configurations, which should both be in a (local) energetic minimum, are connected with intermediate structures, which are usually constructed via linear interpolation between the two initial states. These intermediate structures are allowed to relax, but under a constraint: The forces acting on the atoms which are tangential to the path defined by the images are replaced by harmonic spring forces, which keep the spacing between the images constant. The forces perpendicular to the path are not affected. With these constraints one can determine the lowest energy reaction path. For more information on NEB calculations the interested reader may refer to Refs. 161, 162.

Applying this technique to the  $\text{Si-TC}_{\text{TC}^*} \rightarrow \text{Si-TC}_{\text{Si}^*}$  transfer one gains barriers as shown in figure 36 a). The procedure seems to work reasonable for the PBE functional; however, for the HSE functional there is little resolution in the area of the barrier. This problem can be reduced by either increasing the spring forces and thus driving the images up the barrier, or by recalculating this subset of the barrier by setting the start and end structures close to the barrier. Both methods however suffer similar problems: A strong undershooting of the established points after the barrier and/or an unrealistic high barrier of several 100 meV – since there is no stable  $\text{Si-TC}_{\text{TC}^*}$  configuration in the LD case, and thus no barrier, a high barrier for the upright standing TC molecules seems unreasonable. The NEB algorithm apparently is not able to predict the barrier for this transfer.

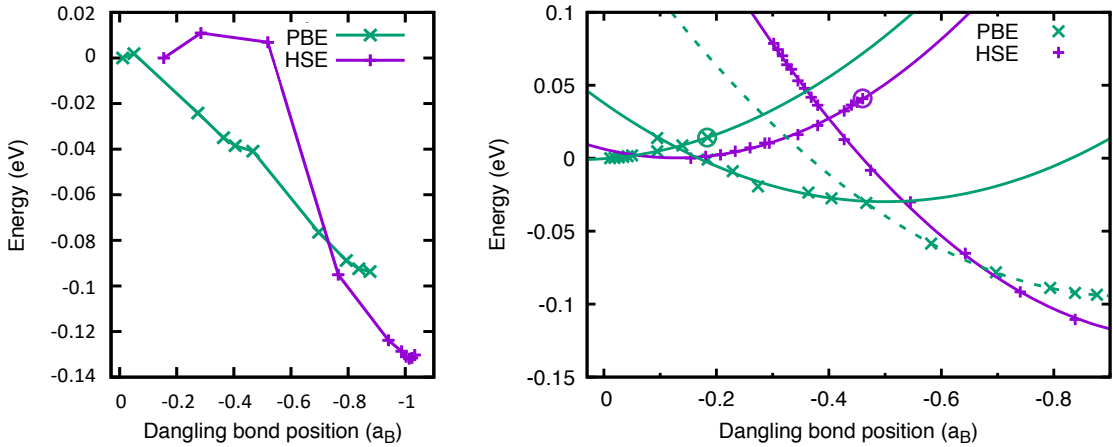


**Figure 36:** Transition barriers calculated via NEB (lhs) and linear interpolating the dangling bond position while relaxing the rest of the structure (rhs). Circles show the last stable point for the PESs. The NEB calculation show a bad resolution around the barrier, making it not suitable for estimating the barrier. The linear interpolation shows two distinct PESs for the HSE functional corresponding to the triplet location. The crossing point of those PESs gives an estimate for the Barrier. The PBE functional shows 3 PESs, which is due to the localization being  $k$ -point dependent for PBE.

The reason for this can be found in the form of the transfer. As already established, the transfer begins to occur as soon the occupied dangling bond Si state in the spin down channel crosses the unoccupied TC state and thus captures the hole. This crossing leads to a sudden change in forces as the new state is occupied. The spring forces on the image closest to the barrier are therefore fundamentally different as they stem from a different PES. This leads to a higher distortion of the structure and thus to higher barrier energies, creating an artificial steep slope. If the spring forces are strong enough, this will also have an effect on the neighbouring images, they are pushed downwards resulting in the undershooting following the barrier. To circumvent this problem a different method has to be chosen which only considers one PES at a time.

Fortunately, the main driving force for the transfer, the dangling bond movement, is already established. This enables the manual driving of the transfer by fixing the dangling bond atom to certain displacements. In a first step 10 intermediate structures are generated by linearly interpolating between the Si-TC<sub>TC\*</sub> and Si-TC<sub>Si\*</sub> structures. Those structures are then relaxed with the position of the dangling bond Si atom being kept constant. By considering the shape of the graph and the electronic densities one identifies the points at which the level crossing has occurred. In order to stay on one PES as long as possible, further intermediate points are generated by starting from the Si-TC<sub>TC\*</sub> or Si-TC<sub>Si\*</sub> structure respectively and only moving the dangling bond atom, and then relaxing those structures with fixed dangling bond. This procedure is repeated until a dangling bond position is identified where the starting PES is no longer viable and the hole hops. The resulting mapping of the PESs is shown in figure 36 b). Due to the construction of these surfaces the correct barrier can not be read from this diagram, however, one gets an estimate. Following the HSE PES from the Si-TC<sub>TC\*</sub> structure, the localization stays stable to a position of  $-0.45 \text{ a}_B$  and a maximal barrier of 44 meV. The intersection of the PESs gives an estimate for a lower boundary for the barrier at 27 meV. Analogous, the maximum for the barrier for PBE is 16 meV and the minimum is 7 meV. This difference in barrier height will have a quantitative influence on the transfer times, but they are both

low enough that thermal activation of the transfer process at room temperature is to be expected. A noticeable difference of the two graphs is the occurrence of a third PES in the PBE curve, indicating a second transfer. A closer look on the electronic densities confirms that indeed two transfers occur, the exciton hops at different dangling bond locations for the two non-equivalent  $k$ -points. For HSE there are only two PESs, the exciton hops at both  $k$ -points at once. This is due to the strengthened localization in hybrid functionals. Interestingly, if one only considers the PBE PESs where the exciton is localized fully at the TC or Si surface at both  $k$ -points, one gets an intersection nearly exactly of the energy of the HSE intersection. That implies that the barrier is mostly dependent on the localization and should be thus reproducible by less computationally expensive methods as DFT+U.

With the functionals compared, the focus can be put on the actual transition times for the PBE functional. The starting procedure is similar to the one used in chapter 4.6: A single MD is conducted from the ground state without excitation using a Berendsen thermostat at 300 K. The trajectory is developed for 1.9 ps. After 1 ps of thermalization starting configurations (positions and velocities) are extracted each 25 fs. These starting configurations are used for MDs with the excited triplet, which then can be analysed for the transfer time. However, while this procedure worked well for lithium niobate, for the Si(111)-TC interface it appears to be problematic: Inspecting trajectories from adjacent time steps reveals clear similarities in the trajectories and transfer times, they are not independent. This can be traced back to the vibration frequencies of the materials: For LN the O cage around the defect Nb has an oscillation period of roughly 70 fs, while the dangling bond oscillates with an oscillation period between 150 fs and 200 fs. This leads to less difference between the starting positions and thus a dependence between them. Furthermore, there is an underlying oscillation of the distance between the surfaces, which has an even lower frequency with a period of 1800 fs. This makes it impossible to access many qualitatively different configurations by extracting starting geometries from the trajectory. Therefore, another approach has to be utilized.

**Starting configurations** In chapter 3.3 the starting configurations were generated by displacing each atom in a uniform random fashion. In chapter 4.6.1 this method is refined by replacing the uniform distribution by a Gauss distribution, which broadness is determined by a fit of an existing trajectory. This worked well for the LN crystal, but applying this method here results in trajectories whose starting temperatures are several 1000 K high. This is due to the amount of components in the present system: The two surfaces on one hand, and the single molecules of the TC layer on the other hand. The intra molecular forces for example are way stronger than the inter molecular forces. Therefore, a molecule can move comparatively easy during a MD, while deforming it is harder, which can lead to an accumulation of “global” displacement for each atom, but none relative to the molecule. With a distribution for each atom independently this information is lost, only the global displacement is seen which leads to strong deformations of the molecules. Since the molecules are rather rigid, this leads to large amounts of potential energy which then quickly translates to high temperatures. In order to solve this problem one has to create distributions for each component in relation to its overarching component. In explicit for the largest component, the TC layer, its mean z position and the mean tilt of the molecules around the axes parallel to the surface are monitored. Relative to the resulting displacements, the position and all rotations of each molecule is monitored. After including those displacements, the deformation of the molecules is taken into account. This is done by considering the largest deformation which is observed during the MD, namely a bend-

ing of the molecule around its lateral axis. The remaining displacement of the atoms is relative to this bended molecule and is also monitored. For the Si surface only the absolute displacements are recorded. This is possible since the position of the Si surface is fixed by its lowest layer in bulk positions and does not contain a subdivision like the TC surface. The values for these parameters are recorded in 50 fs intervals. Using the variance of the parameters, a Maxwell distribution for each parameter is constructed.

With this distribution as a basis, the rotations, curvatures and movements are generated randomly. The direction of the rotations and displacements is decided randomly, with a uniform distribution. The starting configurations created this way lead to starting temperatures closer to the desired 300 K, but are still several 100 K too high. This could be retraced to an remaining overestimation of the displacement between the H-C bonds, as well of a “breathing” motion of the Si surface, meaning an expansion and retraction motion of the atoms perpendicular to the surface. These issues are addressed by removing any further displacement after the bending of the molecules, and scaling the displacements of the Si-atoms inverse proportional to the highest bond length increase. Additionally, for some starting configurations an unrealistic large bending of the molecules is observed. To prevent this, the bending is confined to the maximally reached value in the trajectory by scaling the curvatures accordingly. With these modifications the temperatures using the resulting starting structures are only few 10 K away from the required 300 K. They are therefore a suitable, though simplified estimation for starting configurations. By scaling the broadening of the Maxwell distributions by  $\frac{T_d}{300\text{K}}$ , where  $T_d$  is the target temperature, one is also able to generate starting structures for other temperatures.

As in prior chapters, not only the structure, but also the initial velocities have to be determined in order to generate a starting configuration. As already established, the displacements of the TC atoms are mostly governed by the rotation, displacement and bending of the molecules. The velocities have to behave in a similar way. To guarantee this, the velocities are not determined randomly, but are gained by calculating a trajectory starting from the generated starting configuration with 0 initial velocity and afterwards controlling the temperature using a Berendsen thermostat. After a thermalization time of 400 fs both starting configuration and initial velocities are obtained. This procedure also bears the advantage of going away from the simplified starting configurations and generating well equilibrated ones. This of course requires additional trajectory calculations for the starting configurations. Nevertheless, the random configurations still bear an advantage over starting configurations derived purely from MDs: Due to the fitting starting point of those trajectories the time for thermalization is with 400 fs much shorter than the 1 ps of the trajectory which serves as basis for the distribution. Furthermore, each starting configuration can be calculated in parallel instead of relying on a very long trajectory to extract the configuration. The randomness furthermore guarantees the independence of the trajectories, which is not a given if the same starting positions are used.

**Trajectories and results** With the determined procedure 50 starting configurations are generated for the temperatures of 50 K, 200 K, 300 K, 400 K and 500 K each. Molecular dynamics are conducted using the Berendsen thermostat and evolving the trajectories over 1 ps with an integration time step of 1 fs. It has to be noted that for several of those trajectories, especially at high temperatures, several exciton transfers from TC to Si and vice versa can be observed. From this transfers only the first will be considered for the transition time, since in the application as solar cell the electron would be moved to a contact upon transiting to the silicon. However, the observed back transfer, together with

the fact that the relaxed uncharged cell assumes a “middle state” between the Si- $\text{TC}_{\text{Si}*}$  and Si- $\text{TC}_{\text{TC}*}$  structures both in dangling bond position and PDOS (see also figure 29), shows the reversibility of the process, allowing for consecutive triplet transfers. In order to find out the transition time of this first transfer, the level crossing is utilized. The transfer is considered to have occurred as soon as the level crossing for both  $k$ -points has happened.

Averaging the transition times leads to the results shown in figure 37. There are two findings: First, the transition time gets shorter with increasing temperature. To see this one has not only to consider the mean transition time, which appears for most of the temperatures to be the same, but also the number of trajectories in which the transfer is not observed during the simulation time (which therefore cannot be included in the mean transition time). From 50 K to 200 K this number stays constant, and the mean transition time declines. At the step from 200 K to 300 K the mean transition time is higher, but the number of trajectories without transition declines. Afterwards an overall decline of both mean transition time and number of trajectories without transfer occurs, except for 500 K where a small increase is observed. This trend indicates an overall reduction of transition time with increasing temperature. That result is to be expected, a process which requires an activation energy is generally more likely to occur at higher temperature. It has to be noted that the results for 500 K have to be considered carefully, as in few cases the TC layer is heavily deformed (for example a single molecule being shifted out of the layer so that one C ring is exposed), in one case one TC molecule even lost two H atoms. Those cases usually lead to late or no transfers, shifting the mean transition time and the number of trajectories without transition upwards, where further decline would be expected.

The second finding is the broad scatter of transition times as seen by their standard deviation. There are several reasons for this. First, there is the oscillation period of roughly 200 fs of the dangling bond. Assuming the conditions are sufficient, i.e. the dangling bond atom has enough kinetic energy to surpass the barrier, the transfer is only dependent on the phase of the oscillation. If the atom is in a down swing, the transition can happen immediately, if it is in an up swing there is no transition until the atom swings down again, leading to a maximal discrepancy of 200 fs. If the conditions are less optimal but

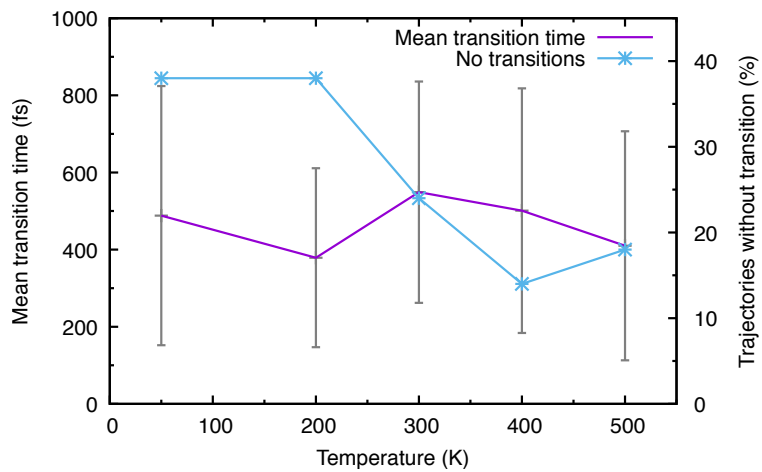


**Figure 37:** Average triplet transition times over simulation temperature. The blue graph indicates the number of trajectories which do not show a triplet transfer within the simulation time of 1 ps. The grey bars indicate the standard deviation of the transition times (non-transfer trajectories excluded). The reduction of trajectories without transitions indicates the lowering of the mean transition time.

need only slight adjustments, the transition will not occur within the first oscillation, but in the second, adding another time window of 200 fs and so on. Therefore, the transition time is highly dependent on the starting conditions.

Another factor is the changing number of trajectories due to the different numbers of trajectories which show a transition. There are two reasons why more trajectories show a transfer at higher temperatures. On one hand, with a higher average velocity there is a higher chance for the dangling bond atom to start with a higher velocity and thus increasing the chance for a transfer. On the other hand, with a higher atom displacement there is a higher likeliness for stronger atom interaction and therefore higher energy transfer. With more energy transfer the time needed to change the conditions is also reduced, leading to a down shift of the higher transition time. This in turn means that trajectories which would not show a transfer within the simulation time at lower temperatures show a transition at higher temperatures, but with high transition times.

Both the effect of the oscillation period as well as of the energy transfer can be seen in figure 38, where the number of transitions per time frame is shown as a histogram. Ideal and nearly ideal starting configurations contribute to a large peak for all temperatures at the range of 0-200 fs, while for high transition times there are notably more trajectories at high temperatures than at low temperatures. However, what is less prominent in this graph, especially for 300 K and 400 K, is the expected rise of better starting conditions due to the higher average velocity at high temperatures. The amount of transitions between 0 K and 200 fs is mostly the same for all temperatures except for 300 K where even a reduction occurs. In order to understand this we consider two example trajectories for 50 K and 400 K and examine the KS levels of the  $k$ -point where the transition occurs first, see figure 39. For the 400 K trajectory (bottom) the transition is, as expected, clearly governed by the dangling bond position. Around 800 fs the dangling bond position is low enough to drive its KS level over the unoccupied TC state. For the 50 K trajectory the dangling bond moves – again as expected – less than at 400 K, with small position variations leading only to small energy variations. However, around 430 fs the unoccupied TC state – independently of the dangling bond motion – lowers its energy and causes

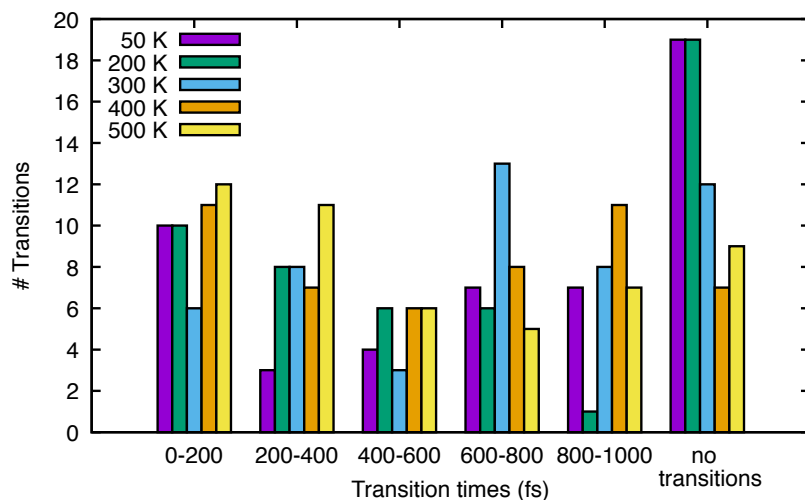


**Figure 38:** Histogram for the number of transitions within a specific time frame. Most notably is a mostly uniform peak at 0-200 fs, followed by an overall decline in transitions, as well as the late time frames being dominated by high temperature transitions. As in figure 37, the trajectories without transitions are mostly low temperature ones.

a hybridization of the states. The hybridization effectively causes the dangling bond to be partially emptied, which subsequently accelerates the downward motion of the atom. This causes its KS level to rise further, de-hybridizes the states and therefore completely emptying the dangling bond. While this TC lowering effect also occurs at 400 K, the 400 K trajectories are as in the example mostly governed by the dangling bond movement, while for 50 K all trajectories with transitions behave like the example and need the lowering of the TC states.

The corresponding TC state is delocalized over several TC molecules, making it difficult to pinpoint the geometrical reason for the energy lowering. Despite checking the position, rotation and deformation of the molecules, no criterion could be found. However, if the TC level would be more likely to reduce its energy with less structural disorder, it could explain the constancy of the number of transitions at low times, as the increase in db kinetic energy would be counteracted by a higher TC energy. This assumption is backed by the fact that the hole KS level at the beginning of the MDs at low temperatures are generally lower than those for high temperatures, see for example the insets in figure 39.

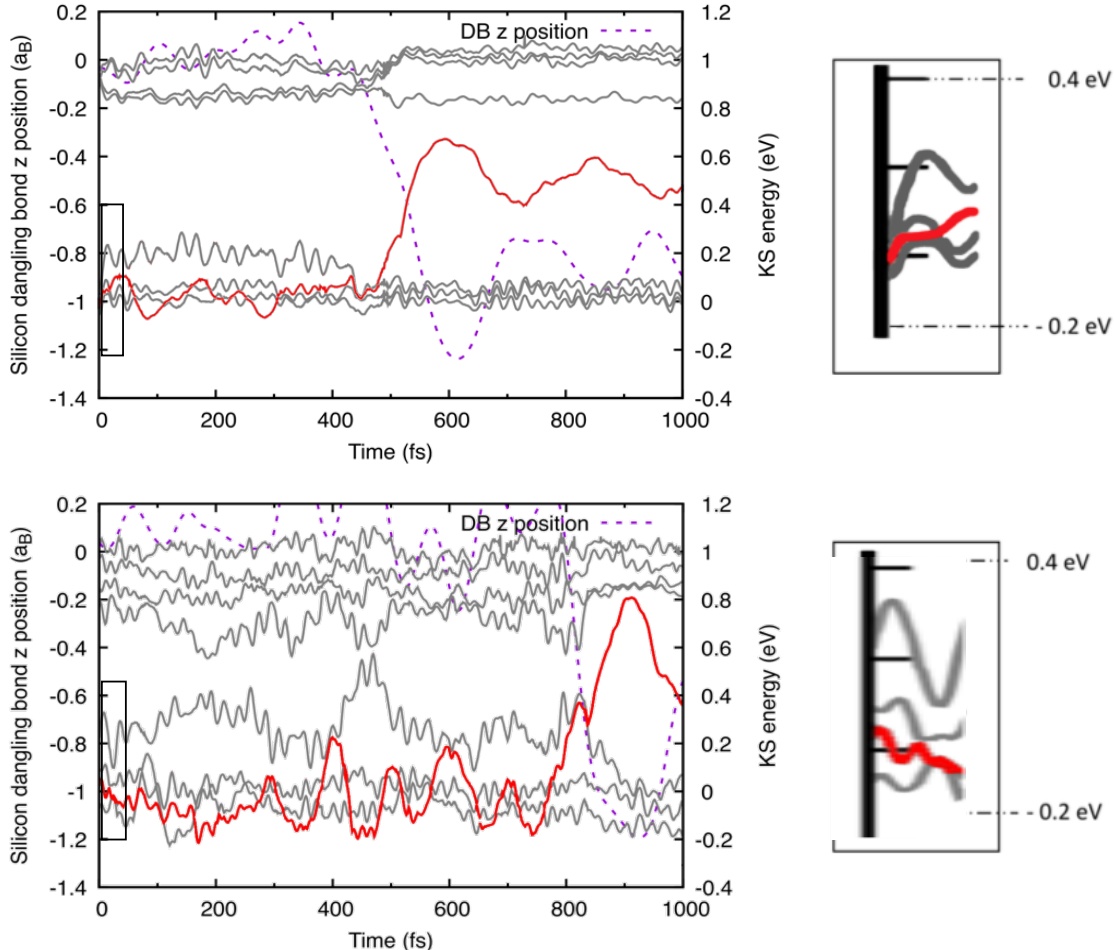


**Figure 39:** Prototypical trajectories for the triplet transfer at the temperatures of 50 K (top) and 400 K (bottom). For 400 K the transition is governed by the dangling bond movement, with the db state rising and crossing the TC state. For 50 K the db state moves little, instead the TC state lowers its energy until it hybridizes with the db state, initiating the transfer. Insets show the relaxation behaviour of the KS states at the beginning.

Furthermore it is to note, that the TC hole state rises in energy shortly after the excitation. This is the case for all trajectories at 50 K, indicating it to be a relaxation process induced by the triplet excitation. However, the difference between the ground state structure and the fully relaxed Si+TC<sub>TC</sub>\* structure is very minuscule (which is part of the reason why no geometrical criterion could be found), this relaxation is easily outdone by the thermal movement at higher temperature. This can also be seen in the insets of figure 39, the rising of the TC state at 400 K is considerably lower than the one at 50 K. While this result is not conclusive, it has to be asked if this effect would occur with a more sophisticated functional. As seen, if hybrid functionals are used the unoccupied state rises higher in energy. Since a MD with hybrid functionals proved impossible to do with the available computational resources, also no data on the fluctuation of the TC level could be obtained. Assuming a similar or slightly higher variation of the KS level, there would be no possibility for the TC state to lower low enough to hybridize with the db state, which would lead to no transfers at 50 K. While it is not possible to proof this assumption directly, since it has been shown that the transfer barrier is localization dependent, one can try to emulate the behaviour of the hybrid functional via the computational less expensive DFT+U formalism, which is covered in the next section.

#### 5.4.3. Exciton transfer using DFT+U

Before going into further detail it has to be stressed that an exact replication of all features of the hybrid functional is not possible. Both carbon and silicon have only their s and p orbitals occupied which, as they tend to delocalize, are normally not described via DFT+U. Testing shows that applying DFT+U on either carbon or silicon barely changes the band gap. Additionally, both elements experience different shifts due to the Hubbard potential, which easily leads to a change in band alignment. Furthermore, the dangling bond Si tries to keep its energetic position relative to the bulk Si constant, leading to a lowering of the atom for higher U-values, which inevitable leads to an emptying of the dangling bond at higher U values. Due to this difficulties we focus on the probably most important aspect: The dispersion of the hole TC state of the Si-TC<sub>TC</sub>\* structure. While the dangling bond state is dispersion free in both HSE and PBE, the hole TC state is dispersion free in HSE and shows dispersion in PBE. This causes the state crossing of the TC and Si state to be at different energies at different  $k$ -points, which in turn leads to the additional PES in the PBE barrier. While this is the main focus for choosing the Hubbard U parameters, secondary aspects one can also try to optimize are the energetic position of the excited electron and hole states, which are respectively lower and higher in HSE than in PBE, and the overall energy difference between both structures.

As already seen in figure 32 lhs, the hole in the Si-TC<sub>TC</sub>\* structure is mostly localized on one molecule, an effect which is increased by the HSE functional. This suggests to only apply the Hubbard correction to one TC molecule. However, it shows that this is still not sufficient, as the hole state is still subject to dispersion, despite being localized at one molecule. By analysing the contributions of the single atoms to the hole state, the 10 carbon atoms of the two middle carbon rings of the molecule were found to have the main contribution to the state, especially around  $\Gamma$ , while the outer ones have less impact on the state and only at the edges of the band. It shows that applying the Hubbard U only to the 10 C atoms of the two middle carbon rings leads to both a reduction in dispersion as well as a raising of the hole and a lowering of the electron state. The U value was adjusted so that these two states qualitatively fit the HSE band structure. Since this leads to a large change in the overall energy difference, an additional Hubbard U term was applied to the

dangling bond Si atom. After small alterations the values of 4.7 eV at the 10 middle C atoms of one molecule and 1.7 eV at the dangling bond Si atom were chosen, the resulting band structures and barrier can be seen in figure 40. The resulting barrier is very close to the HSE one, especially the crossing point of the PESs are nearly identical. However, as already seen in the case of lithium niobate, the Hubbard U values leads to overly stable states. While the last stable point of the PES corresponding to the TC localization of the triplet is around 46 meV in the case of HSE, the 4.7+1.7 eV PBE+U set is stable up to 120 meV. This most probably influences the trajectory during a MD. To compensate for this potential problem, another set of reduced Hubbard values is needed. This set is found with 1.5 eV for the C atoms and 1.7 eV for the dangling bond atom, which results in the last stable TC localization point around 55 meV, see figure 40. In turn, the PES crossing point is way off, suggesting a barrier of 2 meV. This can result in more starting configurations where the triplet is already localized at the Si-surface than to be expected for HSE.

Since both Hubbard U sets can only partly approximate the HSE barrier, molecular dynamics for both sets were conducted. This of course would lead to a doubling of the number of trajectories, wherefore only the fringe cases of 50 K and 400 K are covered. The trajectories are prepared as previous, a 2 ps long MD in the electric ground state at 300 K is performed for both sets, and 50 starting geometries are randomly generated for both sets and temperatures. A further 400 fs MD in the ground state for each configurations is conducted for further thermalization. Afterwards, the actual trajectories with excited triplet are calculated. As in the case of lithium niobate, the higher set of Hubbard U values can lead to numerical problems during the MD calculations. However, in this case they are less severe, as they are more seldom, and continuing the MD for one to three fs without completely converged densities is sufficient to reach structures which can be calculated in a stable manner again.

The resulting number of transition per time frame are shown in figure 41. It is directly apparent that for both sets the low temperature regime shows an enormous increase of trajectories without transition. Only a few trajectories show an early transition. A closer inspection of the trajectories show, that most of these early transitions (in case of the 4.5+1.7 eV set all early transitions) are in fact a direct capture of the triplet by the Si surface. The effect of the lowering TC hole state, while still present, is not strong enough to initiate the transition, it can only aid it. Comparing the high temperature regime for both sets, due to the lower barrier and lower stability of the 1.5+1.7 eV set it shows more direct (or close to direct) captures of the triplet at the Si surface, as expected. The 4.5+1.7 eV set in contrast shows a shift to longer transition times. Both sets, however, are qualitatively the same as without Hubbard correction (compare figure 38). This further solidifies the finding for the transfer occurring at higher temperature. While the transfer process can be substantiated, the back-transfer of the triplet to the TC surface, which occurs in the PBE MDs at high temperatures, could not be observed. This questions the reversibility of the process. However one has also to keep in mind that in a solar cell the electron will be moved to the contacts of the cell and thus removed from the system. As already shown in chapter 5.3, removing one electron from the excited system moves the system into a “middle” state, where the dangling bond is between the  $\text{Si-TC}_{\text{Si}^*}$  and the  $\text{Si-TC}_{\text{TC}^*}$  structure, both spatially and energetically (see also figure 29). Furthermore, besides the removal of the excited electron, the solar cell also returns “used” electrons from the load, which do not have to be the same spin as the removed electron. They can therefore recombine with the hole, effectively creating the same electronic configuration

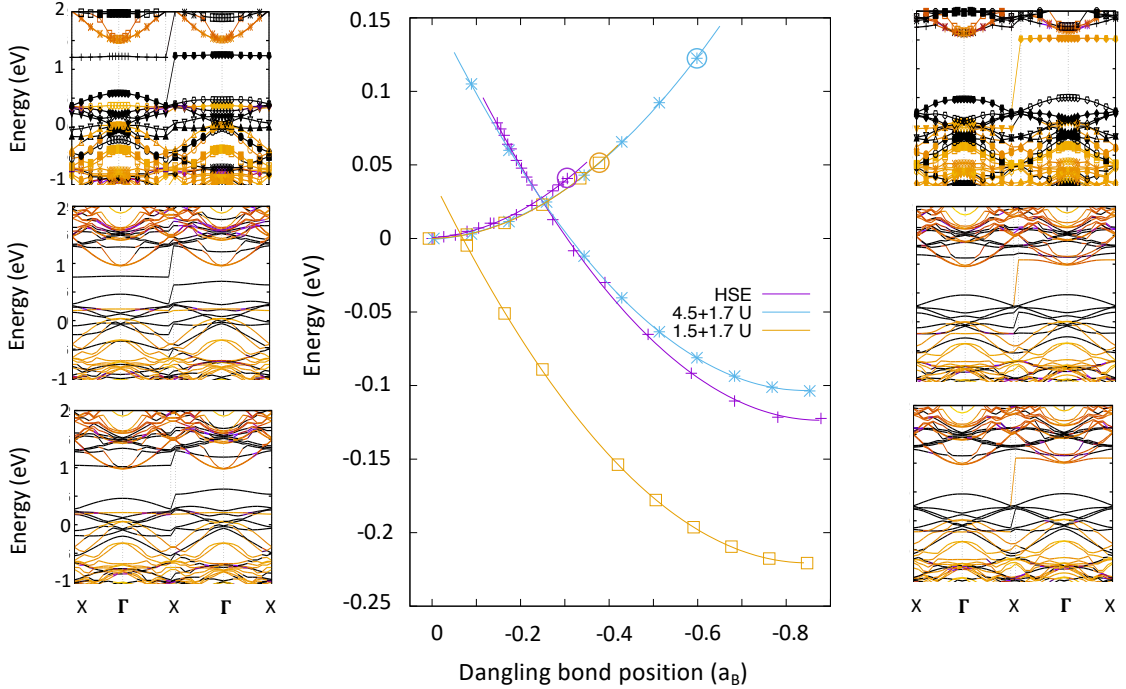


**Figure 40:** Calculated transfer barriers for the HSE functional and PBE+U with 4.5 and 1.7 eV as well as 1.5 and 1.7 eV Hubbard U correction applied to the mid section of one TC molecule and the dangling bond Si atom respectively. The right and left side show the band structures for the corresponding end structures (HSE top, 4.5+1.7 eV middle, 1.5+1.7 eV bottom). The 4.5+1.7 eV set reproduces the HSE barrier well, especially at the crossing point. The band structures are also in qualitative agreement. Not well reproduced, however, is the last stable point of the PES corresponding to the TC localized triplet, designated by the last data point on the corresponding PES (marked with circles as guide for the eye). The 4.5+1.7 eV set largely overestimates the stability. A good description of the stability is given by the lower set of 1.5+1.7 eV. However, this set does not well reproduce the crossing.

as in the beginning. Under this condition the dangling bond oscillations should allow for achieving the same starting conditions once another triplet forms.

In summary the triplet exciton transfer at the silicon-tetracene interface was studied using molecular dynamics, PES calculations and surface hopping procedures. Two surface models were investigated, the bulk like low density model, and the TC2 like high density model. At an idealized surface with H atoms terminating the silicon surface, no exciton transfer could be observed for both models. That changes as soon one H atom is removed, creating a Si dangling bond defect. This defect leads to a band realignment. For the low density model the realignment causes an immediate exciton localization at the Si. For the high density phase this is not the case, the transfer only occurs after thermal activation. The transfer is characterized by a downward movement of the dangling bond atom, which causes a rise of the dangling bond state due to the rehybridization from a  $sp^3$  to the energetically unfavourable  $sp^2+p$  configuration. Once the state crosses the empty TC valence state, the hole transfers to the dangling bond and the electron follows due to electrostatic interaction. The barrier for this process in the HD model was calculated using the HSE and PBE functional, with activation energies around 27 meV and 7 meV. Using MDs with the PBE functional, the transfer times dependent on the temperature were calculated. Those scatter over a large time frame from as low as 1 fs to as high as 1 ps, with some trajectories even not showing a transfer at all. Generally, the higher the

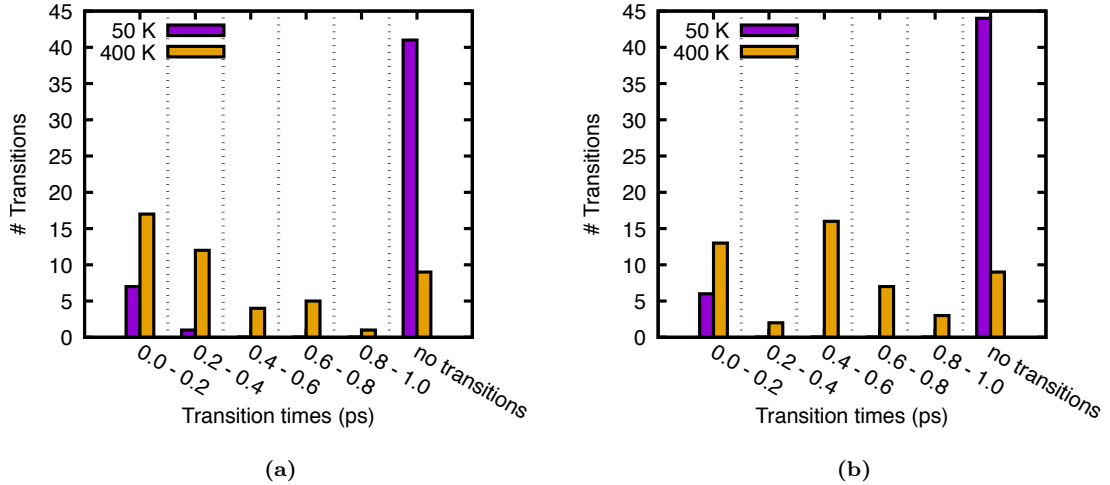


**Figure 41:** Number of transitions within certain time frames for trajectories calculated using PBE+U, where (a) shows the 1.5+1.7 eV set and (b) the 4.5+1.7 eV set. Both sets show a rapid decline of low temperature transitions in comparison with figure 38. The 4.5+1.7 eV set furthermore shows, as expected, a shift to higher transition times compared to the 1.5+1.7 eV set.

temperature the more transfers and shorter transition times are observed as more energy is available to overcome the barrier. However, it appears that there is a dampening effect, as the unoccupied TC state which has to be crossed by the dangling bond tends to rise with more disorder in the system. During the transfer, the dangling bond has to transfer its electron to the empty TC state. The probability for this to occur was calculated using a modified surface hopping approach at fixed trajectories. Those probabilities are dependent on the duration of hybridization, which is shown to increase if no hopping occurs. While incorporating the electron hopping into the transfer is most likely to increase the transfer time, it is neglectable due to the increased hopping chance if no hopping event occurs, and due to the several 100 fs it can take for the level crossing to occur in the first place. Since no hybrid functional MDs were viable, the effect of improved functionals was emulated using DFT+U, whereby the U values are chosen to reconstruct the relevant states for the transfer. While little change is observed at high temperatures, the exciton transfer drastically decreases at low temperatures.

The silicon-tetracene interface clearly shows the restrictions which are imposed by large systems, and what measures can be taken to account for those. While hybrid functional MDs are principally doable, for a system with several hundred atoms they are computationally not feasible. However, opting for the less expensive GGA functional can potentially lead to drastic changes in the computed quantities. In order to assure reliable results, further methods have to be employed additionally. In the presented case the hybrid PES calculation and the DFT+U MDs with hybrid-functional derived U values show the reliability of the PBE MDs.

---

## 6. Conclusions

In this work three different systems, oxirane, lithium niobate and Si(111)-TC were studied. While those systems are fundamentally different from each other – one is a molecule, the other one a crystal and the last one an interface – they are united in that they all show interesting dynamic features upon optical excitation. The “life“ of such an excitation was introduced beginning with the interaction of an electromagnetic field with the system, levelling an electron to a state in the conduction band, followed by electronic and structural relaxation due to the excited state, hopping of the electron to lower states, until it finally reaches the valence band. During the whole process and dependent on the system the excited electron can interact with the system and create quasi-particles, induce phase transitions or lead to chemical reactions. The aim of this work was to simulate the dynamics of these excitation processes and monitor the system-dependent properties which arise due to the excitations, mainly by the use of DFT based molecular dynamics.

For the oxirane molecule the photochemical decomposition, i.e. the reaction  $\text{C}_2\text{H}_4\text{O} + \hbar\nu \rightarrow \text{CH}_3 + \text{COH}$  was studied. The c-DFT method was introduced to move from the ground state only DFT to a computationally cheap approach which can calculate excited states. With this method the ground state and first three excited states were calculated, and used as basis for the hopping between those states during several MDs at finite temperatures by the means of a DFT based FSSH algorithm. The excitation energy of those c-DFT excited states were found to be in good agreement with the high level hybrid TD-DFT method.<sup>[78]</sup> Since oxirane is a small system, electron hopping dynamics for the ground state and first three excited states could be simulated without much computational expense, making the molecule a good testing ground for the method. The temperature was simulated both within the *NVE* ensemble as well as in the *NVT* ensemble by means of the Nosé-Hoover thermostat. With these approaches the experimental established Gomer-Noyes mechanism could be confirmed as main reaction for the photochemical decomposition. This reaction begins when the system switches to the first excited state in a slightly disturbed geometry. The ring opening occurs fully within the first excited state, following this the opposite lying H atoms rotate around the C-C axis. The final H transfer and C-C bond breaking can only occur in the ground state. Starting the simulation from the second excited state, the mechanism occurs within 90 fs. These results are in line with previous findings, except for the ring opening being driven by the first and not the second excited state, which can be attributed to the sensitivity of the system to distortions. The ratio of other reaction products is dependent on both temperature and thermostat. The initial-velocity-only *NVE* approach leads to an abundance of bond breaking like H-abstractions, while the temperature controlled *NVT* ensemble shows a lack of bond breaking and underestimates especially the final C-C bond breaking. This highlights the need for a correct description of energy dissipation even in the fs regime. While these results do not gain much new insight to the system as they mostly confirm already existing findings, they show that the computational inexpensive c-DFT approach and the DFT based surface hopping algorithm are reliable tools (at least for small systems), even compared to high end methods.

In the case of lithium niobate the formation time of polarons in dependence on the temperature was studied. Lithium niobate is an optically non-linear material with several usages like waveguides or frequency changing. Polarons are known to change the intensity of the second and third harmonic generation, i.e. the doubling or tripling of the frequency,<sup>[163,164]</sup> which makes the study of their formation an interesting topic. Starting from the already established additional-electron-model, both the free and bound polaron were considered.

It was shown that the free polaron could not be modelled at finite temperature as the vibrations of the system and the self interaction error delocalize the electron. The bound polaron, however, could be modelled using the DFT+U method. It shows that the U parameters for the static polaron are not suitable for a MD calculation, as those freeze the electron in its starting configuration. A lowering of the U values was necessary to overcome this problem, resulting in a barrier free polaron formation as indicated by relaxation calculations. Considering the unit cell size, this is in line with earlier calculations of trapping radii. With this parameters determined thermal equilibrated starting configurations were generated and MDs conducted. Despite the findings during the oxirane study, it was opted to use the *NVE* ensemble. On one hand, the *NVE* ensemble allows for exact comparisons between trajectories with and without excitation at the same starting geometries, on the other hand, the (most of the times) delocalized electron at the beginning of the trajectory has less impact on the temperature than the directed motion caused by the excitation in the oxirane which also has considerably less atoms. For further insight on the polaron formation, the electronic localization and lattice deformation were examined separately and analysed by the means of conduction band position, local magnetic moment and phonon decomposition. By associating the lowest conduction band position with the dielectric function, a direct comparison to experimental values is enabled. The local magnetic moment allows for a clear monitoring of the charge localization without having to rely on the data heavy electronic density. By decomposing the ion movement into phonon modes one gains a novel possibility to study the influence of the localized electron on the phonon modes, and the influence of the phonon modes on the lattice distortion.

It shows that both localization and formation time are slightly dependent on the temperature, with increasing times at higher temperatures. Furthermore, there is a strong influence of the temperature on the lifetime, with decreasing lifetime at higher temperatures. The formation times are in the range of 50-75 fs, which is on the lower end of experimental values, which is most likely due to the neglect of polaron hopping, as the unit cell is too small to observe this phenomenon. The phonon decomposition and comparison with trajectories without excitation further show that the formation time is dependent on the phase of the oxygen breathing phonon modes. In contrast to oxirane the electron hopping could not be studied. The single  $k$ -point description necessary for the hopping algorithm leads to near zero hopping probabilities, which is most likely due to the highly dispersive manner of the involved states. To account for this dispersion either phenomenological methods or highly expensive methods like cell duplication would have been needed, which were not feasible at the time.

In the last system, the silicon-tetracene Si(111)-TC interface, the triplet exciton transfer from TC to Si was studied. This transfer is of great technological interest, as it would enable the construction of highly efficient Si-TC hybrid solar cells. Without modification of the interface, however, only low to none transfer rates have been observed, a result that could be confirmed in this work by band structure analysis and molecular dynamics. A few experimental studies have reported an increased transfer rate by manipulating the interface, for example by inserting a hafniumoxynitride intermediate layer.<sup>[144]</sup> Often this is tried to be explained by passivation effects.<sup>[143,144]</sup> In this work it could be shown that the opposite might be the case, the introduction of a defect at the Si surface is sufficient to enable the triplet transfer. The removal of a H atom in the passivation layer causes a dangling bond defect which in turn causes a band realignment due to Fermi level pinning. Depending on the surface model – a bulk like TC structure and a high density TC structure were considered – this respectively leads to either a barrier free transfer of the triplet to the

---

silicon, or to the possibility of a transfer, which has to be thermally activated. This process is governed by the movement of the dangling bond (db), where a downward movement of the db atom leads to a less favourable rehybridization of the atomic orbitals, causing the defect spin down state to cross the highest TC valence band and consequently becoming the triplet hole state. The electron follows the hole to the Si surface via electrostatic interaction. The activation barrier for this process was calculated using the HSE and PBE functional by interpolating the dangling bond position and relaxing the system afterwards. Both cases show barrier heights which should be overcome at room temperature.

To study the transfer time, molecular dynamics were conducted at different temperatures and the time of the level crossing chosen as indicator for the transfer. Due to the expensiveness of hybrid functionals the MDs could only be conducted using the PBE functional. Those transfer times, while generally showing a large scatter of up to the simulation time of 1 ps, show a temperature dependency where more transfers occur within the simulation time of the trajectories at high temperatures than at low temperatures. While this behaviour is to be expected, even at 50 K transfers occur. Those transfers are governed by a lowering of the highest TC state instead of a rising of the dangling bond state. As this effect might not occur using hybrid functionals because the corresponding TC state has a higher energy, the behaviour of the hybrid functional was tried to be emulated using the less expensive DFT+U approach. With two sets of Hubbard U values the HSE barrier height and stability were reproduced individually. Molecular dynamics for both sets reproduce the PBE results at high temperatures, while for low temperatures little to no transfers could be registered. The calculated transfer times might be further prolonged by the fact that the level crossing of the db and TC state leads to an excited system, which first has to hop into its ground state in order for the hole to transfer to the Si. This hopping process was modelled using a modified hopping approach for prototypical trajectories. The hopping probability was found highly dependent on the hybridization of the states, leading to variations of 0.1 % and 80 % hopping probability. However, if no hopping occurs, the excited system will increase the hybridization and thus also increase the probability. Due to this effect and the already high variation of transition times the added time due to the hopping is considered negligible. Overall the dangling bond defect has shown to be a reusable “elevator” for excitons. Since this defect is very common and could easily be produced accidentally, for example by the surface manipulation done by several experiments, it could explain the increased transfer rate in those experiments. Whether such defects can be used for the construction of a Si-TC hybrid solar cell remains to be seen. However, due to the general nature of the effect, namely the Fermi level pinning of defects and energetic unfavourable states due to rehybridization, such a mechanism is most probably also present in other interfaces.

Overall DFT based molecular dynamics proved as a reliable tool to investigate time and temperature dependent values in solid states. However, such evaluations are quite costly, as a multitude of trajectories have to be analysed to account for the statistical nature of temperature dependent values. Special attention has to be given to the choice and the parameters for the thermostat and the generation of suitable starting conditions. The importance of the thermostat has been made visible in the study of the oxirane, and all systems, but especially lithium niobate, show a great dependence on the exact geometry at the beginning of the MD. The generation of those starting configurations proved to be a bottleneck for the calculations, as the (usually) necessary MD for finding a thermal equilibrium can not be parallelized. The increasing system size and the need for more trajectories made it necessary to resort to increasingly more elaborated generation of randomized start-

ing structures and velocities which are close to thermal equilibrium. For the Si-TC interface for example the typical generation by a singular molecular dynamic or by random displacements was not possible by any means due to the only weakly coupled degrees of freedom of the sub systems. Instead a random distribution routine for each sub-system had to be developed to generate different realistic starting positions. Due to the computational cost, especially for large systems, one is often limited to a restricted choice of basis set and xc-functional. For Si-TC for example the calculation of hybrid functional MDs proved to be prohibitively expensive to compute. This underlines the necessity to substantiate the “lower level” MDs via other methods like the calculation of PES, force constants or band structures. Sometimes a cheaper method like DFT+U can emulate certain behaviours of more expensive methods, in this case one, however, has to keep in mind that most likely only parts will be simulated correctly. It is therefore important to decide which quantity is the most relevant for the analysis. DFT+U itself proved as a useful method to increase localization within DFT. In conjunction with molecular dynamics though it proved difficult to find fitting U parameters, as the values calculated for relaxed structures are generally to high and cause a “freezing” of the electronic configuration as seen in lithium niobate. In case of Si-TC one could correctly calculate the barrier by PES intersection, but the stability of each state, i.e. staying on the same PES despite an energetic favourable one existing, is way higher than for hybrid functionals. Emulating both barrier and stability correctly at the same time proved impossible. Using DFT+U in dynamics therefore is possible, but needs a lot of parameter tweaking to produce reliable results. Last but not least the DFT based FSSH algorithm proved to be reliable for hopping between localized states as in molecules or defects, not only for small systems as oxirane but also for large systems like Si-TC or InP. However it fails at predicting the hopping probabilities for systems with a high band dispersion like lithium niobate. This failing is due to being only able to account for a single  $k$ -point and having to omit any inter  $k$ -point interaction. To circumvent this problem one might consider folding the Brillouine zone by multiplying the unit cell, which, however, quickly results in overly large systems. The electron hopping could alternatively be approximated *ex situ*, for example by the Landau-Zener method, or could be guessed by calculating the electron-phonon interaction coefficients for q-vectors which connects the different  $k$ -points. As of this point<sup>4</sup> there is no DFT based *in situ* method to include inter  $k$ -point hopping. However, as phonons are basically atom displacements, which also occur during a MD (in fact phonons modes can be calculated from a MD<sup>[32]</sup>), it seems reasonable that there is a possibility to include such a coupling during a MD.

---

<sup>4</sup>to the authors knowledge

---

## A. Program modifications

The dynamic calculation, in particular their flexible applicability to various 3D and 2D periodic systems, becomes only possible by several necessary modifications of the used codes.

The smearing scheme of the LIBRA-X program<sup>[52]</sup> was modified according to equation 3.53 to allow for excitations higher than the second excited state. The code was furthermore adapted to allow choosing an arbitrary  $k$ -point for the extraction of the KS wave functions from a set of  $k$ -points defined by the DFT calculation, which allowed for (spin-polarized) calculations with more than one  $k$ -point. To increase the efficiency of the LIBRA-X code the calculation of the different excited states by c-DFT was parallelized. The read-in routines, the starting configuration generator and the thermostat were modified to allow for specific atoms to stay fixed during a MD, as necessary for modelling a surface. In order to gain more fail safety and flexibility the creation of a restart file and a restart routine were implemented. Lastly minor changes in terms of output and compatibility with the PC<sup>2</sup> NOCTUA-I and NOCTUA-II cluster were done, but are not listed in detail.

The smearing routine for the c-DFT calculations was later on implemented into the QUANTUM ESPRESSO pw code<sup>[33,34]</sup>, which a) enabled the usage of other smearing distributions besides the Fermi-Dirac distribution and b) largely reduced the in- and output operations between the Libra-X and Quantum espresso code, which tends to be a bottleneck for the calculations, especially for small systems.

## B. Publications

The author contributed to following articles in scientific journals:

- M. Krenz, U. Gerstmann and W.G. Schmidt, Photochemical Ring Opening of Oxirane Modelled by Constrained Density Functional Theory, ACS Omega **5**, 24057 (2020), <https://doi.org/10.1021/acsomega.0c03483>, PMID: 32984727.
- M. Krenz, U. Gerstmann and W. G. Schmidt, Bound polaron formation in lithium niobate from ab initio molecular dynamics, Applied Physics A **128**, 480 (2022).
- M. Krenz, U. Gerstmann and W.G. Schmidt, Defect assisted exciton transfer across the tetracene-Si(111):H interface, submitted to Phys. Rev. Lett.
- B. Halbig, M. Liebhaber, U. Bass, J. Geurts, E. Speiser, J. Räthel, S. Chandola, N. Esser, M. Krenz, S. Neufeld, W.G. Schmidt, S. Sanna, Vibrational properties of the Au-(3×3)/Si(111) surface reconstruction, Physical Review B **97** (2018).
- C.W. Nicholson, M. Puppin, A. Lücke, U. Gerstmann, M. Krenz, W.G. Schmidt, L. Rettig, R. Ernstorfer, M. Wolf, Excited-state band mapping and momentum-resolved ultrafast population dynamics in In/Si(111) nanowires investigated with XUV-based time- and angle-resolved photoemission spectroscopy, Physical Review B **99** (2019).
- Jonathan Diederich, Jennifer Velasquez-Rojas, Mohammad Amin Zare Pour, Isaac Azahel Ruiz Alvarado, Marvin Krenz, Agnieszka Paszuk, Christian Höhn, Klaus Schwarzburg, David Ostheimer, Rainer Eichberger, Wolf Gero Schmidt, Thomas Hannapel, Roel van de Krol and Dennis Friedrich, Indium Phosphide excitations under water exposure (title is subject to change), work in progress, to be published

Other scientific publications:

- M. Krenz, A. Bocchini, T. Biktagirov, A. Kozub, S. Badalov, S. Neufeld, I. A. Ruiz Alvarado, U. Gerstmann, and W. G. Schmidt, Polaron formation dynamics in lithium niobate from massively parallel ab-initio simulations High Performance Computing in Science and Engineering 2022, Springer Nature Switzerland AG

## Bibliography

- [1] G. Czycholl, Theoretische Festkörperphysik Band 1 (Springer, 2016).
- [2] C. Kittel, Introduction to solid state physics, John Wiley & Sons, New York , 402 (1996).
- [3] R. M. Martin, Electronic structure: basic theory and practical methods (Cambridge university press, 2020).
- [4] M. C. Payne, M. P. Teter, D. C. Allan, T. Arias and a. J. Joannopoulos, Iterative minimization techniques for ab initio total-energy calculations: molecular dynamics and conjugate gradients, Reviews of modern physics **64**, 1045 (1992).
- [5] N. C. Handy and A. M. Lee, The adiabatic approximation, Chemical physics letters **252**, 425 (1996).
- [6] P. Hohenberg and W. Kohn, Inhomogeneous electron gas, Physical review **136**, B864 (1964).
- [7] E. Engel, Density functional theory (Springer, 2011).
- [8] W. Kohn and L. J. Sham, Self-Consistent Equations Including Exchange and Correlation Effects, Phys. Rev. **140**, A1133 (1965).
- [9] J. Lagrange, Mécanique Analytique, volume 1. Courcier, Paris, revised edition, 1811.
- [10] A. D. Becke, Density functional theories in quantum chemistry: Beyond the local density approximation, ACS Publications, 1989.
- [11] J. P. Perdew, J. A. Chevary, S. H. Vosko, K. A. Jackson, M. R. Pederson, D. J. Singh and C. Fiolhais, Atoms, molecules, solids, and surfaces: Applications of the generalized gradient approximation for exchange and correlation, Physical review B **46**, 6671 (1992).
- [12] Searchresults Web of science, criteria “DFT” and “Density functional theory” in Abstract or keyword in the year 2022, 2023.
- [13] G. D. Billing, Classical path method in inelastic and reactive scattering, International reviews in physical chemistry **13**, 309 (1994).
- [14] D. Carfi, The Pointwise Hellmann-Feynman Theorem, AAPP **LXXXVIII**, C1A0101004 (2010).
- [15] H. Hellman, Einführung in die Quantenchemie, Franz Deuticke, Leipzig **285** (1937).
- [16] R. P. Feynman, Forces in molecules, Physical review **56**, 340 (1939).
- [17] J. L. Hudgins, Wide and narrow bandgap semiconductors for power electronics: A new valuation, Journal of Electronic materials **32**, 471 (2003).

[18] W. Demtröder, *Experimentalphysik 1: Mechanik und Wärme* (Springer-Verlag, 2017).

[19] V. Rühle, Berendsen and nose-hoover thermostats, *Am. J. Phys* (2007).

[20] A. Lemak and N. Balabaev, On the Berendsen thermostat, *Molecular Simulation* **13**, 177 (1994).

[21] H. J. Berendsen, J. v. Postma, W. F. Van Gunsteren, A. DiNola and J. R. Haak, Molecular dynamics with coupling to an external bath, *The Journal of chemical physics* **81**, 3684 (1984).

[22] P. H. Hünenberger, Thermostat algorithms for molecular dynamics simulations, *Advanced computer simulation: Approaches for soft matter sciences I* , 105 (2005).

[23] S. Nosé, A unified formulation of the constant temperature molecular dynamics methods, *The Journal of chemical physics* **81**, 511 (1984).

[24] D. Sidler and S. Riniker, Fast Nosé–Hoover thermostat: molecular dynamics in quasi-thermodynamic equilibrium, *Physical Chemistry Chemical Physics* **21**, 6059 (2019).

[25] G. J. Martyna, M. L. Klein and M. Tuckerman, Nosé–Hoover chains: The canonical ensemble via continuous dynamics, *The Journal of chemical physics* **97**, 2635 (1992).

[26] W. Qian and C. Zhang, Review of the phonon calculations for energetic crystals and their applications, *Energetic Materials Frontiers* **2**, 154 (2021).

[27] A. V. Kuznetsov and C. J. Stanton, Theory of coherent phonon oscillations in semiconductors, *Physical review letters* **73**, 3243 (1994).

[28] O. Misochnko, M. Hase, K. Ishioka and M. Kitajima, Transient Bose–Einstein condensation of phonons, *Physics Letters A* **321**, 381 (2004).

[29] A. Einstein, Quantum theory of the monatomic ideal gas, *Sitzungsberichte der Preussischen Akademie der Wissenschaften, Physikalisch-mathematische Klasse* , 261 (1924).

[30] M. M. Dacorogna, M. L. Cohen and P. K. Lam, Self-consistent calculation of the  $q$  dependence of the electron-phonon coupling in aluminum, *Physical review letters* **55**, 837 (1985).

[31] P. García-Risueño, P. Han and G. Bester, Frozen-phonon method for state anticrossing situations and its application to zero-point motion effects in diamondoids, *arXiv preprint arXiv:1904.05385* (2019).

[32] S. Baroni, S. De Gironcoli, A. Dal Corso and P. Giannozzi, Phonons and related crystal properties from density-functional perturbation theory, *Reviews of modern Physics* **73**, 515 (2001).

[33] P. Giannozzi *et al.*, QUANTUM ESPRESSO: a modular and open-source software project for quantum simulations of materials, *Journal of physics: Condensed matter* **21**, 395502 (2009).

[34] P. Giannozzi *et al.*, Advanced capabilities for materials modelling with Quantum ESPRESSO, *Journal of physics: Condensed matter* **29**, 465901 (2017).

[35] L. Hedin, New method for calculating the one-particle Green's function with application to the electron-gas problem, *Phys. Rev.* **139**, A769 (1965).

- [36] M. E. Casida, Time-dependent density-functional response theory for molecules, in *Recent Advances In Density Functional Methods: (Part I)*, World Scientific, 1995.
- [37] C. R. Jacob and M. Reiher, Spin in density-functional theory, *International Journal of Quantum Chemistry* **112**, 3661 (2012).
- [38] A. Hellman, B. Razaznejad and B. I. Lundqvist, Potential-energy surfaces for excited states in extended systems, *The Journal of chemical physics* **120**, 4593 (2004).
- [39] Q. Wu and T. Van Voorhis, Direct optimization method to study constrained systems within density-functional theory, *Physical Review A* **72**, 024502 (2005).
- [40] B. Kaduk, T. Kowalczyk and T. Van Voorhis, Constrained density functional theory, *Chemical reviews* **112**, 321 (2012).
- [41] R. O. Jones and O. Gunnarsson, The density functional formalism, its applications and prospects, *Reviews of Modern Physics* **61**, 689 (1989).
- [42] J. Gavnholt, T. Olsen, M. Engelund and J. Schiøtz,  $\Delta$  self-consistent field method to obtain potential energy surfaces of excited molecules on surfaces, *Physical Review B* **78**, 075441 (2008).
- [43] T. Frigge *et al.*, Optically excited structural transition in atomic wires on surfaces at the quantum limit, *Nature* **544**, 207 (2017).
- [44] T. Kowalczyk, S. R. Yost and T. V. Voorhis, Assessment of the  $\Delta$ SCF density functional theory approach for electronic excitations in organic dyes, *The Journal of chemical physics* **134** (2011).
- [45] C.-L. Cheng, Q. Wu and T. Van Voorhis, Rydberg energies using excited state density functional theory, *The Journal of chemical physics* **129** (2008).
- [46] W. Sotoyama, Simulation of low-lying singlet and triplet excited states of multiple-resonance-type thermally activated delayed fluorescence emitters by delta self-consistent field ( $\Delta$ SCF) method, *The Journal of Physical Chemistry A* **125**, 10373 (2021).
- [47] M. Kasha, Characterization of electronic transitions in complex molecules, *Discuss. Faraday Soc.* **9**, 14 (1950).
- [48] J. C. Tully, Molecular dynamics with electronic transitions, *J. Chem. Phys.* (1990).
- [49] A. V. Akimov and O. V. Prezhdo, The PYXAID program for non-adiabatic molecular dynamics in condensed matter systems, *Journal of chemical theory and computation* **9**, 4959 (2013).
- [50] B. Smith and A. V. Akimov, Modeling nonadiabatic dynamics in condensed matter materials: some recent advances and applications, *Journal of Physics: Condensed Matter* **32**, 073001 (2019).
- [51] A. V. Akimov, Nonadiabatic molecular dynamics with tight-binding fragment molecular orbitals, *Journal of chemical theory and computation* **12**, 5719 (2016).
- [52] E. Pradhan, K. Sato and A. V. Akimov, Non-adiabatic molecular dynamics with  $\Delta$ SCF excited states, *Journal of Physics: Condensed Matter* **30**, 484002 (2018).
- [53] J. P. Perdew, Density functional theory and the band gap problem, *International Journal of Quantum Chemistry* **28**, 497 (1985).

[54] P. Mori-Sánchez, A. J. Cohen and W. Yang, Localization and delocalization errors in density functional theory and implications for band-gap prediction, *Physical review letters* **100**, 146401 (2008).

[55] J. P. Perdew and A. Zunger, Self-interaction correction to density-functional approximations for many-electron systems, *Physical Review B* **23**, 5048 (1981).

[56] T. Tsuneda and K. Hirao, Self-interaction corrections in density functional theory, *The Journal of chemical physics* **140** (2014).

[57] H. J. Kulik, Perspective: Treating electron over-delocalization with the DFT+ U method, *The Journal of chemical physics* **142** (2015).

[58] E. Pavarini, E. Koch, F. Anders and M. Jarrell, Correlated electrons: from models to materials, *Reihe Modeling and Simulation* **2** (2012).

[59] M. Cococcioni and S. De Gironcoli, Linear response approach to the calculation of the effective interaction parameters in the LDA+ U method, *Physical Review B* **71**, 035105 (2005).

[60] M. Côté, *Introduction to DFT+ U*, International Summer School on Numerical Methods for Correlated Systems in Condensed Matter, Université de Montréal,(May 26 to Jun. 6, 2008) , 23 (2008).

[61] D. Hait and M. Head-Gordon, Delocalization Errors in Density Functional Theory Are Essentially Quadratic in Fractional Occupation Number, *The Journal of Physical Chemistry Letters* **9**, 6280 (2018), <https://doi.org/10.1021/acs.jpclett.8b02417>.

[62] P. Mori-Sánchez and A. J. Cohen, The derivative discontinuity of the exchange-correlation functional, *Physical Chemistry Chemical Physics* **16**, 14378 (2014).

[63] J. F. Janak, Proof that  $\partial E / \partial n_i = \varepsilon$  in density-functional theory, *Physical Review B* **18**, 7165 (1978).

[64] G. Trimarchi, Z. Wang and A. Zunger, Polymorphous band structure model of gapping in the antiferromagnetic and paramagnetic phases of the Mott insulators MnO, FeO, CoO, and NiO, *Physical Review B* **97**, 035107 (2018).

[65] A. Svane, Electronic structure of  $\text{La}_2\text{CuO}_4$  in the self-interaction-corrected density-functional formalism, *Physical review letters* **68**, 1900 (1992).

[66] I. Duck, W. Pauli and E. Sudarshan, *Pauli and the spin-statistics theorem* (World Scientific, 1997).

[67] W. Pauli, *Die allgemeinen prinzipien der wellenmechanik* (Springer, 1933).

[68] J. C. Slater, The theory of complex spectra, *Physical Review* **34**, 1293 (1929).

[69] V. Fock, Näherungsmethode zur Lösung des quantenmechanischen Mehrkörperproblems, *Zeitschrift für Physik* **61**, 126 (1930).

[70] P. Lykos and G. Pratt, Discussion on the Hartree-Fock approximation, *Reviews of Modern Physics* **35**, 496 (1963).

[71] P. J. Hasnip, K. Refson, M. I. Probert, J. R. Yates, S. J. Clark and C. J. Pickard, Density functional theory in the solid state, *Philosophical Transactions of the Royal Society A: Mathematical, Physical and Engineering Sciences* **372**, 20130270 (2014).

- [72] P.-F. Loos and P. M. Gill, Ground state of two electrons on concentric spheres, *Physical Review A* **81**, 052510 (2010).
- [73] A. Kerridge, A. Harker and A. Stoneham, Quantum behaviour of hydrogen and muonium in vacancy-containing complexes in diamond, *Journal of Physics: Condensed Matter* **16**, 8743 (2004).
- [74] Y.-i. Matsushita, K. Nakamura and A. Oshiyama, Comparative study of hybrid functionals applied to structural and electronic properties of semiconductors and insulators, *Physical Review B* **84**, 075205 (2011).
- [75] M. Krenz, U. Gerstmann and W. G. Schmidt, Photochemical Ring Opening of Oxirane Modeled by Constrained Density Functional Theory, *ACS Omega* **5**, 24057 (2020), <https://doi.org/10.1021/acsomega.0c03483>, PMID: 32984727.
- [76] F. Lyon, VOLUME 97 1, 3-Butadiene, Ethylene Oxide and Vinyl Halides (Vinyl Fluoride, Vinyl Chloride and Vinyl Bromide).
- [77] G. C. Mendes, T. R. Brandao and C. L. Silva, Ethylene oxide sterilization of medical devices: a review, *American journal of infection control* **35**, 574 (2007).
- [78] E. Tapavicza, I. Tavernelli, U. Rothlisberger, C. Filippi and M. E. Casida, Mixed time-dependent density-functional theory/classical trajectory surface hopping study of oxirane photochemistry, *Journal of Chemical Physics* **129**, 124108 (2008).
- [79] E. Gomer and J. W. A. Noyes, Photochemical Studies. XLII. Ethylene Oxide, *J. Am Chem. Soc.* **72**, 101 (1950).
- [80] M. Kawasaki, . T. Ibuki, M. Iwasaki and Y. Takezaki, Vacuum-ultraviolet photolysis of ethylene oxide, *Journal of Chemical Physics* **59**, 2076 (1973).
- [81] X. Bin, A. Azizi, T. Xu, S. R. Kirk, M. Filatov and S. Jenkins, Next-generation quantum theory of atoms in molecules for the photochemical ring-opening reactions of oxirane, *International Journal of Quantum Chemistry* **119**, e25957 (2019).
- [82] T. Helgaker, P. Jorgensen and J. Olsen, Molecular electronic-structure theory (John Wiley & Sons, 2013).
- [83] M. A. Marques and E. K. Gross, Time-dependent density functional theory, *Annu. Rev. Phys. Chem.* **55**, 427 (2004).
- [84] J. Alonso and N. Cordero, Nonlocal weighted density approximation to exchange, correlation and kinetic energy in density functional theory, in *Theoretical and Computational Chemistry* Vol. 4, Seiten 239–294, Elsevier, 1996.
- [85] F. Cordova, L. J. Doriol, A. Ipatov, M. E. Casida, C. Filippi and A. Vela, Troubleshooting time-dependent density-functional theory for photochemical applications: Oxirane, *The Journal of chemical physics* **127**, 164111 (2007).
- [86] T.-K. Liu and A. Duncan, The absorption spectrum of ethylene oxide in the vacuum ultraviolet, *The Journal of Chemical Physics* **17**, 241 (1949).
- [87] A. Lowrey III and K. Watanabe, Absorption and ionization coefficients of ethylene oxide, *The Journal of Chemical Physics* **28**, 208 (1958).
- [88] G. Fleming, M. M. Anderson, A. J. Harrison and L. W. Pickett, Effect of ring size on

the far ultraviolet absorption and photolysis of cyclic ethers, *The Journal of Chemical Physics* **30**, 351 (1959).

[89] T. Ozaki, Continued fraction representation of the Fermi-Dirac function for large-scale electronic structure calculations, *Physical Review B* **75**, 035123 (2007).

[90] N. Marzari, D. Vanderbilt, A. De Vita and M. C. Payne, Thermal Contraction and Disordering of the Al(110) Surface, *Phys. Rev. Lett.* **82**, 3296 (1999).

[91] M. Spiekermann, D. Bougeard and B. Schrader, Coupled calculations of vibrational frequencies and intensities. III. IR and Raman spectra of ethylene oxide and ethylene sulfide, *Journal of Computational Chemistry* **3**, 354 (1982).

[92] M. Krenz, U. Gerstmann and W. G. Schmidt, Bound polaron formation in lithium niobate from ab initio molecular dynamics, *Applied Physics A* **128**, 480 (2022).

[93] M. Bazzan and C. Sada, Optical waveguides in lithium niobate: Recent developments and applications, *Applied Physics Reviews* **2** (2015).

[94] L. N. Binh, Lithium niobate optical modulators: Devices and applications, *Journal of crystal growth* **288**, 180 (2006).

[95] Y. Qi and Y. Li, Integrated lithium niobate photonics, *Nanophotonics* **9**, 1287 (2020).

[96] A. Zaltron *et al.*, Integrated optics on lithium niobate for sensing applications, in *Optical Sensors 2015* Vol. 9506, Seiten 50–59, SPIE, 2015.

[97] W. M. Haynes, *CRC handbook of chemistry and physics* (CRC press, 2014).

[98] A. Alexandrov and P. Kornilovitch, Mobile small polaron, *Physical Review Letters* **82**, 807 (1999).

[99] O. Schirmer, M. Imlau, C. Merschjann and B. Schoke, Electron small polarons and bipolarons in  $\text{LiNbO}_3$ , *Journal of Physics: Condensed Matter* **21**, 123201 (2009).

[100] G. Wellein, H. Röder and H. Fehske, Polarons and bipolarons in strongly interacting electron-phonon systems, *Physical Review B* **53**, 9666 (1996).

[101] D. Emin, Optical properties of large and small polarons and bipolarons, *Physical Review B* **48**, 13691 (1993).

[102] T. Mitra, A. Chatterjee and S. Mukhopadhyay, Polarons, *Physics Reports* **153**, 91 (1987).

[103] M. Imlau, H. Badorreck and C. Merschjann, Optical nonlinearities of small polarons in lithium niobate, *Applied Physics Reviews* **2** (2015).

[104] F. Schmidt, A. L. Kozub, T. Biktagirov, C. Eigner, C. Silberhorn, A. Schindlmayr, W. G. Schmidt and U. Gerstmann, Free and defect-bound (bi) polarons in  $\text{LiNbO}_3$ : Atomic structure and spectroscopic signatures from ab initio calculations, *Physical Review Research* **2**, 043002 (2020).

[105] F. Schmidt, A. L. Kozub, U. Gerstmann, W. G. Schmidt and A. Schindlmayr, Electron Polarons in Lithium Niobate: Charge Localization, Lattice Deformation, and Optical Response, *Crystals* **11** (2021).

- [106] W. T. Pollard, S.-Y. Lee and R. A. Mathies, **Wave packet theory of dynamic absorption spectra in femtosecond pump–probe experiments**, *The Journal of chemical physics* **92**, 4012 (1990).
- [107] Y. Qiu, K. Ucer and R. Williams, **Formation time of a small electron polaron in LiNbO<sub>3</sub>: measurements and interpretation**, *physica status solidi (c)* **2**, 232 (2005).
- [108] I. S. Akhmadullin, V. Golenishchev-Kutuzov, S. Migachev and S. Mironov, **Low-temperature electrical conductivity of congruent lithium niobate crystals**, *Physics of the Solid state* **40**, 1190 (1998).
- [109] K. Buse, A. Adibi and D. Psaltis, **Non-volatile holographic storage in doubly doped lithium niobate crystals**, *nature* **393**, 665 (1998).
- [110] D. Berben, K. Buse, S. Wevering, P. Herth, M. Imlau and T. Woike, **Lifetime of small polarons in iron-doped lithium–niobate crystals**, *Journal of applied physics* **87**, 1034 (2000).
- [111] S. Sasamoto, J. Hirohashi and S. Ashihara, **Polaron dynamics in lithium niobate upon femtosecond pulse irradiation: Influence of magnesium doping and stoichiometry control**, *Journal of Applied Physics* **105**, 083102 (2009).
- [112] J. Czochralski, **Ein neues verfahren zur messung der kristallisationsgeschwindigkeit der metalle**, *Zeitschrift für physikalische Chemie* **92**, 219 (1918).
- [113] T. Volk and M. Wöhlecke, **Lithium niobate: defects, photorefraction and ferroelectric switching** Vol. 115 (Springer Science & Business Media, 2008).
- [114] K. Lengyel *et al.*, **Growth, defect structure, and THz application of stoichiometric lithium niobate**, *Applied Physics Reviews* **2** (2015).
- [115] L. Guilbert, L. Vittadello, M. Bazzan, I. Mhaouech, S. Messerschmidt and M. Imlau, **The elusive role of Nb<sub>Li</sub> bound polaron energy in hopping charge transport in Fe: LiNbO<sub>3</sub>**, *Journal of Physics: Condensed Matter* **30**, 125701 (2018).
- [116] S. Albrecht, **Optical absorption spectra of semiconductors and insulators: ab initio calculation of many-body effects**, (1999).
- [117] A. Marini, C. Hogan, M. Grüning and D. Varsano, **Yambo: an ab initio tool for excited state calculations**, *Computer Physics Communications* **180**, 1392 (2009).
- [118] D. Sangalli *et al.*, **Many-body perturbation theory calculations using the yambo code**, *Journal of Physics: Condensed Matter* **31**, 325902 (2019).
- [119] P. Reckenthaler, D. Maxein, T. Woike, K. Buse and B. Sturman, **Separation of optical Kerr and free-carrier nonlinear responses with femtosecond light pulses in LiNbO<sub>3</sub> crystals**, *Physical Review B* **76**, 195117 (2007).
- [120] H. Badorreck, S. Nolte, F. Freytag, P. Bäune, V. Dieckmann and M. Imlau, **Scanning nonlinear absorption in lithium niobate over the time regime of small polaron formation**, *Optical Materials Express* **5**, 2729 (2015).
- [121] O. Beyer, D. Maxein, T. Woike and K. Buse, **Generation of small bound polarons in lithium niobate crystals on the subpicosecond time scale**, *Applied Physics B* **83**, 527 (2006).

[122] M. Rüsing, S. Sanna, S. Neufeld, G. Berth, W. Schmidt, A. Zrenner, H. Yu, Y. Wang and H. Zhang, **Vibrational properties of  $\text{LiNb}_{1-x}\text{Ta}_x\text{O}_3$  mixed crystals**, Physical Review B **93**, 184305 (2016).

[123] C. Zener, **Non-adiabatic crossing of energy levels**, Proceedings of the Royal Society of London. Series A, Containing Papers of a Mathematical and Physical Character **137**, 696 (1932).

[124] C. Wittig, **The landau- zener formula**, The Journal of Physical Chemistry B **109**, 8428 (2005).

[125] G. H. Wannier, **The structure of electronic excitation levels in insulating crystals**, Physical Review **52**, 191 (1937).

[126] N. Marzari and D. Vanderbilt, **Maximally localized generalized Wannier functions for composite energy bands**, Physical review B **56**, 12847 (1997).

[127] N. Marzari, A. A. Mostofi, J. R. Yates, I. Souza and D. Vanderbilt, **Maximally localized Wannier functions: Theory and applications**, Reviews of Modern Physics **84**, 1419 (2012).

[128] W. Bludau, A. Onton and W. Heinke, **Temperature dependence of the band gap of silicon**, Journal of Applied Physics **45**, 1846 (1974).

[129] Y. Okada and Y. Tokumaru, **Precise determination of lattice parameter and thermal expansion coefficient of silicon between 300 and 1500 K**, Journal of applied physics **56**, 314 (1984).

[130] J. Niederhausen, R. W. MacQueen, K. Lips, H. Aldahhak, W. G. Schmidt and U. Gerstmann, **Tetracene ultrathin film growth on hydrogen-passivated silicon**, Langmuir **36**, 9099 (2020).

[131] P. M. Zimmerman, F. Bell, D. Casanova and M. Head-Gordon, **Mechanism for singlet fission in pentacene and tetracene: From single exciton to two triplets**, Journal of the American Chemical Society **133**, 19944 (2011).

[132] T. Takahashi, T. Takenobu, J. Takeya and Y. Iwasa, **Ambipolar Light-Emitting Transistors of a Tetracene Single Crystal**, Advanced Functional Materials **17**, 1623 (2007), <https://onlinelibrary.wiley.com/doi/pdf/10.1002/adfm.200700046>.

[133] N. J. Turro, **The triplet state**, Journal of Chemical Education **46**, 2 (1969).

[134] R. Poli and J. N. Harvey, **Spin forbidden chemical reactions of transition metal compounds. New ideas and new computational challenges**, Chemical Society Reviews **32**, 1 (2003).

[135] M. B. Smith and J. Michl, **Singlet fission**, Chemical reviews **110**, 6891 (2010).

[136] T. Markvart and L. Castaner, **IIa-1 - Principles of Solar Cell Operation** (Elsevier Science, Amsterdam, 2003).

[137] M. Iqbal, **An introduction to solar radiation** (Elsevier, 2012).

[138] W. Shockley and H. J. Queisser, **Detailed balance limit of efficiency of p-n junction solar cells**, Journal of applied physics **32**, 510 (1961).

[139] S. Rühle, **Tabulated values of the Shockley–Queisser limit for single junction solar cells**, Solar energy **130**, 139 (2016).

- [140] A. F. van den Boom, S. Ferro, M. Gelvez-Rueda, H. Zuilhof and B. Ehrler, Toward Improving Triplet Energy Transfer from Tetracene to Silicon Using a Covalently Bound Tetracene Seed Layer, *The Journal of Physical Chemistry Letters* (2023).
- [141] G. B. Piland, J. J. Burdett, T.-Y. Hung, P.-H. Chen, C.-F. Lin, T.-L. Chiu, J.-H. Lee and C. J. Bardeen, Dynamics of molecular excitons near a semiconductor surface studied by fluorescence quenching of polycrystalline tetracene on silicon, *Chemical Physics Letters* **601**, 33 (2014).
- [142] B. Daiber, S. P. Pujari, S. Verboom, S. L. Luxembourg, S. W. Tabernig, M. H. Futscher, J. Lee, H. Zuilhof and B. Ehrler, A method to detect triplet exciton transfer from singlet fission materials into silicon solar cells: Comparing different surface treatments, *The Journal of Chemical Physics* **152** (2020).
- [143] B. Daiber *et al.*, Change in tetracene polymorphism facilitates triplet transfer in singlet fission-sensitized silicon solar cells, *The journal of physical chemistry letters* **11**, 8703 (2020).
- [144] M. Einzinger *et al.*, Sensitization of silicon by singlet exciton fission in tetracene, *Nature* **571**, 90 (2019).
- [145] S. Grimme, Semiempirical GGA-type density functional constructed with a long-range dispersion correction, *Journal of Computational Chemistry* **27**, 1787 (2006), <https://onlinelibrary.wiley.com/doi/10.1002/jcc.20495>.
- [146] V. Barone, M. Casarin, D. Forrer, M. Pavone, M. Sambi and A. Vittadini, Role and effective treatment of dispersive forces in materials: Polyethylene and graphite crystals as test cases, *Journal of Computational Chemistry* **30**, 934 (2009), <https://onlinelibrary.wiley.com/doi/10.1002/jcc.21112>.
- [147] C. Adamo and V. Barone, Toward reliable density functional methods without adjustable parameters: The PBE0 model, *The Journal of chemical physics* **110**, 6158 (1999).
- [148] J. Heyd and G. E. Scuseria, Efficient hybrid density functional calculations in solids: Assessment of the Heyd–Scuseria–Ernzerhof screened Coulomb hybrid functional, *The Journal of chemical physics* **121**, 1187 (2004).
- [149] J. Tirado-Rives and W. L. Jorgensen, Performance of B3LYP density functional methods for a large set of organic molecules, *Journal of chemical theory and computation* **4**, 297 (2008).
- [150] P. J. Stephens, F. J. Devlin, C. F. Chabalowski and M. J. Frisch, Ab initio calculation of vibrational absorption and circular dichroism spectra using density functional force fields, *The Journal of physical chemistry* **98**, 11623 (1994).
- [151] D. Holmes, S. Kumaraswamy, A. J. Matzger and K. P. C. Vollhardt, On the Nature of Nonplanarity in the [N] Phenyles, *Chemistry—A European Journal* **5**, 3399 (1999).
- [152] O. Madelung, Numerical data and functional relationships in science and technology, *Landolt Bornstein, New Series, Group III* **22**, 117 (1982).
- [153] P. Linstrom and W. Mallard, editors, *NIST Chemistry WebBook, NIST Standard Reference Database Number 69* (National Institute of Standards and Technology, Gaithersburg MD, 20899, 2023).

- [154] Y. Tomkiewicz, R. Groff and P. Avakian, Spectroscopic approach to energetics of exciton fission and fusion in tetracene crystals, *The Journal of Chemical Physics* **54**, 4504 (1971).
- [155] Y. Wan, G. P. Wiederrecht, R. D. Schaller, J. C. Johnson and L. Huang, Transport of Spin-Entangled Triplet Excitons Generated by Singlet Fission, *The Journal of Physical Chemistry Letters* **9**, 6731 (2018), <https://doi.org/10.1021/acs.jpclett.8b02944>.
- [156] S. M. Janke, M. Rossi, S. V. Levchenko, S. Kokott, M. Scheffler and V. Blum, Pentacene and tetracene molecules and films on H/Si (111): Level alignment from hybrid density functional theory, *Electronic Structure* **2**, 035002 (2020).
- [157] T. Ihn, *Semiconductor Nanostructures: Quantum states and electronic transport* (OUP Oxford, 2009).
- [158] X. Liu, M. S. Choi, E. Hwang, W. J. Yoo and J. Sun, Fermi level pinning dependent 2D semiconductor devices: challenges and prospects, *Advanced Materials* **34**, 2108425 (2022).
- [159] W. Demtröder, *Experimentalphysik 3: Atome, Moleküle und Festkörper* (Springer-Verlag, 2016).
- [160] J. Diederich *et al.*, Indium Phosphide excitations under water exposure (title is subject to change), Work in progress, to be published .
- [161] G. Henkelman, B. P. Uberuaga and H. Jónsson, A climbing image nudged elastic band method for finding saddle points and minimum energy paths, *The Journal of chemical physics* **113**, 9901 (2000).
- [162] H. Jónsson, G. Mills and K. W. Jacobsen, Nudged elastic band method for finding minimum energy paths of transitions, in *Classical and quantum dynamics in condensed phase simulations*, Seiten 385–404, World Scientific, 1998.
- [163] A. L. Kozub, U. Gerstmann and W. G. Schmidt, Third-Order Susceptibility of Lithium Niobate: Influence of Polarons and Bipolarons, *physica status solidi (b)* **260**, 2200453 (2023).
- [164] A. L. Kozub, A. Schindlmayr, U. Gerstmann and W. G. Schmidt, Polaronic enhancement of second-harmonic generation in lithium niobate, *Physical Review B* **104**, 174110 (2021).

## List of Figures

1. The Gomer-Noyes mechanism <sup>[79]</sup> mainly responsible for the photochemical decomposition of oxirane. . . . .	25
2. Calculated electron densities of the ground state and lowest excited states of oxirane. . . . .	27
3. State populations for <i>NVE</i> calculations modelling an initial temperature of 100 K (lhs) and 300 K (rhs). . . . .	30
4. Reaction products over time in the microcanonical <i>NVE</i> ensemble for temperatures of 100 K (lhs) and 300 K (rhs). . . . .	30
5. State populations for <i>NVT</i> calculations modelling an initial temperature of 100 K (lhs) and 300 K (rhs). . . . .	31
6. Reaction products over time calculated in the canonical <i>NVT</i> ensemble at temperatures of 100 K (lhs) and 300 K (rhs). . . . .	31
7. Percentage of end products over temperature after 250 fs integration time calculated in the microcanonical <i>NVE</i> (lhs) and canonical <i>NVT</i> ensembles (rhs). . . . .	32
8. Electronic densities of the active $S_1$ during the ring opening reaction for an example trajectory after 5, 15 and 30 fs. . . . .	34
9. Electronic densities of the active state for an example trajectory of an inhibited H transfer. . . . .	34
10. Electronic densities of the active state during an O abstraction reaction of an example trajectory. . . . .	34
11. Lithium niobate shown in its hexagonal unit cell. . . . .	37
12. Structure and electronic density of the free (lhs) and bound (rhs) polaron. . . . .	41
13. Kohn-Sham energies and dielectric functions for a prototypical MD. . . . .	45
14. Evolution of the mean distance of the excess electron to the $Nb_{Li}$ antisite atom. . . . .	46
15. Evolution of the local magnetic moment at the defect $Nb_{Li}$ and the average bond length between the $Nb_{Li}$ atom and the nearest O atoms surrounding the defect. This figure is reused from Ref. 92 in accordance with the Creative Commons licence 4.0. . . . .	47
16. Subset of phonon modes for the LN unit cell. . . . .	47
17. Dependence of the average times required for electronic localization, polaron formation, and polaron quenching on the simulation temperature. This figure is reused from Ref. 92 in accordance with the Creative Commons licence 4.0. . . . .	48
18. Number of trajectories with electron localization times above and below 20 fs depending on the temperature. . . . .	49
19. Evolution of average O- $Nb_{Li}$ distances for eight example trajectories at 600 K with (left) and without (right) excess charge. This figure is reused from Ref. 92 in accordance with the Creative Commons licence 4.0 . . . . .	53
20. Tetracene molecule with (rhs) and without (lhs) triplet excitation. . . . .	58
21. Top and side view of the high and low density phase. . . . .	60
22. Electron and hole densities for the considered excitation in the TC bulk crystal. . . . .	62
23. Averaged electrostatic potential over the x-y plane for the Si-TC interface (lhs) and a Si unit cell (rhs). . . . .	63
24. Partial densities of states for the ground state of the high density (lhs) and low density phase (rhs). . . . .	64

25.	Partial density of states for a vertical triplet excitation at the ground state structure of the HD model. . . . .	65
26.	PDOS of the ground state of the HD phase with dangling bond. . . . .	66
27.	PDOS with added triplet excitation. . . . .	67
28.	Band structure corresponding to the PDOS of figure 26. . . . .	67
29.	PDOS of the uncharged dangling bond HD structure. . . . .	68
30.	PDOS of the HD phase with dangling bond at the TC localized triplet structure (Si-TC <sub>TC*</sub> , lhs) and the Si localized triplet structure (Si-TC <sub>Si*</sub> , rhs). .	68
31.	PDOS for the LD model with dangling bond in the ground state (lhs) and with excited triplet (rhs). . . . .	69
32.	Charge densities of the triplet during an exemplary trajectory starting at the Si-TC <sub>TC*</sub> structure. . . . .	70
33.	Dangling bond z position and KS energies at one $k$ -point for the trajectory as in figure 32. . . . .	71
34.	Graphs analogue to figure 33 for two other trajectories. . . . .	73
35.	c-DFT Molecular dynamic starting at 330 fs of the trajectory in figure 33, i.e. directly after the level crossing. . . . .	74
36.	Transition barriers calculated via NEB (lhs) and linear interpolating the dangling bond position while relaxing the rest of the structure (rhs). . . . .	75
37.	Average triplet transition times over simulation temperature. . . . .	78
38.	Histogram for the number of transitions within a specific time frame. . . . .	79
39.	Prototypical trajectories for the triplet transfer at the temperatures of 50 K (top) and 400 K (bottom). . . . .	80
40.	Calculated transfer barriers for the HSE functional and PBE functional with Hubbard correction. . . . .	83
41.	Number of transitions within certain time frames for trajectories calculated using PBE+U. . . . .	84

## List of Tables

1.	Oxirane singlet excitation energies (in eV) for (PBE) c-DFT in comparison with other computational methods as well with experimental data. . . . .	27
2.	Geometrical parameters used to determine the reaction products. . . . .	29
3.	Calculated reaction yields after 250 fs simulation time compared to experimental data after optical excitation with 174 - 147 nm light <sup>[80]</sup> . . . . .	33
4.	Si and Tc excitation energies (in eV) calculated using $\Delta$ -scf and c-DFT. . . . .	61
5.	Singlet and triplet excitation energies (in eV) in the bulk TC crystal for different functionals and excitation configurations. . . . .	62



## Danksagung

Diese Arbeit wäre ohne die Unterstützung einiger Personen nicht möglich gewesen, und ohne viele weitere wesentlich weniger erträglich zu schreiben gewesen. Sich bei allen zu bedanken, würde sicherlich den Umfang dieser Arbeit immens erhöhen, daher entschuldige ich mich im Voraus bei denen, die ich im Folgenden nicht explizit nenne.

Zuerst möchte ich mich bei Prof. Dr. Wolf Gero Schmidt bedanken, der meinen Werdegang seit meiner Bachelorarbeit begleitet. Vielen Dank für die Diskussionen, Unterstützung und Vielzahl an physikalischen Systemen, die ich bearbeiten durfte. Es ist erstaunlich zu sehen, wie die unterschiedlichsten Systeme und Probleme immer wieder Gemeinsamkeiten aufweisen!

Prof. Dr. Simone Sanna sei gedankt für den Einstieg in das spannende Gebiet der Dichtefunktionaltheorie, und dafür dass er mich schon im vierten Semester direkt in die Forschung mit einbezogen hat.

Die übrige Promotionskommission möchte ich auch nicht außen vor lassen; danke dass ihr euch die Zeit nehmt euch mit meiner Arbeit zu befassen.

Ein großes Danke geht auch an Prof. Dr. Uwe Gerstmann für die langen und hilfreichen Diskussionen, Hilfestellungen in sowohl physikalischen als auch technischen Fragen und dafür, dass man auf eine Frage nicht nur eine Antwort, sondern auch viele nützliche Zusatzinformationen bekommt. An meine Arbeitskollegen auf N3, durch die ein sehr angenehmes Arbeitsklima auf dem Flur herrscht, geht natürlich ebenfalls ein herzliches Danke. Insbesondere möchte ich meiner Bürokollegin Dr. Adriana Bocchini danken, die gemäß unserem inoffiziellen Büromotto „Meckern steigert die Moral“ stets ein offenes Ohr für fachliche als auch für allgemeine Belange hat. Mit absoluter Selbstverständlichkeit ist auch Simone Lange zu danken. Die Bezeichnung „Sekretärin“ ist meiner Meinung nach unpassend für eine Person, ohne die der ganze Flur in kurzer Zeit zum Erliegen kommen würde.

Zudem möchte ich mich bei meinen Kommilitonen, Freunden und Familie bedanken. Man hat es nicht immer einfach mit mir – danke dafür das ihr mich erträgt und unterstützt. Ich danke insbesondere dir, Melanie, für das Korrekturlesen und die fortlaufende Motivation. Ich bin immer mal wieder überrascht, dass es Leute gibt die mit mir Sport machen, und dann die Motivation haben immer wieder zum Training zu kommen. Meinen Eltern Petra und Wolfgang danke ich für die fortlaufende Unterstützung, welche es mir erst ermöglicht hat mich näher mit der Physik zu beschäftigen. Ebenfalls für ihre Unterstützung und nicht zuletzt für ihre hervorragenden Kochkünste danke ich meiner Großmutter Wilma.

Zu guter Letzt möchte ich mich bei meinem ehemaligen Schachtrainer Zoltán Nagy bedanken. In dieser Arbeit habe ich Simulationen im Femto- bis Pikosekundenbereich durchgeführt. Er hat diesen Vorhersagebereich gesprengt, indem er schon vor mehr als 20 Jahren vorhergesagt hat, dass ich einmal diesen Weg einschlagen würde.